National Library
of Canada

Acquisitions and
Bibliographic Services Branch

395 Wellington Street
Ottawa, Ontario
K1A 0N4

Bibliothèque nationale
du Canada

Direction des acquisitions et
des services bibliographiques

395, rue Wellington
Ottawa (Ontario)
K1A 0N4

Your file Votre référence

Our file Notre référence

NOTICE

The quality of this microform is heavily dependent upon the quality of the original thesis submitted for microfilming. Every effort has been made to ensure the highest quality of reproduction possible.

If pages are missing, contact the university which granted the degree.

Some pages may have indistinct print especially if the original pages were typed with a poor typewriter ribbon or if the university sent us an inferior photocopy.

Reproduction in full or in part of this microform is governed by the Canadian Copyright Act, R.S.C. 1970, c. C-30, and subsequent amendments.

AVIS

La qualité de cette microforme dépend grandement de la qualité de la thèse soumise au microfilmage. Nous avons tout fait pour assurer une qualité supérieure de reproduction.

S'il manque des pages, veuillez communiquer avec l'université qui a conféré le grade.

La qualité d'impression de certaines pages peut laisser à désirer, surtout si les pages originales ont été dactylographiées à l'aide d'un ruban usé ou si l'université nous a fait parvenir une photocopie de qualité inférieure.

La reproduction, même partielle, de cette microforme est soumise à la Loi canadienne sur le droit d'auteur, SRC 1970, c. C-30, et ses amendements subséquents.

Canada

A TECHNIQUE FOR TWO-COLOUR PARTICLE IMAGE VELOCIMETRY

BY

GREGORY JOHN SMALLWOOD

A thesis submitted to the Faculty of Graduate Studies and Research
in partial fulfilment of the requirements for the degree of Master of Applied Science

Department of Mechanical Engineering
University of Ottawa
Ottawa, Ontario, Canada

National Library
of Canada

Acquisitions and
Bibliographic Services Branch

395 Wellington Street
Ottawa, Ontario
K1A 0N4

Bibliothèque nationale
du Canada

Direction des acquisitions et
des services bibliographiques

395, rue Wellington
Ottawa (Ontario)
K1A 0N4

Your file Votre référence

Our file Notre référence

ISBN 0-315-80032-1

ABSTRACT

To study the complex flowfields found in combustion, it is often necessary to acquire an instantaneous overall view of the flowfield. One method of achieving this is two-dimensional velocity mapping with particle image velocimetry (PIV). A two-colour PIV experimental apparatus has been developed expressly to meet the demands of combustion and related flowfields. This technique offers advantages over other PIV methods in that the absolute velocity vector direction is known and data processing requirements are reduced. A method for calculating the mean exposure from particles on colour film, based on Mie scattering theory, is developed. A technique optimized for analysis of two-colour PIV images is described. Two-colour PIV is demonstrated in the wake of a noncombusting n-heptane fuelled bluff-body burner, which presented a suitably complex flowfield including counter-rotating recirculation zones and centreline stagnation points. To complement these results, mean velocities obtained with LDA are also presented. This is the first report of spray velocity measurement by PIV.

ACKNOWLEDGEMENTS

To Dave Snelling. who has been my colleague and mentor, I wish to express gratitude and thanks for his support, stimulating discussions, enthusiasm and, most of all, friendship since I joined the research community.

To Bill Hallett, my advisor, I am grateful and appreciative of his incredible patience and unwavering support throughout the course of this research. I would also like to thank Bill for his guidance and assistance.

Good efforts in scientific research result from discussion of good ideas and subsequent accurate implementation of the experiments. For this I must thank my colleagues and the skilled technical staff in the Combustion and Fluids Engineering Program. I would especially like to thank Bob Sawchuk for his tremendous help with lasers and optics, and our leader Rick Williamson for his encouragement and support. For their work in two-colour PIV, all the researchers at Systems Research Laboratories (Wright Laboratories) have contributed, and I would like to thank Mike Post in particular for his help.

I am grateful to the National Research Council and the Department of National Defence for providing financial support throughout the course of this project.

The greatest thanks of all belongs to Susan, my wife and best friend, who has been outstanding throughout, and our daughters Chelsea and Megan, all of whom have brought me great happiness.

Greg Smallwood
Ottawa, April 1992

TABLE OF CONTENTS

NOMENCLATURE

Letters:

A	surface area of spherical section defined by the lens
A_e	area of particle image in the film plane
$b(x_c, y_c)$	intensity of blue particles at coordinates (x_c, y_c) in the correlation map
d	distance
d_a	diameter of aperture of lens
d_{aero}	effective aerodynamic diameter
$dC_{sca}/d\Omega$	differential scattering cross-section
d_e	particle image diameter
d_l	laser beam diameter
d_p	particle diameter
d_s	lens blur circle diameter
d_{sep}	particle image separation
Δd	particle motion distance
D_{min}	minimum film density (gross fog level)
D_{max}	maximum film density (saturation level)
$D_{1.0}$	film density of 1.0 above D_{min}
$E_{\parallel i}$, $E_{\perp i}$	incident electric field parallel and perpendicular to the scattering plane
$E_{\parallel s}$, $E_{\perp s}$	scattered electric field parallel and perpendicular to the scattering plane
E_{xi}, E_{yi}	incident electric field in x and y directions
f	focal length of lens
$f\#$	f-number of camera lens
$g(x_c-\xi, y_c-\psi)$	intensity of green particles at coordinates $(x_c-\xi, y_c-\psi)$ in the correlation map
H	correlation histogram
i	dimensionless scattered irradiance per unit incident irradiance
$i_\parallel$, $i_\perp$	components of i for parallel and perpendicular incident light
I_0	incident irradiance
k	wavenumber of light
L	specific colour layer in colour film
M	lens magnification
n	number of blue particle images, number of vectors
n_f	refractive index of fluid
N_{max}	maximum number density of seed particles
N_p	number of pixels per unit measurement
P	image separation
P_{max}	maximum image separation
Q_i	degree of coverage in the image plane
r	distance from origin to an arbitrary detection point
R	radius of lens
R_s	scanner resolution
Re	Reynolds number

s	distance from origin to centre of lens
S_j, S_{ij}	amplitude scattering matrix elements ($j = 1$ to 4)
t	time
Δt	illumination period
t_{sep}	time separation between laser pulses
u	object distance from lens
v	image distance from lens
V	velocity
V_{max}	maximum anticipated velocity
V_p	particle velocity
V_{pix}	velocity represented by one pixel separation
V_x, V_y	x and y components of the velocity vector
w	width of region-of-interest
W	laser pulse energy
x	direction normal to laser sheet
Δx	laser sheet thickness
Δx_{edge}	laser sheet thickness at edge of region-of-interest
x_b	x coordinate of blue particle in image
x_i	x coordinate of interpolation location
x_p	nondimensional size parameter
y	direction of span of laser sheet
Δy	laser sheet span
y_b	y coordinate of blue particle in image
y_i	y coordinate of interpolation location
z	direction of propagation of laser beam

Greek Letters:

α	angle from lens axis to detection point projected onto x-z plane
β	angle between lens axis and a scattered ray striking the lens
γ	film gamma (slope of characteristic curve)
ε	mean exposure
θ_a	half-angle of diffraction limited spot size
θ_d	laser beam divergence
θ_s	scattering angle
λ	free-space wavelength of light
μ	fluid dynamic viscosity
ξ	x distance from correlation map origin
ρ_p	particle density
ρ_h	particle density (hollow spheres)
ρ_s	particle density (solid spheres)
τ_p	particle response time
ϕ	azimuthal angle
ψ	y distance from correlation map origin

Ω	solid angle subtended by camera lens

Acronyms:

1-D	one-dimensional
2-D	two-dimensional
3-D	three-dimensional
cw	continuous wave
CCD	charge-coupled device
DIV	digital image velocimetry
FWHM	full width at half of the maximum
LDA	laser Doppler anemometry
LSV	laser speckle velocimetry
MPTRS	Mike Post tracking software
Nd:YAG	neodymium-doped yttrium-aluminum-garnet (laser)
PIDV	particle image displacement velocimetry
PIV	particle image velocimetry
PTV	particle tracking velocimetry
RGB	red, green, blue
SLPM	standard litres per minute
SMD	Sauter mean diameter
TOC	test-object-contrast

1 INTRODUCTION

Improved combustion performance of hydrocarbon-fuelled combustors, through increased efficiency and reduced emissions, is a high priority research requirement. The most effective method for responding to this need is to develop a fundamental understanding of combustion processes. This can be achieved through an integrated program, in which experimental research data obtained from advanced laser-based optical diagnostics are used to improve the knowledge of combustion, and to evaluate and improve computer models of the physical and chemical processes in combustion.

A determining factor in the performance of liquid-fuelled combustors is the fuel spray behaviour, which affects fuel/air mixing, flame stability, soot formation, flame radiation, and unburned hydrocarbons. It is important to characterize individual droplet velocities in fuel sprays, in both combusting and noncombusting flows.

To study the complex flowfields found in combustion, with large scale structures such as recirculation zones, it is often necessary to acquire a view of the overall flowfield. In addition, many combustion-related flowfields are transient, either due to intermittent combustion or to the presence of structures such as vortices in continuous combustion. In such situations, it is important that the overall view be instantaneous.

To provide this, laser-based optical diagnostics have been developed for simultaneous full-field (two-dimensional) velocity mapping. This work describes a two-colour double-pulse PIV (particle image velocimetry) technique. Double-pulse PIV is a method in which a droplet- or particle-laden flowfield is illuminated by two sequential, two-dimensional, spatially coincident pulsed laser light sheets, the light scattered from the seed material is recorded on film by a camera with its line-of-sight placed orthogonally to the laser sheet, and the film is analyzed to determine velocities from the displacement and direction of image pairs. The two-colour method employs spectral separation to resolve the 180° directional ambiguity common to the conventional monochromatic methods for acquiring PIV images, in which the magnitude and relative angle of the velocity are known, but the direction of the vector is not, since it is not known which of the particle images was recorded first and which was second.

In recent years PIV has matured to the point that in many instances it is being used as an application with little or no reporting of further development on the technique itself. The following examples are discussed to demonstrate the widespread use of PIV as a diagnostic tool in fluid dynamics, fluid mechanics, and combustion.

PIV has been used to examine the roll-up of the laminar shear layer into vortices, and their subsequent growth and interactions, in the transition region (Re=3600) of a three-dimensional jet.[1] This revealed the nature of the instability process occurring in the initial region of the jet.

Flow turbulence can be estimated from experimental visibility of fringes using a variant of the Young's fringe analysis method,[2] provided that the type of turbulence (isotropic, wake flows) is known.

The flowfield through a planar turbine cascade has been measured under highly accelerating conditions.[3] Two-colour PIV was used to track particles entering the cascade at 80 m/s and exiting at 340 m/s with a turning angle of 72°.

Measurements have been made in a motored reciprocating engine[4] to determine velocity. Further interpretation of the velocity data reveals scalar quantities such as large scale vorticity and strain rate. The analysis system used for this work is now marketed commercially as the TSI

Model 6000 Interrogation System for Particle Image Velocimetry.

Other examples include measuring convection currents near a heated wall,[5] measuring square channel velocity profiles,[6] investigating transonic flowfields about a bluff cylinder in a wind tunnel,[7] and observing the velocity field of a turbulent circular jet impinging upon a flat plate.[8]

Applications in combusting flows include measurements in laminar premixed flames,[9] diffusion flames,[10] and a pulverized coal flame.[11]

In a comprehensive survey on the imaging of sprays,[12] it is noted that to date there have been no instantaneous 2-D velocimetry data published for sprays. Subsequent to this, the only reports of PIV in sprays known to this author are those presented while preparing this document.[13,14]

The objective of the two-colour PIV technique is to extend the capabilities of conventional double-pulse PIV to the wide range of conditions found in combustion-related flowfields. This range of conditions includes velocities from below 1 m/s to greater than 200 m/s, a velocity dynamic range in a single flowfield of 20:1, flow reversal and recirculation, seed particles or droplets with diameters from below 1 μm to greater than 100 μm, and interference from combustion and soot formation.

This work reviews laser-based two-dimensional velocity mapping methods, including PIV. Light scattering theory for small particles is outlined, an algorithm for calculating particle image exposure on film as a function of the experimental conditions is presented, and the image analysis fundamentals are described. Experimental considerations are discussed for the choice of laser, recording medium, method of digitization, seed particles, and related items.

As a demonstration, the two-colour PIV technique is then applied in a noncombusting axisymmetric bluff-body stabilized turbulent diffusion flame burner to measure the velocities of n-heptane droplets. This is the first report, to the author's knowledge, of spray velocities measured by PIV. It is also one of the most complex flowfields reported to be analyzed by PIV, with recirculation, centreline stagnation points, a wide range of droplet sizes, and a large variation in the seeding density. Individual randomly spaced droplet velocities are shown, as is an interpolated velocity map. To complement this, point mean velocity measurements made by LDA (laser Doppler anemometry) are presented.

2 BACKGROUND

Optical diagnostics for combustion and fluids research can be grouped into three main classes: flow visualization techniques, single point measuring techniques, and two-dimensional imaging techniques.[15] The common individual techniques that make up each of these categories, along with the observation(s) that may be made with each, are listed in Table I.

Flow visualization techniques provide useful qualitative information about the structure of the flowfield. Schlieren and shadowgraph are line-of-sight averaging methods that may be realised with conventional light sources. Sheet illumination, along with the related measuring and imaging techniques, usually requires some of the optical properties of laser beams, such as monochromaticity, coherence, low angular divergence, and high energy. An advantage of sheet illumination is that typically it is the sheet thickness, not the imaging lens, that defines the depth-of-field.

The single point measuring techniques require bringing two or more laser beams to a common focus, creating a small elliptical control volume in which quantitative measurements are made. These measurements are typically made point-by-point throughout the flowfield over a period of time at each point. Mean and variance (turbulence) statistics may be calculated for each point.

The two-dimensional imaging techniques provide quantitative data from laser sheet illumination experiments. Most of these methods may also be used for single point measurements. Due to the relatively slow acquisition rate of electronic imaging systems, as compared to single point systems, the images are acquired intermittently, produced by pulsed

Table I Optical diagnostics for combustion and fluids research

TECHNIQUE	OBSERVATION
QUALITATIVE FLOW VISUALIZATION METHODS	
Schlieren	index of refraction gradients (density, temperature)
Shadowgraph	index of refraction gradients (density, temperature)
Sheet-illumination	Mie scattering from particles
SINGLE POINT MEASURING METHODS	
LDA (laser Doppler anemometry)	particle velocity
PDPA (phase-Doppler particle analysis)	particle size and velocity
CARS (coherent anti-Stokes Raman spectroscopy)	gas temperature and major species concentration
TWO-DIMENSIONAL IMAGING TECHNIQUES	
PIV (particle image velocimetry)	particle velocity
PLIF (planar laser-induced fluorescence)	minor species concentration and temperature
DFWM (degenerate four-wave mixing)	minor species concentration and temperature
Rayleigh scattering	total density
Exciplex fluorescence	separate gas and liquid phases of fuel

laser sources. These methods provide instantaneous images of a two-dimensional section of the entire flowfield, which is useful for identifying major structures, and is essential for transient conditions.

The two-dimensional particle imaging techniques for velocity measurement are referred to by a variety of names and acronyms, including particle image velocimetry (PIV), particle tracking velocimetry (PTV), laser speckle velocimetry (LSV), particle image displacement velocimetry (PIDV), and digital image velocimetry (DIV). These methods differ in experimental approach and analysis methods, yet have in common that they require particles to be illuminated by laser light sheets and subsequently imaged to determine the particle velocities. Often the velocities are used to infer the velocity of the surrounding fluid. Reviews of these methods have been written by Adrian,[16] who also discusses molecular velocimetry, Cenedese and Paglialunga,[17] who focus on digital analysis methods, Hunter and Collins,[18] who also include holographic velocimetry, Lourenco *et al.*,[19] and Hesselink,[20] who discusses all digital flow visualization methods.

Aspects of the particle imaging methods of velocimetry that are discussed below include experimental techniques, methods of analysis, error considerations, and particle characteristics. For the purpose of brevity, in the following sections all of these methods will be referred to generically as PIV unless otherwise specified.

2.1 EXPERIMENTAL TECHNIQUES FOR ACQUIRING PIV IMAGES

Historically, PIV has evolved from qualitative flow visualization techniques such as particle streak photography and stroboscopic photography, which could be made quantitative through laborious manual analysis of the photographs.

The first method to be realized with digital analysis of images was laser speckle velocimetry, which was demonstrated in laminar flowfields.[21,22,23,24] This is a double or multiexposure technique that requires a very high seed density to create a speckle pattern in the image, which is then analyzed by the Young's fringe method (analysis methods are discussed below, in Section 2.2). It was later shown[25,26] that in most practical flowfields the particle concentrations required to create speckle patterns were unlikely to be achieved.

With lower seed densities, the double pulse PIV method was established,[27] which relied not upon speckle patterns, but used actual particle images in the photograph for analysis purposes. Double-pulse PIV suffers from two drawbacks. Since it involves double-pulsing a single monochromatic laser, the time interval between the pulses, and thus the range of velocities that may be measured, is fixed.[27] The second, more serious, problem is that the technique suffers from 180° directional ambiguity. This occurs because it is not known which of the two images for each particle was recorded first, unless there is *a priori* knowledge of the flowfield. The following experimental techniques were developed to avoid this problem of directional ambiguity, yet are based upon the concepts of conventional double-pulse monochromatic PIV.

One method is to apply a known velocity bias of magnitude greater than the maximum expected negative velocities, so that all velocities are positive in the measured image. This is done by spatially shifting the image on the detector between the first and second exposures, either with a rotating mirror,[28] scanning mirror,[29] or by electro-optical methods.[30] The electro-optical technique involves placing a birefringent crystal in front of the detector lens so that it will pass the rays of one polarization unaltered and deflect the rays of the orthogonal polarization. A Pockels cell placed at the exit of the double-pulsed laser is used to switch the laser polarization between laser pulses. The scattered radiation favours the plane of polarization of the incident radiation by several orders of magnitude, so that the birefringent crystal will shift the second image with respect to the first. These methods reduce the dynamic range of measurable velocities by the magnitude of the velocity bias.

Pulse tagging is another way of resolving the directional ambiguity.[31] This uses pulses of different duration, resulting in a point image and a short streak image, to identify the direction.

However, pulse tagging can only be achieved by chopping the output of a *cw* (continuous wave) laser, such as an Argon-ion laser. This limits the technique to relatively slow moving phenomena, since the time resolution is not adequate to prevent image blurring in high velocity flows.

The use of pulses of two different colours to resolve the 180° directional ambiguity requires a minimum of experimental complexity while retaining applicability to a wide range of flowfield conditions. This was initially proposed to study spray plume propagation in diesel fuel injection.[32] The first successful application was to measure the flow through a turbine cascade.[33] The two-colour method was also demonstrated as a combustion diagnostic in a propane diffusion flame.[34] These applications used a frequency-doubled Nd:YAG laser and an Nd:YAG-pumped dye laser as the sources for the two colours. A variation of this method is to generate the second colour by Raman-shifting the frequency-doubled output of an Nd:YAG laser.[35] A more economical alternative for generating two-colour PIV images is to use the dual flashlamp-pumped dye laser method described herein. Preliminary results from applying this technique to measure droplet velocities in a dilute heptane spray have been reported.[13,14] These two-colour methods are essentially two-frame techniques, where both frames are recorded in different layers of the same film. The images may be separated by colour and processed individually, so that particles are conceptually tracked from one frame to the next. This not only resolves the directional ambiguity, it also reduces the data processing requirements, since only half of the total number of particle images appear in each colour layer.

Other experimental approaches, which are not variants of double-pulse PIV, can be grouped into two main classes. These are single frame multi-pulse velocimetry, and multiframe tracking velocimetry, both of which are sometimes referred to as PTV (particle tracking velocimetry) techniques. The single frame multi-pulse methods inherently have limited applicability, since the optically chopped output of an argon-ion laser is used to provide the pulses. The exposure intensity is much less than that available with pulsed lasers, and the problem of blurring at high velocities mentioned earlier still exists. Under appropriate flow conditions, this method can provide exceptional accuracy due to the long distance over which a particle is tracked. These multi-pulse techniques use illumination pulse coding to resolve the directional ambiguity by inserting one or more long pulses in a train beginning and ending with a short pulse.[36,37,38]

Multiframe tracking velocimetry,[39,40,41] also referred to as digital image velocimetry,[42,43,44,45,46,47] is an extension of the dual-frame concept employed in two-colour PIV. Successive video or cinematographic frames are exposed, and the particles recorded in each are tracked from frame to frame, with the directional ambiguity being resolved by knowing the order in which the frames were acquired. Limitations of this technique are low spatial resolution and a small range of velocities. The spatial resolution is low due to the use of electronic cameras, which have up to 400 lines (interlaced) resolution for RS-170 type signals, or up to 1024 by 1024 pixels for proprietary CCD cameras. For comparison, colour 35-mm format film can have up to 6000 by 4000 pixel resolution in a frame. Since the framing rate of these cameras is fixed (30 Hz for RS-170) the motion of the particle in high speed flows is too great to be tracked from frame to frame. One major advantage of these techniques is that by avoiding film, the processing of data can begin immediately after acquisition, since the data is in electronic format.

Particle tracking methods have been extended to provide the third velocity component with limited success. These 3-D PIV techniques[48,49,50,51,52] succumb to the same limitations of the multi-pulse or multiframe methods, and often impose further limitations in order to generate the third component of velocity. These methods typically employ whole-field illumination rather than sheet illumination, and recording by two orthogonally positioned cameras. To avoid unsolvable ambiguities in matching particles, it has been shown that a third camera is necessary.[52] Whole-field illumination requires that the depth-of-field be determined by the lens characteristics rather than the sheet thickness. Also, optical access from three orthogonal directions is required, so that this is only suitable for unconfined flow or flow in transparent channels.[50,51] A unique 3-D PIV method is based on two parallel light sheets of different colours,[48] where colour is used to determine the third component of velocity in multiframe exposures. This technique is similar in complexity to two-dimensional multiframe techniques, and requires no more optical access, but the accuracy of the third velocity component is severely limited. A further limitation is that a colour CCD camera is required, which limits the image resolution to 512 by 512 pixels.

2.2 METHODS OF ANALYSIS FOR DOUBLE-PULSE PIV

There are numerous analysis techniques for extracting velocity data from double-pulse PIV images. These include Young's fringe analysis,[27] spatial autocorrelation,[27] digital convolution by Fourier transformation,[53] optical correlation,[54] cross-correlation,[55] correlation-histogram map[33] and 1-D analysis.[56] The correlation techniques relate light intensity to positional location. All of these methods are outlined below, with the exception of the correlation-histogram map technique, which is detailed in Section 3.3.2.

Briefly, the Young's fringe method involves interrogating the photographic image with a small diameter laser beam. Each particle image within the laser beam spot acts as a point source, and paired images produced by the double-pulse create the interference pattern known as Young's fringes. These fringes are oriented perpendicularly to the displacement vector, and the fringe spacing is inversely proportional to the velocity. The magnitude and orientation of the velocity are determined for the region illuminated by the laser beam.

The spatial autocorrelation method is also applied to a relatively small region, where the image of that region is shifted in relation to a second image of the same region, and the autocorrelation of intensity peaks is determined. This results in a massive self-correlation peak, and two symmetrically located displacement peaks.

Both of these methods determine the magnitude and orientation of the velocity, yet do not resolve the 180° directional ambiguity without *a priori* knowledge of the flowfield.

The digital convolution filtering method allows regions of a constant velocity amplitude or direction to be obtained from a complete image of the flow field. The convolution is calculated by multiplying the Fourier transforms of two arrays together, then taking the inverse transform of the product. The filtering is performed by convolving the digitized flow image with a mask prescribing the velocity components to be identified. This may be useful in applications where regions of fluid having similar kinetic energies need to be tracked.[53] This is a computationally intensive technique with a limited range of applications.

Optical correlation is a variant of the spatial autocorrelation technique in which the computing effort is greatly reduced. This is a two-step method, in which the light amplitude in the illuminated region of the double-pulse exposure is first recorded as a Fourier plane hologram into an electro-optic crystal. Following this, the reference beam to form the hologram is blocked, so that the crystal acts as a filter with a complex transmission function due to photoinduced refractive index modulations, and the autocorrelation function of the region is formed in the output plane.[54] This is then imaged by a TV camera, and the largest noncentral peak indicates the velocity for the region. This reduces the computational effort for analysis of the autocorrelation peaks.

Another method of reducing computational effort is the 1-D analysis technique. A region of the double-pulse exposure is imaged onto a digital camera, and then the 2-D image is compressed onto orthogonal (x,y) axes. A one-dimensional spatial correlation can then be applied to determine the x and y components of the average particle displacement.[56] This method is limited to low seed densities, where there are few particle image pairs in the interrogation spot region.

An alternative method of data reduction for the Young's fringe analysis technique is to apply one-dimensional cross-correlation algorithms to digitized images of the fringes to determine orientation and wavelength, from which velocity can be determined.[11] This method can be fully automated, and is computationally efficient.

All of these methods, with the exception of the correlation-histogram map, to be described later, were developed for monochromatic double-pulse images, and do not take account of the colour information present in two-colour PIV images. From the above examples, it can be seen that considerable effort has been expended to minimize the data reduction requirements for double-pulse analysis. The correlation-histogram map method, as explained later, is inherently efficient,[33] since the spectral separation of the first and second images eliminates approximately one-half of the possible particle images from each.

2.3 ERROR ESTIMATION IN PIV

Estimates of accuracy, resolution, reliability, and errors for PIV depend largely upon the experimental technique and the analysis method. Some results for monochromatic double-pulse systems using Young's fringe, spatial autocorrelation, and successive-frame tracking are discussed below.

For Young's fringe analysis, it has been shown that the noise contributed by photographic recording on high sensitivity moderate resolution films can be attenuated significantly.[25] This is achieved by using a gate (thin layer) of refractive index-matching fluid to remove phase distortion caused by emulsion thickness variations in the film during optical analysis. This is not necessary for high resolution films, where the phase distortion is negligible. As a result of removing this phase distortion, the dynamic range of the method can be increased by an amount equal to the increase in signal-to-noise ratio, which may be as much as 5 dB. Further improvements in measurement accuracy, through increasing the fringe signal-to-noise ratio, can be achieved through a two-step photographic process, in which a copy negative is made from the original double exposure negative to remove all sources of noise due to phase distortion.[57,58] This method also simplifies analysis, since the liquid gate is no longer necessary to remove phase distortion. This method reduces the seed density requirements for Young's fringe analysis owing to the ability to measure weaker, noisier fringes.

For spatial autocorrelation analysis, it has been shown that error in determining velocity is a function of the separation time between laser pulses, the magnification and resolution of the imaging system, and the flow velocity itself.[59] This demonstrated that the measurement accuracy of PIV was comparable to existing anemometry methods. Prasad *et al.*[60] have shown that reduced accuracies and mean bias errors were introduced as the resolution of the interrogation spot used in spatial autocorrelation (the area analyzed at one time) was reduced. If the resolution was 128 by 128 pixels or greater, the mean bias error was smaller by an order of magnitude than random errors due to imperfections in the particles, the recording process, and the data reduction process. At lower resolutions, the mean bias error was of the same order or greater than the random errors, and the number of incorrect vectors became prohibitively large, negating the gain in data reduction speed.

A detailed analysis of double-pulsed PIV systems for data reduction by spatial autocorrelation has provided optimal nondimensional values for factors affecting PIV performance.[61] The image density, which is the mean number of particle pairs per interrogation spot, should be greater than 15. The maximum relative in-plane and out-of-plane displacements should not exceed 30% of the interrogation spot diameter and sheet thickness, respectively. It was also shown that strong velocity gradients reduce the valid data rate and introduce a statistical bias. Estimates of error due to, and corrections to account for, out-of-plane motion and refractive indices other than 1 have been formulated for PIV imaging.[62]

In successive frame particle tracking, a parametric study has been performed to investigate the influence of image contrast, image noise, particle density, distribution of sizes, and frame-to-frame particle displacement on PIV accuracy.[63] It was demonstrated that, given sufficient image contrast, particle locations could be determined with sub-pixel accuracy, and the velocities could be calculated within a few percent.

2.4 PARTICLE CHARACTERISTICS FOR PIV

The characteristics of particles that are influential in PIV are the seed materials, diameter, refractive index, source density, and particle dynamics. These characteristics are interrelated, as the seed material determines the density, which affects the dynamics, and the refractive index, which affects the scattering intensity. The diameter of the particle also affects the dynamics and the scattering intensity.

Source density is the mean number of particles in a resolution cell. This cell is a cylindrical volume formed by the intersection of the laser sheet with a circle of diameter equivalent to that of the particle image projected back into the fluid.[26] This represents the mean number of particle images that overlap. For PIV, a source density of much less than unity is desirable so that the probability of image overlap is small, and images of individual particles are recorded.[26] When the source density is much greater than one, speckle occurs in the recording because many images overlap. It has been shown[26] that in most naturally or artificially seeded flows the source density is low enough to permit single particle imaging. One exception to this is in dense liquid sprays, such as in diesel fuel injection, especially when close to the nozzle.

With the exception of droplet velocimetry in liquid sprays, the objective of PIV is to determine the velocity of the surrounding fluid by measuring the velocity of entrained particles. These flows can be accelerating, can have high turbulence intensities, and can be unsteady or transient. To follow accurately the fluid in these types of flows, the particles must have excellent time response and should be spherical so that they are independent of orientation . The time response depends upon the particle diameter, density, and the fluid density and viscosity.[64,65] Small diameter and low particle density provide the best time response. The response may be characterized by the slip velocity between the particle and the surrounding fluid; this velocity should be minimized.

The scattering intensity for spherical particles used in PIV may be calculated[66,67,68] using Mie scattering theory, which will be discussed in detail in Section 3.1. Mie scattering intensity is highly dependent upon the particle diameter and is also dependent upon the relative refractive index between the particle and the fluid.[69] An alternative calculation method is the geometrical optics approach[70,71] in which the scattering is approximated from the interference of diffracted, refracted, and reflected rays. The angular region for PIV, centred around 90° from the plane of the light sheet, is dominated by surface reflection and one component of the second internal reflection.[71]

Imaging of sprays increases the complexity due to the wide distribution of droplet diameters, and thus a wide range of scattering intensities. This, along with many other factors affecting the imaging of sprays (most of which are also applicable to solid seed particles), are discussed in detail in a recent review.[12]

3 THEORY

3.1 MIE SCATTERING THEORY

The two-colour PIV technique depends upon observation of elastic scattering from particles in the flowfield. For particles of diameter $d_p << \lambda$ (where λ is the wavelength of the scattered light) the regime is referred to as Rayleigh scattering, while for particles of diameter $d_p > \lambda$ it becomes Mie scattering.[69] Mie, Debye, and Lorenz, working simultaneously but independently, all contributed to the theory which describes the physics of the interaction of a plane electromagnetic wave with a single homogeneous sphere of arbitrary diameter and refractive index.[72] This will be referred to hereafter as Mie scattering theory.

To develop a predictive capability for determining film exposure levels dependent upon experimental conditions (Section 3.2), one must know the differential scattering cross-section ($dC_{sca}/d\Omega$), which has dimensions of area, for the particle. The differential scattering cross-section is defined as the energy scattered per unit time per unit incident irradiance into a solid angle about a direction which may be specified by two angles, the scattering angle and the azimuthal angle. This can be determined from Mie theory which is described in detail in light scattering texts.[69,70,72] Bohren and Huffman[72] provide the FORTRAN source code for subroutine BHMIE, which has been modified slightly by the author of this document to provide the scattering matrix elements S_{11} and S_{12}, which are used in turn to determine the differential scattering cross-section, as described below. The modifications are to calculate the scattering matrix elements instead of the scattering efficiencies, and to do this for a user-specified number

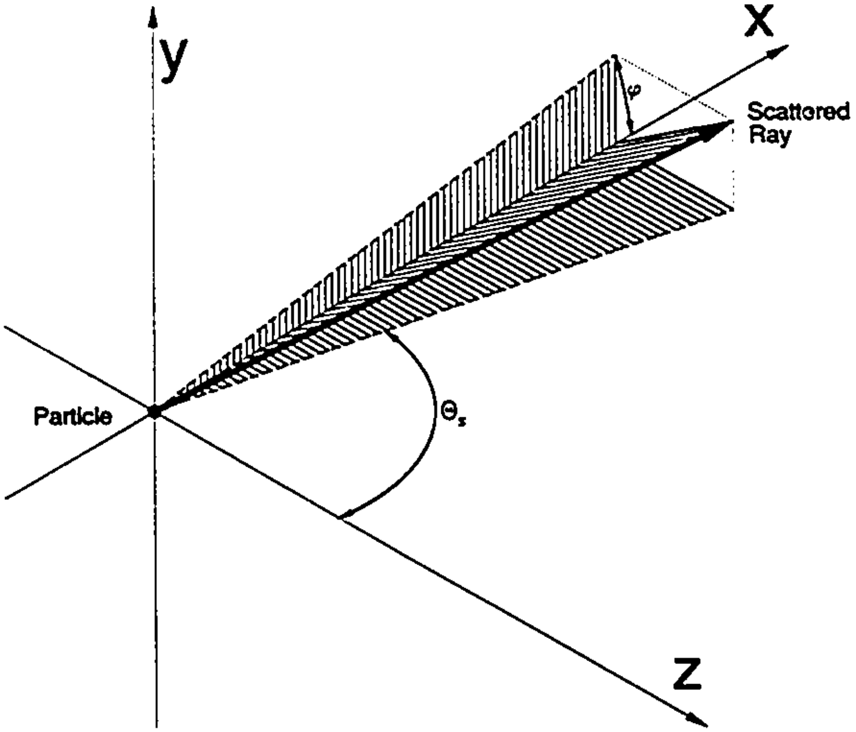

Figure 1. Arbitrary ray scattered from a particle illuminated by an incident beam propagating along the z axis.

of scattering angles symmetric about a user-specified detector angle.

The notation for the Mie theory sketched here is based on that of Bohren and Huffman. Illustrated in Figure 1 is an arbitrary particle at the origin illuminated by a plane harmonic wave propagating along the z axis. The scattering plane is defined by the z axis and the ray from the origin to the detector. This ray extends from the origin in the (θ_s,ϕ) direction, where θ_s is the deviation from the forward z-axis in the x-z plane (scattering angle), and ϕ is the deviation from the x-axis (lens axis) in the x-y plane (azimuthal angle). $E_{\parallel i}$ and $E_{\perp i}$ are the components of the incident electric field parallel and perpendicular, respectively, to the scattering plane. If the components of the electric field in the x and y directions of the x-y plane are denoted by E_{xi} and

E_{yi}, then[72]

$$E_{\parallel i} = \cos\phi \; E_{xi} + \sin\phi \; E_{yi} \quad ,$$
$$E_{\perp i} = \sin\phi \; E_{xi} - \cos\phi \; E_{yi} \quad . \tag{1}$$

The far-field region is defined as

$$k\,r \gg 1 \tag{2}$$

where r is the distance from the origin and the wavenumber, k, is defined as

$$k = \frac{2\pi n_f}{\lambda} \tag{3}$$

where n_f is the refractive index of the fluid, and λ is the free-space wavelength of the incident beam. In the far-field region, the scattered electric field can be related to the incident electric field in matrix form as[72]

$$\begin{pmatrix} E_{\parallel s} \\ E_{\perp s} \end{pmatrix} = \frac{e^{ik(r-z)}}{-ikr} \begin{pmatrix} S_2 & S_3 \\ S_4 & S_1 \end{pmatrix} \begin{pmatrix} E_{\parallel i} \\ E_{\perp i} \end{pmatrix} \tag{4}$$

where the elements of the amplitude scattering matrix, S_j, are functions of θ_s and ϕ. For spherical particles, the off-diagonal elements, S_3 and S_4, are zero. S_1 and S_2 are complex quantities that may be determined as a function of the scattering angle θ_s, the complex relative refractive index between the particle and the fluid, and the nondimensional size parameter x_p, where $x_p = kd_p/2 = \pi n_f d_p/\lambda$ (d_p is the particle diameter). S_1 and S_2 are calculated in BHMIE as functions of scattering coefficients and angle dependent functions by iterative solution of Riccati-Bessel functions. The factors S_{11} and S_{12}, used to determine the differential scattering cross-section, are related to the amplitude scattering matrix coefficients as

$$S_{11} = \frac{1}{2}\left(|S_1|^2 + |S_2|^2\right)$$

$$S_{12} = \frac{1}{2}\left(|S_2|^2 - |S_1|^2\right) \tag{5}$$

for spherical particles.

The differential scattering cross-section can be determined as[72]

$$\frac{dC_{sca}}{d\Omega} = \frac{i}{k^2} \tag{6}$$

where i is the dimensionless scattered irradiance per unit incident irradiance. The components of i representing incident light of parallel and perpendicular polarization, respectively, are denoted by

$$i_{\parallel} = \frac{E_{\parallel i}^2}{E_{xi}^2 + E_{yi}^2}\left(S_{11} + S_{12}\right)$$

$$i_{\perp} = \frac{E_{\perp i}^2}{E_{xi}^2 + E_{yi}^2}\left(S_{11} - S_{12}\right) \tag{7}$$

where $i = i_{\parallel} + i_{\perp}$. Thus, the differential scattering cross-section, as determined by Mie theory, is

$$\frac{dC_{sca}}{d\Omega} = \frac{1}{k^2}\,\frac{E_{\parallel i}^2\left(S_{11} + S_{12}\right) + E_{\perp i}^2\left(S_{11} - S_{12}\right)}{E_{xi}^2 + E_{yi}^2} \tag{8}$$

for homogeneous spheres.

For PIV, the lens axis is orthogonal to the light sheet, so that the three most common polarizations are parallel to the lens axis ($E_{yi} = 0$), perpendicular to the lens axis ($E_{xi} = 0$), or unpolarized ($E_{xi} = E_{yi}$).

3.2 EXPOSURE

Applying the Mie scattering theory of Section 3.1, the film exposure level can be determined as a function of the particle size and refractive index, the lens f-number and magnification, the laser pulse energy and light sheet dimensions, and the film sensitivity. The method of Adrian and Yao,[67] which considered black-and-white film and minimum intensities necessary to expose the film, has been extended to consider colour films and maximum intensities allowable without causing saturation. These results are applicable in the Mie scattering regime ($d_p > \lambda$).

3.2.1 Calculation of Scattered Radiation Collected by Lens

Assuming that the incident energy is distributed evenly over the area of the particle image, the mean exposure, which is the average energy density in the image plane, is equal to the time integrated irradiance scattered from the particle into the solid angle subtended by the lens, divided by the area of the particle image. The scattered irradiance per unit solid angle per unit incident irradiance is the differential scattering cross-section, $dC_{sca}/d\Omega$. From equation (6), the scattered irradiance collected by the lens is

$$\int_{\Omega} \frac{i}{k^2}\, d\Omega \tag{9}$$

where Ω is the solid angle subtended by the lens. The incident irradiance, I_o, is assumed to be uniformly distributed over the cross-sectional area of a rectangular laser light sheet, so that

$$I_0 = \frac{W}{\Delta x\, \Delta y} \tag{10}$$

where W is the laser pulse energy, Δx is the sheet thickness, and Δy is the sheet span.

The mean exposure, ε (ergs/cm^2), is represented as

$$\varepsilon = \frac{I_0}{A_e} \int_{\Omega} \frac{i}{k^2}\, d\Omega \tag{11}$$

where A_e is the area of the particle image in the film plane. Substituting Equations (3) and (10) into Equation (11) gives

$$\begin{aligned} \varepsilon &= \frac{\dfrac{W}{\Delta x\, \Delta y} \displaystyle\int_{\Omega} \frac{i}{(2\pi n_f/\lambda)^2}\, d\Omega}{\dfrac{\pi}{4}\, d_e^2} \\ &= \frac{\lambda^2}{n_f^2 \pi^3 d_e^2}\, \frac{W}{\Delta x\, \Delta y} \int_{\Omega} i\, d\Omega \end{aligned} \tag{12}$$

where d_e is the particle image diameter. Details of the algorithm used to evaluate the integral above numerically and a schematic of the geometry are found in Appendix A.

The particle image diameter can be estimated as[27]

$$d_e = \left(M^2 d_p^2 + d_s^2\right)^{\frac{1}{2}} \tag{13}$$

where M is the lens magnification, d_p is the particle diameter, and d_s is the diameter of the point response function of a diffraction-limited lens measured at the first dark ring of the Airy disk intensity distribution. This formulation for the particle image diameter represents the effects of both magnification and diffraction effects due to the lens aperture. The diameter d_s can be calculated as

$$d_s = 2.44\,(M + 1)\,f\#\,\lambda \tag{14}$$

Table II. Conditions used in calculations for Figures 2 - 4 and Figure 7.

Calculation Variable	Actual Value(s)
Laser wavelength	452.4 nm
Laser energy	330 mJ
Laser polarization	Perpendicular
Sheet thickness	1.375 mm
Sheet span	50.0 mm
Lens *f*-number	*f/5.6*, *f/11* and *f/22*
Lens magnification	0.41
Refractive index	1.388

Table III. Conditions used in calculations for Figures 5 and 6.

Calculation Variable	Actual Value(s)
Laser wavelength	694.3 nm
Laser energy	2546 mJ
Laser polarization	Perpendicular
Sheet thickness	1.0 mm
Sheet span	100.0 mm
Lens *f*-number	*f/5.6*, *f/11* and *f/22*
Lens magnification	1.0
Refractive index	1.5

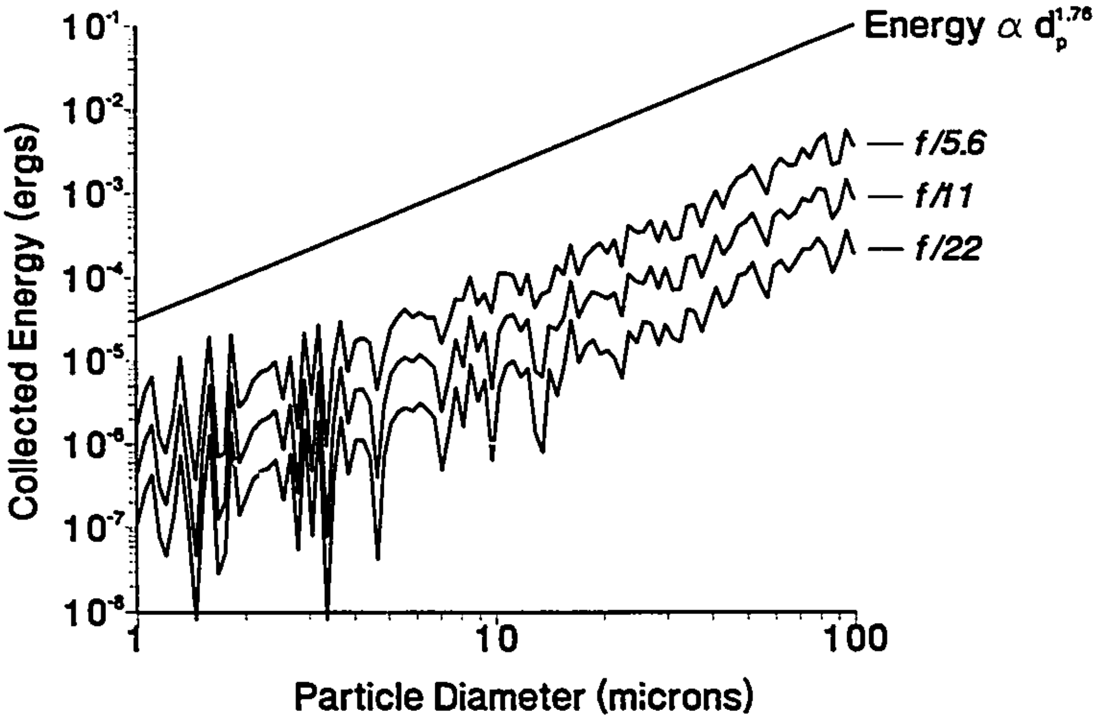

Figure 2. Scattered energy collected by lenses with apertures of *f/5.6*, *f/11* and *f/22*. The straight line indicates a functional relationship that is a best-fit to the slope of the calculated energy data.

where *f#* is the actual *f*-number of the camera lens (see Appendix B for details). The mean exposure is defined as the total energy of the particle image averaged over an area of diameter d_e. The peak exposure level will be higher, since the true particle image will have a near-Gaussian intensity distribution instead of a uniform one.[67]

The mean exposure calculated by this method can be used as a guideline in setting experimental conditions, such as laser energy, lens aperture, and film sensitivity. The true exposure will vary within the particle image due to the variation of intensity across the image,

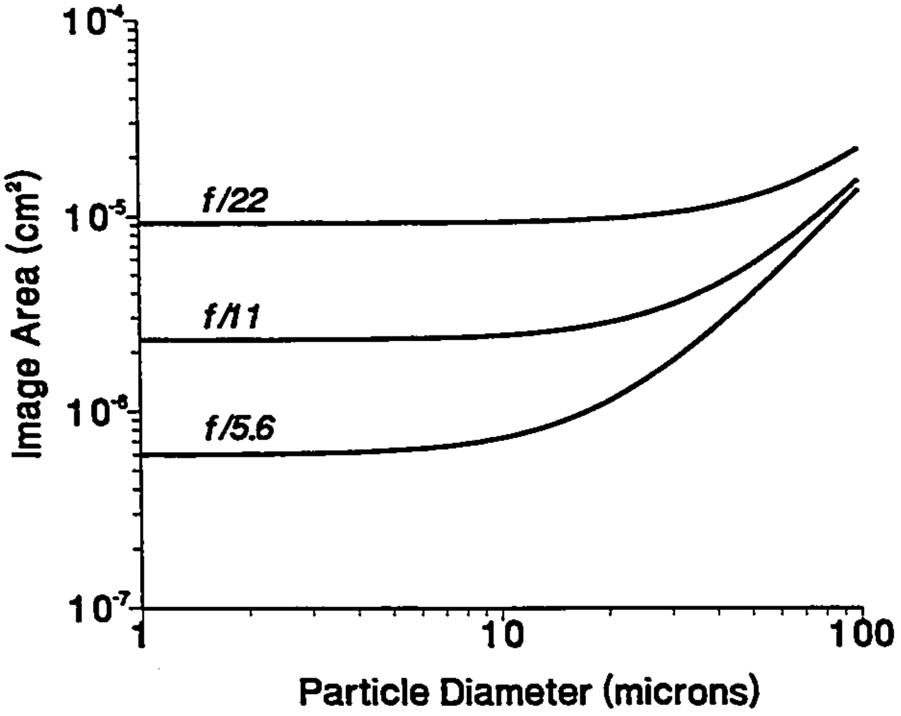

Figure 3. Image area as a function of particle diameter for lens apertures of *f/5.6*, *f/11* and *f/22*.

and it will also vary depending upon the particle location. This sensitivity to location is due to the nonuniformity of intensity across the laser sheet cross-section, and due to variation of the scattered irradiance with position in the field-of-view of the camera. For calculation purposes, the particle is assumed to be on the lens axis, so that the primary scattering angle is 90°. Particles nearer to the laser source will have a slightly higher intensity, since the scattering angle will be less than 90°, and forward scattering is more intense than backscattering. The opposite is true for particles furthest from the laser source. Particles that are away from the lens axis in the direction of the span of the laser sheet will also vary in scattered irradiance depending upon

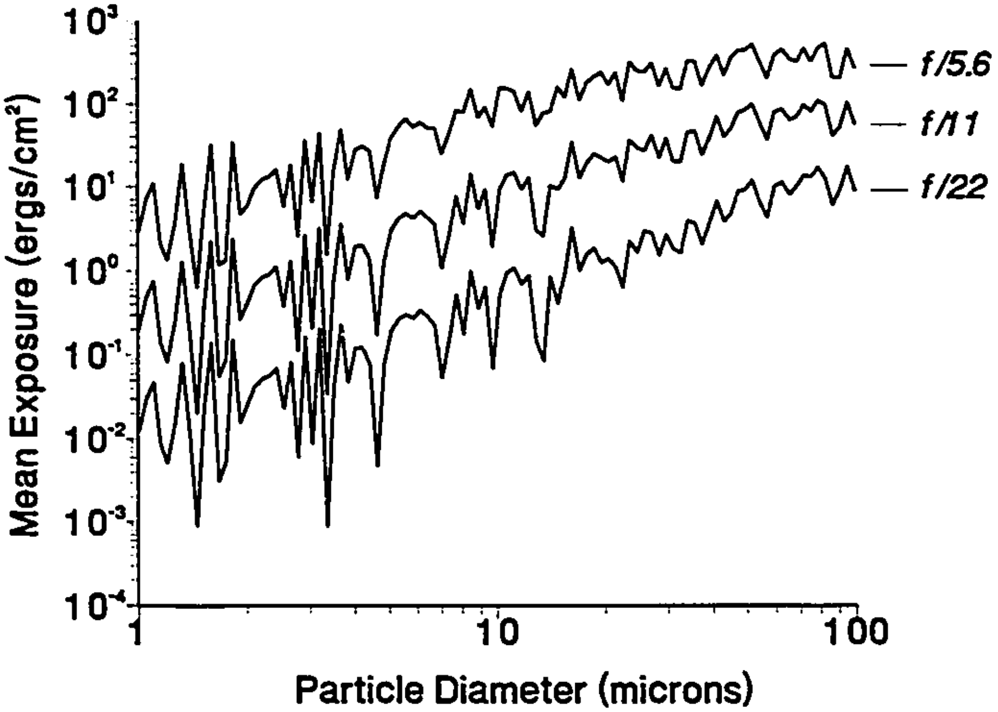

Figure 4. Mean exposure as a function of particle diameter for lens apertures of *f/5.6*, *f/11* and *f/22*.

the polarization orientation of the incident laser beam with reference to the lens axis. However, these variations are minor in comparison to the variation in mean exposure as a function of particle diameter, relative refractive index, lens aperture, and laser energy and sheet dimensions. Adrian and Yao[67] found that for $d_p << d_s$, the mean exposure was proportional to $f\#^4$, since d_e was essentially independent of d_p, while for $d_p >> d_s$, the mean exposure was proportional to $f\#^2$.

Figure 2 shows the results of sample calculations of the scattered energy collected by the lens. The quantities used for the variables are summarized in Table II. From linear regression of the results presented, the energy collected by the lens is proportional to $d_p^{1.76}$ in the Mie

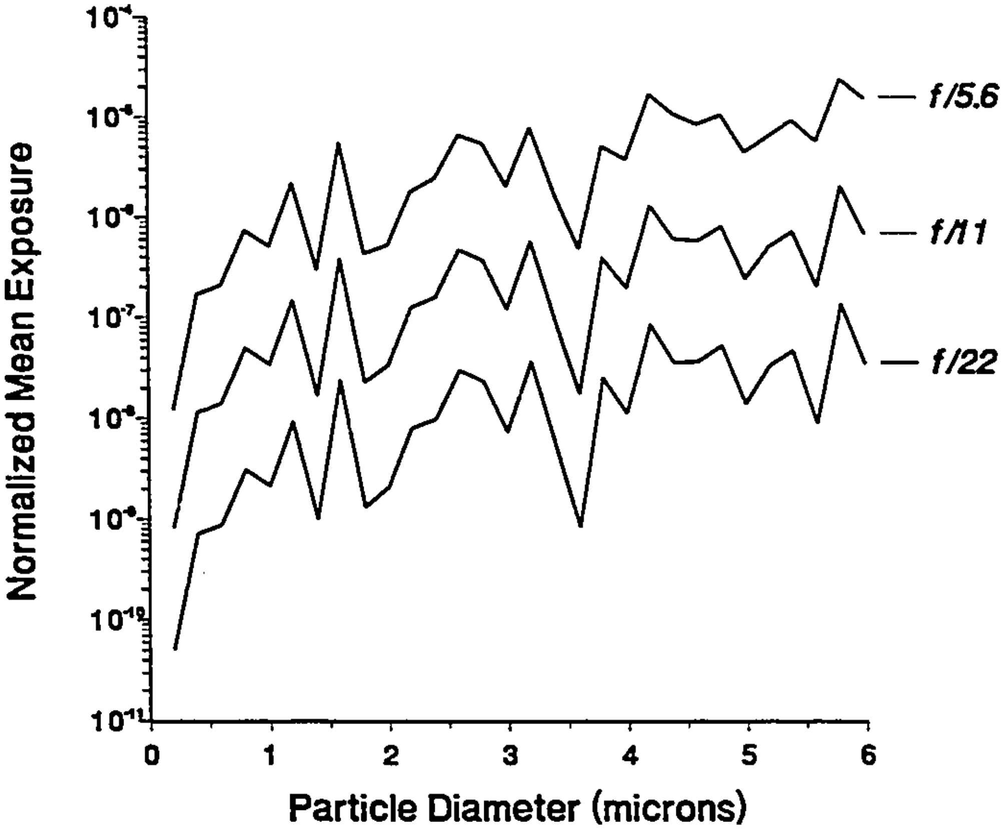

Figure 5. Scattering intensity calculations performed at conditions in Table III, and at diameters spaced 0.2 μm apart.

scattering regime. Figure 3 shows how the diffraction-limited spot size can dominate the particle size in determining the area of the particle image.

The mean exposure, which represents the collected energy distributed uniformly over the image area, is shown as a function of d_p in Figure 4. As the lens aperture is enlarged, the diameter at which d_e is proportioned to d_p is reduced, and the mean exposure goes from being proportional to $d_p^{1.76}$ to being independent of d_p.

Before proceeding further, a comparison was performed between the predictions made here and those of Adrian and Yao.[67] The results determined here (see Figure 5 above) were

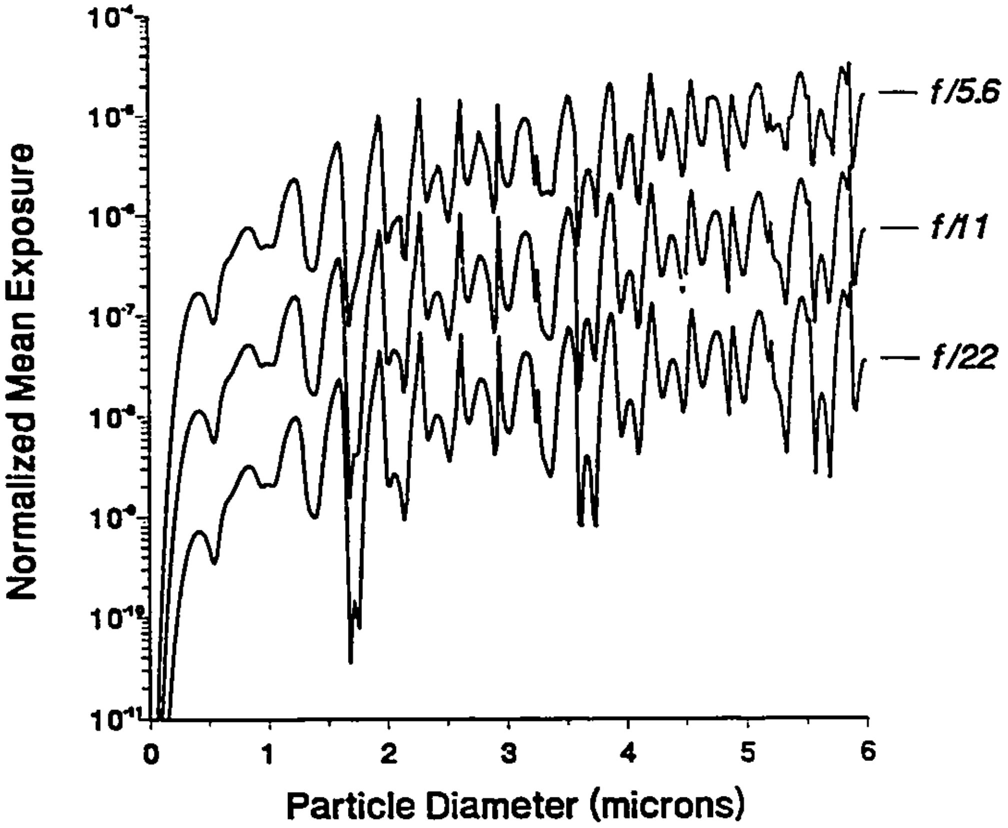

Figure 6. Scattering intensity at the same conditions as Figure 5, calculated at diameters spaced at 0.02 μm apart.

calculated at identical conditions (Table III) to those of Adrian and Yao (Figure 6 of reference 67). This indicated excellent agreement, with the plotted results having similar shapes and magnitudes to those of Adrian and Yao.[67] For the comparison, the mean exposures are normalized by the average energy density of the laser sheet. As a further comparison, a hand calculation of normalized mean exposure for a single particle diameter was performed, assuming that the scattered irradiance was constant over a small field-of-view (provided by an aperture of f/22). The result of this was within 2% of the computed value.

The oscillations in the magnitude of the mean exposure may be due to resonances relating

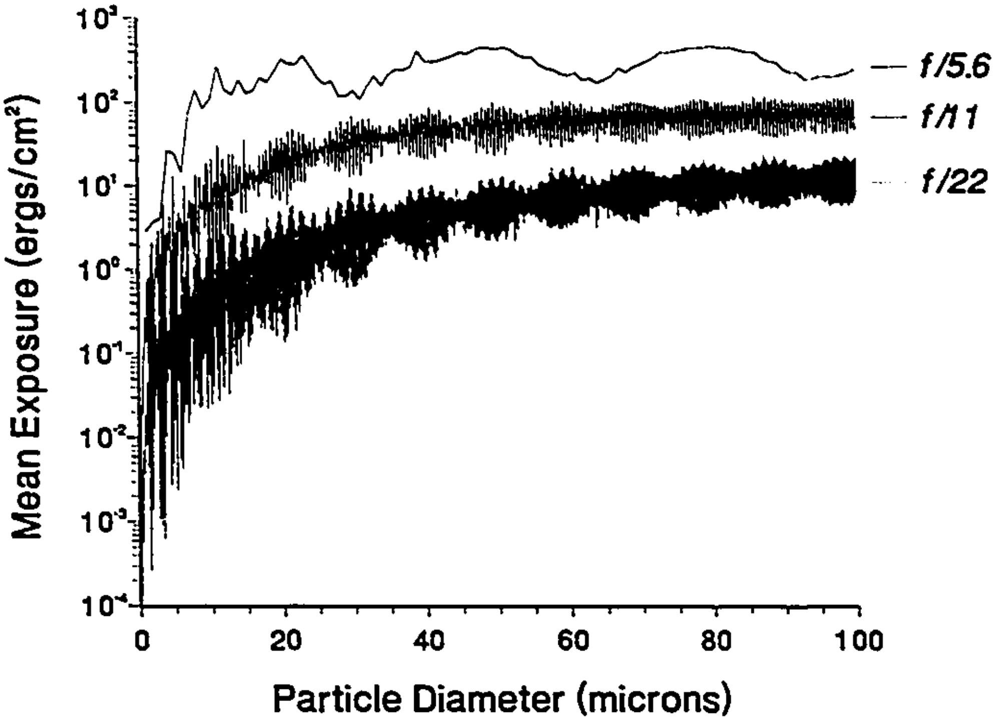

Figure 7. Scattering calculations for heptane droplets determined at diameter intervals of 1.0 µm (*f/5.6*), 0.1 µm (*f/11*), and 0.01 µm (*f/22*).

investigation, it was discovered that the frequency of the oscillations was much higher than shown by the calculations presented in Figure 5. The results for the same conditions, calculated at an order of magnitude more particle diameters, are shown in Figure 6. The period of these oscillations appears to be about 0.15 µm, so to observe the magnitude of the oscillations, the intervals between particle diameters used for the computations should be 0.03 µm or less. For computations over a wide range of particle sizes, to observe the trend of the mean exposure, a larger interval may be used to reduce the execution time. This is illustrated in Figure 7, where the curves are calculated at intervals of 1 µm for *f/5.6*, 0.1 µm for *f/11*, and 0.01 µm for *f/22*.

The calculated results presented are in the range $0\ \mu m < d_p \leq 100\ \mu m$, as this is the expected extent of the droplet size distribution in a fuel spray.

3.2.2 Colour Film Response

To apply the information acquired by calculating the mean exposure levels, the exposure characteristics of the detector must also be quantified. As will be discussed in Section 4.1.3, colour film is the best choice for detecting two-colour PIV images. Colour film is composed of three primary layers, sensitive to blue, green, and red wavelengths. A typical spectral-sensitivity curve[73] (see Figure 8) shows that for most wavelengths there is cross-sensitivity between these layers. For optimum performance from the two-colour technique, it would be ideal to have each of the colours exposing just one layer of the film. To achieve this, the exposure in the unwanted cross-sensitive layers must be kept below the minimum density (D_{min}), also known as the gross fog level, which is the level of exposure at which each layer of film begins to respond. Optical

Table IV Exposure levels required to meet specified densities for two colour films

Exposure (ergs/cm^2)	Kodak Ektar 125				Kodak Gold 100				
	λ=452.4 nm		λ=543.7 nm		λ=452.4 nm		λ=543.7 nm		
Film Layer	Blue	Green	Green	Red	Blue	Green	Blue	Green	Red
@ D_{min}	.0005	.0112	.0002	.0075	.0026	0.317	3.17	.0040	0.824
@ $D_{1.0}$	.0117	0.42	.0085	0.53	.0585	9.05	70.3	0.113	36.1
@ D_{max}	0.419	7.92	0.160	6.53	4.21	323	5062	4.02	616

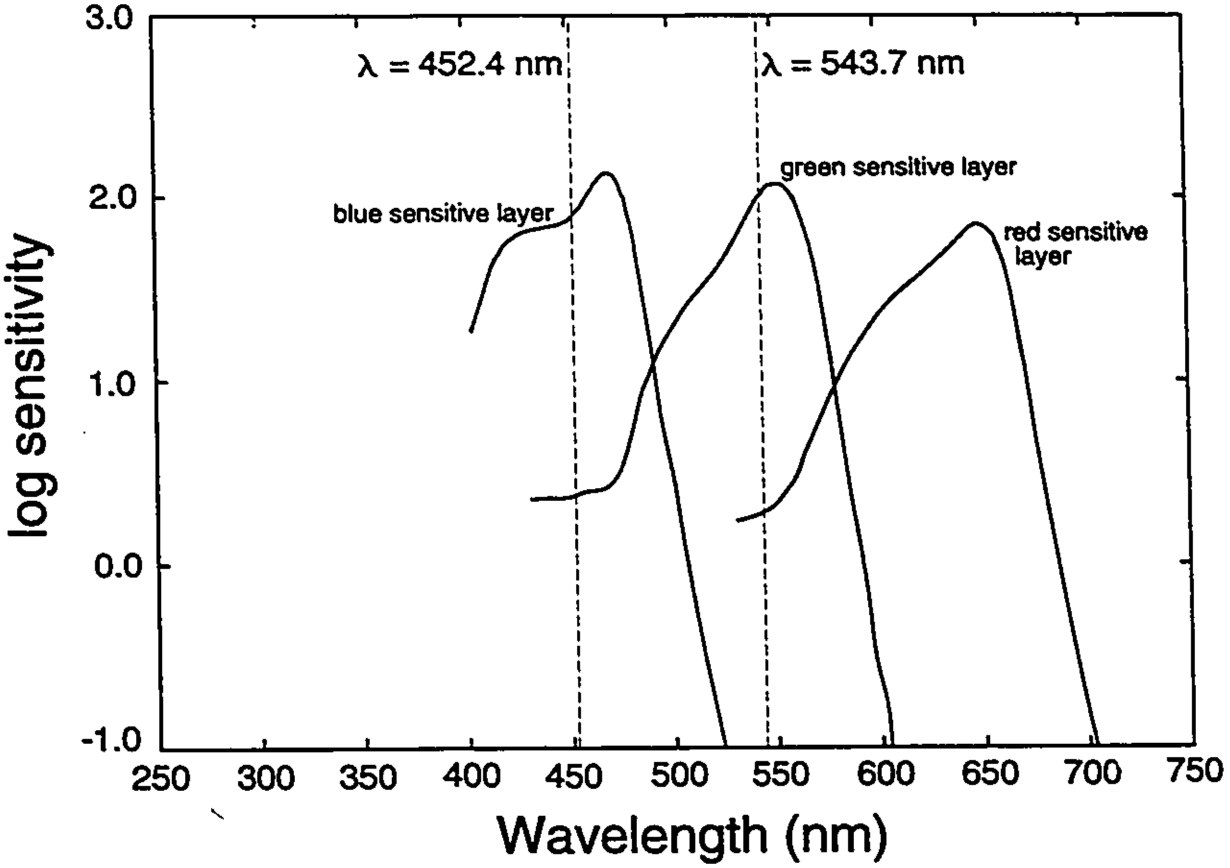

Figure 8. Spectral sensitivity curves for Kodak Ektar 125 colour film (with laser wavelengths indicated by dashed lines).

density is equal to the logarithm to the base 10 of the inverse transmittance of the film. A density of 1.0 above D_{min} (an order of magnitude decrease in transmittance) is considered to be the level necessary for good exposure. It is therefore desirable to have an exposure level such that the target layer has a density greater than 1.0 above D_{min}, while the other layers have densities less than D_{min}.

The spectral-sensitivity curves are typically published for a density of 1.0 above D_{min}. The exposure (in ergs/cm^2) at this density is simply the reciprocal of the sensitivity for a particular wavelength and layer of the film. To determine the exposure at other densities, one must use the

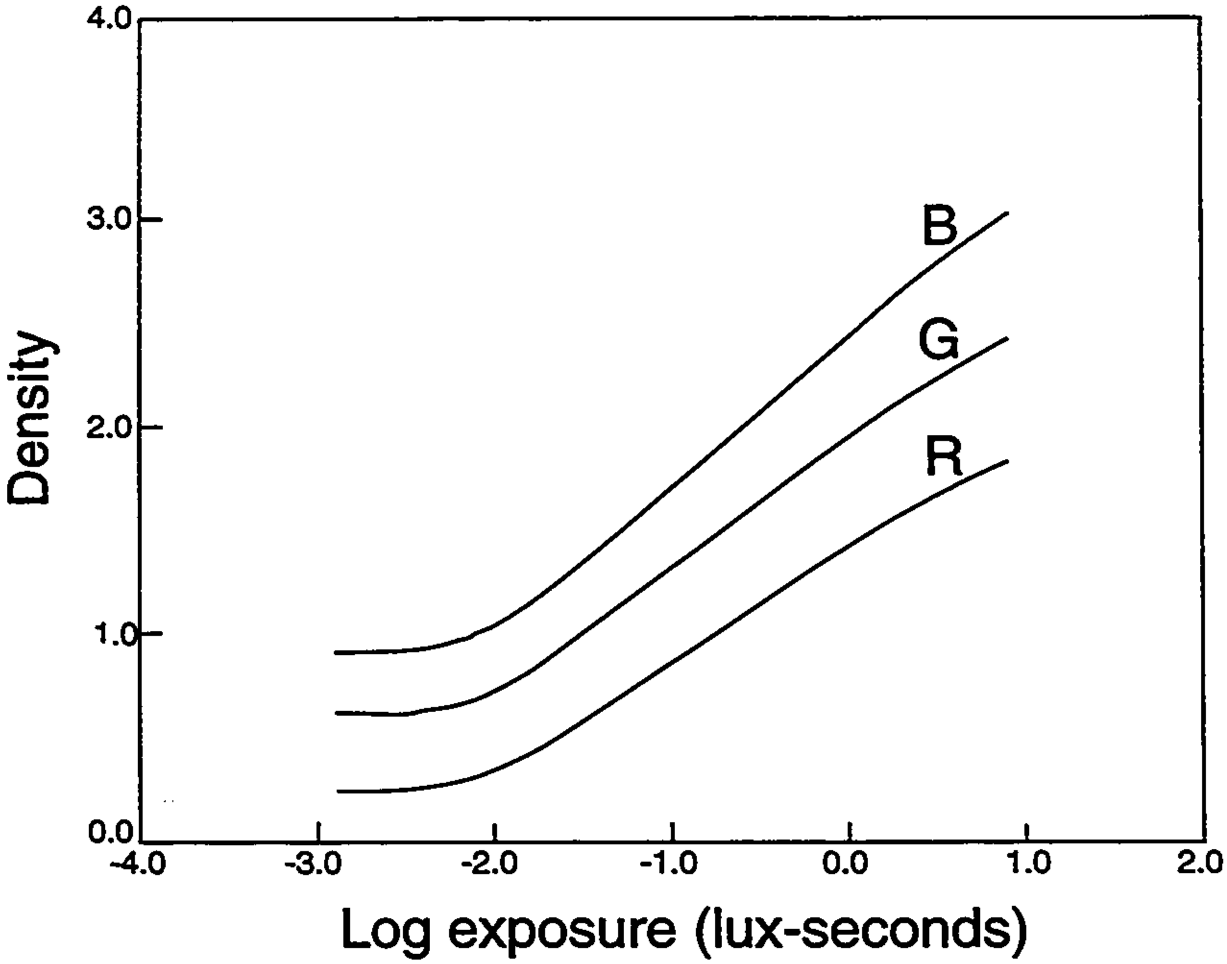

Figure 9. Characteristic curves for individual layers of Kodak Ektar 125 colour film.

characteristic curves, which relate density to exposure for each of the three layers[73] (see Figure 9). The low end of these curves is at D_{min}, the gross fog level, the high end is at D_{max}, the level beyond which increased exposure will not produce increased density (saturation), and the slope is the gamma (γ) for the film, which is proportional to the degree of contrast. All three of these characteristics have independent values for each layer of the film. The exposure at an arbitrary density D_x above D_{min} is represented by $\varepsilon_x(\lambda,L)$ where λ is the laser wavelength and L

is the layer of film. The exposure can be determined in the constant gamma region as[74]

$$\varepsilon_x(\lambda,L) = \varepsilon_{1.0}(\lambda,L)\ 10^{\left(\frac{D_x(L) - D_{1.0}(L)}{\gamma(L)}\right)} \qquad (15)$$

where $D_{1.0}(L)$ is the density of 1.0 above D_{min} for the specified layer, $D_x(L)$ is the density at which the exposure is to be determined, $\gamma(L)$ is the slope for the specified layer, and $\varepsilon_{1.0}(\lambda,L)$ is the exposure determined from the spectral sensitivity curves (at a density of 1.0 above D_{min}) for the laser wavelength and film layer specified.

Exposures resulting from these calculations for two films are presented in Table IV. The first film is Kodak Ektar 125, which has very high resolving power (160 lines/mm at a test-object-contrast of 1000:1) and moderately wide exposure latitude.[73] The second film, Kodak Gold 100, has high resolving power (100 lines/mm at a test-object-contrast of 1000:1) and excellent exposure latitude.[75] As revealed in Table IV, with Kodak Ektar 125 it is impossible to have an exposure that exceeds a density of 1.0 above D_{min} in the desired layer while keeping the other layers below the gross fog level for either the blue or the green laser wavelengths. The same is not true for Kodak Gold 100, where blue laser (452.4 nm) exposures of 0.0585 ergs/cm^2 < ε < 0.3172 ergs/cm^2 will

Table V. Conditions used in calculations for Figures 10 and 11.

Calculation Variable	Actual Value(s)
Laser wavelength	452.4 nm(blue) 543.7 nm (green)
Laser energy	330 mJ (blue) 352 mJ (green)
Laser polarization	Perpendicular
Sheet thickness	1.375 mm
Sheet span	50.0 mm
Lens *f*-number	*f/8*, *f/16* and *f/32*
Lens magnification	0.41
Refractive index	1.388

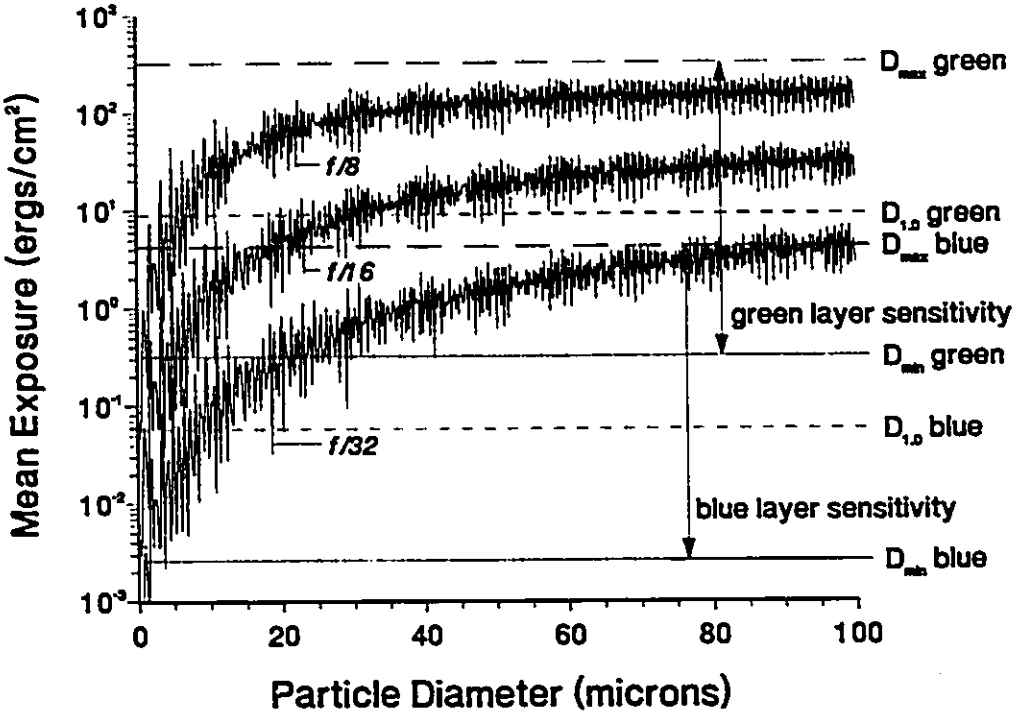

Figure 10. Scattered intensity from n-heptane droplets exposed to blue laser, compared with film sensitivity for Kodak Gold 100 colour film.

meet both conditions, as will green laser (543.7 nm) exposures of $0.1130 \text{ ergs/cm}^2 < \varepsilon < 0.8241 \text{ ergs/cm}^2$.

These results for Kodak Gold 100 film are shown graphically for the blue laser (Figure 10) and the green laser (Figure 11), where mean exposure calculations for n-heptane fuel droplets are combined with the film exposure data. The conditions for these mean exposure calculations are the same as those for the experiments reported in Section 5, and are listed in Table V. From these curves, one may observe that at the specified conditions, a lens aperture of *f/32* will provide the best exposure results over the widest range of droplet sizes.

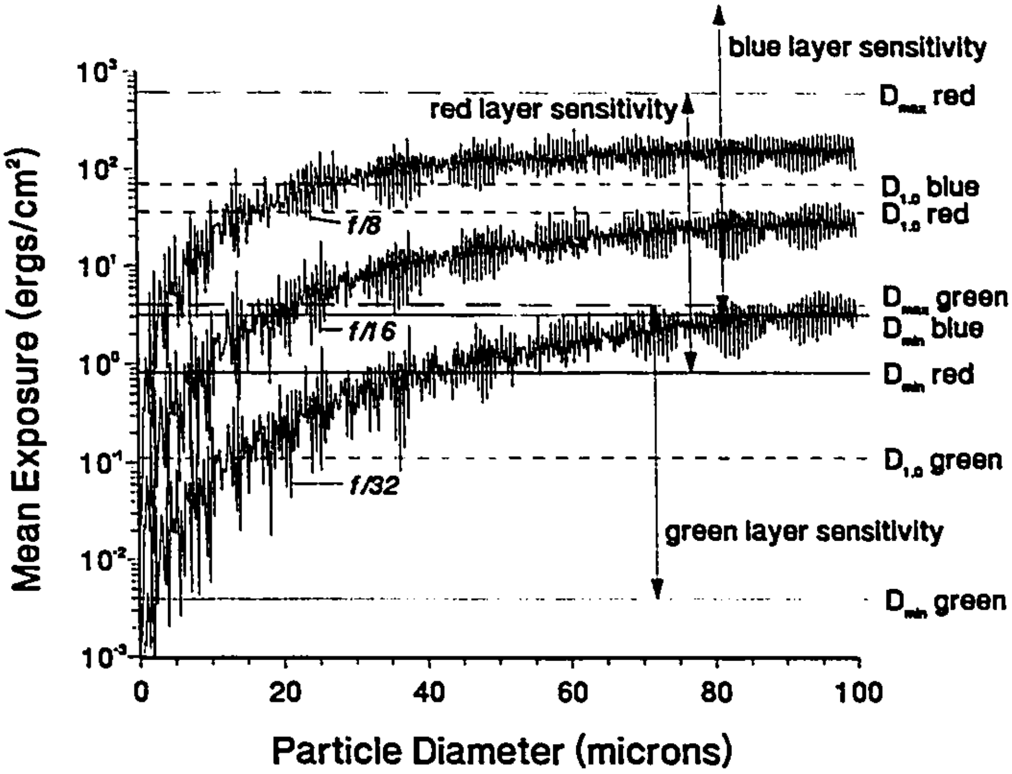

Figure 11. Scattered intensity for n-heptane droplets exposed to green laser, compared to film sensitivity for Kodak Gold 100 colour film.

The mean exposure analysis relates the seed particle, fluid, laser, camera, and film characteristics and can be used to estimate the conditions necessary for a good exposure. In practice, some trial-and-error adjustment about the prescribed conditions may be required.

3.3 IMAGE ANALYSIS PRINCIPLES

The approaches most often used for conventional double-pulse monochromatic PIV analysis are the Young's fringe method[27] and the spatial autocorrelation method.[27] Other methods attempted are cross-correlation[28] and optical correlation.[54] However, these methods do not recognize the additional information contained in the two-colour images which can permit the true direction of the velocity vectors to be determined. The histogram-correlation map method can account for the two separate colour images. This is the technique used, and it is described in Section 3.3.2.

The software used here to analyze the two-colour PIV images, the MPTRS code (Mike Post TRacker Software), was graciously donated to the National Research Council by Systems Research Laboratories, Inc. It is based on a Digital Equipment Corporation VAX FORTRAN code developed by L. P. Goss, M. E. Post, and L. F. Brainard. It has been implemented on a 25 MHz Intel 80386 processor-based PC compatible computer using a 32 bit compiler, Microway NDP FORTRAN-386. This code is used to identify particles, determine the most probable velocity vector, and then track individual particles. Due to computer memory limitations, the full image (up to 6144 x 4096 pixels) is split into manageable subimages of 1024 x 1024 pixels or less before processing and analysis. A detailed description of the analysis software exists elsewhere;[33] however, a brief overview will be outlined in the following sections.

3.3.1 Identification of Particle Locations

The analysis is performed on a digital image (maximum of 1024 x 1024 pixels) with 24 bits of colour depth per pixel, 8 bits (256 intensity levels) each of red, green, and blue (RGB). The laser wavelengths are in the blue and green portions of the visible spectrum (see Section 4.1.1), so upon reading in the image, the blue and green components are separated and the red data is discarded. The blue and green images are then treated as separate monochrome images for the purpose of locating particles in each, and the following procedures are applied to both of them.

A two-dimensional Laplacian operator is applied to remove background variation and noise. This background may be due to film granularity, scattering from out-of-focus particles, or scattering from solid objects in the flowfield, for example. This operator is equivalent to a spatial frequency filter, passing only high frequency components. The image is then scanned in two dimensions to find local maxima. The four criteria used to determine if the local maxima are particle centres are that the intensity should be above a minimum threshold, that they are not shoulders of a larger peak, that the local average intensity is greater than another threshold, and that the diameter is within minimum and maximum size limits. The first criterion is applied to ensure that the maximum is greater than the background level, and the second is to determine whether the maximum is in the vicinity of greater maxima (shoulders or secondary peaks may appear due to uneven contouring of the intensity profile). The third criterion is to eliminate background noise spikes of high intensity that satisfy the first two conditions. The maximum for a particle is typically surrounded by pixels of similar intensity, so that the average would discriminate against noise spikes. The intensities of the pixels surrounding the maximum are then applied to calculate a weighted average to determine the intensity centre of the particle image. The location of this intensity centre is determined by a method analogous to calculating a centre of mass. The fourth criterion is applied by measuring the FWHM (full width of half maximum) diameter from the intensity centre in orthogonal directions. The minimum diameter should be set to slightly less than the image diameter of the smallest anticipated particle, and the maximum diameter should be set larger than the image diameter of the largest anticipated particle. However, the maximum diameter should also be smaller than any solid objects visible in the photographic image. If all of these criteria are met, then the intensity centre is identified as the location of a particle image.

3.3.2 Determination of the Most Probable Velocity Vector

The image is separated into a user-specified number of sections, determined to some degree by the anticipated complexity of the flowfield. For flows dominated by translation, the entire image (up to 1024 x 1024 pixels) may be analyzed. However, flow regions dominated by solid body rotation require several sections, owing to the significant directional variations in the velocities. Each section should be sufficiently small that the velocity is essentially constant within it, yet large enough that a significant number of blue/green image pairs are present. Statistically, it is recommended that there be a minimum of ten image pairs in a given section.[3]

Within each section, the histogram-correlation map approach is used to find the representative velocity for that section. The analysis software copies a region of the green image, sized according to the maximum anticipated velocity and centred on each blue particle image, into a correlation map. This is repeated in turn for all of the blue particle images, so that multiple regions of the green image are superimposed on each other. This is represented mathematically by[33]

$$H(\xi,\psi) = \sum_{n} b(x_c, y_c)\, g(x_c-\xi, y_c-\psi) \tag{16}$$

where $H(\xi,\psi)$ is the correlation histogram, $b(x_c, y_c)$ are the intensities at the centre locations of the blue particle images, $g(x_c-\xi, y_c-\psi)$ are the intensities of the green images located surrounding each blue particle image shifted by (ξ, ψ), and the summation is performed over all the blue particle images. Peaks will appear on this map at locations where blue/green particle image pairs have the same displacement and direction. The greatest peak indicates the direction and magnitude of the most probable velocity vector for that section.

If this had been a conventional double-pulse monochromatic PIV image, the analysis would have produced a correlation map with a maximum at the origin, indicating a self-correlation peak, and two velocity peaks arranged symmetrically about the self-correlation peak. This results in the 180° directional ambiguity symptomatic of conventional PIV. As shown, the two-colour method determines a unique velocity for each section analyzed.

3.3.3 Tracking of Individual Particles

Actual particle velocities are determined by matching blue/green particle images. The origin of the representative velocity vector for each section is applied to the intensity centre of every blue particle image in the section, and a search for a corresponding green particle image at the opposite end of this vector is undertaken. This search involved opening a "window" of increasing dimension centred at the most probable green particle image location (the end of the vector) until a matching green particle is found, or else limits for variance in direction or magnitude are exceeded, in which case the blue particle image is discarded. If a match is found, then an individual particle velocity vector has been determined. The final result is a number of these individual velocity vectors for each section in the image.

3.3.4 Interpolation of Velocity Vectors

The velocity vectors determined by the two-colour PIV technique are located randomly throughout the flowfield, according to the distribution of particles (droplets) within the field-of-view. For comparison with computer models or with point measurements, both of which commonly use a uniformly spaced grid, it was necessary to generate a velocity map with vectors at specified locations. This was achieved by interpolating the existing randomly located vectors within a user-specified fixed distance of the desired location. The vectors were weighted inversely according to their distance from the desired location, as represented by

$$\left[V_x(x_i, y_i), V_y(x_i, y_i)\right] = \frac{\sum_{i=1}^{n} \frac{\left[V_x(x_b, y_b), V_y(x_b, y_b)\right]}{\left[(x_b - x_i)^2 + (y_b - y_i)^2\right]^{\frac{1}{2}}}}{\sum_{i=1}^{n} \frac{1}{\left[(x_b - x_i)^2 + (y_b - y_i)^2\right]^{\frac{1}{2}}}} \qquad (17)$$

where (x_i, y_i) was the specified coordinate location for calculating the interpolated velocity, (x_b, y_b) was the coordinate for the initial point (blue particle image) of a measured random velocity vector, $V_x(x_i, y_i)$ and $V_y(x_i, y_i)$ are the x and y components of the interpolated velocity vector, and n is the number of random vectors within the specified fixed distance of the interpolation location.

In the example of a spray, the velocities measured are the droplet velocities, not the fluid velocities (unlike the intention in seeded PIV). At the periphery of the spray the interpolation routine could produce vectors outside of the spray cloud. To avoid this, the vectors were not projected by interpolation or extrapolation to fill regions where there were no droplets within the specified fixed distance of the interpolation location. Also, the fixed distance for random vectors to be included in the interpolation calculation was the same as the spacing of the interpolation grid. Combining this with the inverse-distance weighting resulted in data that was minimally smoothed, affected only by random vectors closer than the nearest interpolation points. For the special case of $n = 1$, the fixed distance was reduced to one-half of the grid spacing, so that only the closest interpolation point was represented by the measured vector, in order to avoid projection into regions with no random vectors.

For seeded flowfields, where the objective is to measure fluid velocities, the distance over which the randomly spaced vectors are interpolated may be increased to greater than the grid spacing. As this distance is increased, the regions where there are no random vectors will be filled with an interpolated vector based on the neighbouring vectors, again with inverse-distance weighting. Increasing this distance can be used to smooth data, if so desired.

4 EXPERIMENTAL METHOD

The particle image velocimetry (PIV) technique is intended to be applied to a wide range of flow conditions that may be encountered in combustion studies. Both combusting and noncombusting flows must be considered. The velocities anticipated range from below 1 m/s in laminar flames to over 200 m/s in Diesel fuel sprays. Recirculation zones and flow reversal are common in combustion-related flows and need to be identified. The scale of the particles imaged range from less than 1 μm for seed particles added to air flows to over 100 μm for the larger droplets in sprays.

The following sections describe the two-colour technique that has been developed to meet these requirements while producing images suitable for analysis by the PIV method described earlier.

4.1 EXPERIMENTAL CONSIDERATIONS

4.1.1 Laser Selection

Conventional monochromatic double-pulse PIV is performed by optically chopping the output of a *cw* (continuous wave) gas laser, by using a high frequency pulsed gas laser, by double pulsing a solid state pulsed laser, or by using two solid state pulsed lasers. With these systems a single frame is double-exposed with the same wavelength radiation, leaving the directional ambiguity problem to be resolved. None of these systems offers the degree of flexibility required for the broad range of experiments the two-colour PIV technique is intended to be applied to. The possible lasers emitting radiation in the visible wavelengths required for the two-colour method are listed in Table VI and the important details are described below.

The most limited choice would be an argon-ion *cw* laser, which would have its output separated into the two strongest lines (514.5 nm and 488.0 nm); the beam would then either be optically chopped or scanned by reflecting it from a rotating or oscillating mirror. This would create a quasi-pulse with a duration of the order of 1 ms, which would be suitable only for slowly moving particles. A reasonable criterion for acceptable blurring due to particle motion

Table VI Potential lasers for two-colour PIV

Laser	Pulse Duration	Maximum Pulse Energy	Wavelengths (nm)	Advantages	Disadvantages
Argon Ion	1 ms	20 mJ	488.0; 514.5	none	long pulse, low energy
Copper vapour	40 ns	5 mJ	510.6; 578.2	short pulse	low energy, not tunable
Nd:YAG + dye	10 ns	50 mJ	532; 570–700	short pulse	fixed separation, only one laser is tunable
2 Nd:YAGs (pumping 1 or 2 dye lasers)	10 ns	100 mJ	400–700; 400–700	short pulse, high energy, tunable, variable separation	expensive
2 flashlamp pumped dye lasers	40 ns 300 ns	100 mJ @40 ns 500 mJ@300ns	400–700; 400–700	short pulse, high energy, tunable, variable separation	none

during the illumination period is

$$\Delta d \leq 0.5\, d_e \tag{18}$$

where Δd is the particle motion and d_e is the particle image diameter. Applying this to the velocity equation ($V=d/t$) results in

$$V_p \leq \frac{0.5\, d_e}{\Delta t} \tag{19}$$

where V_p is the particle velocity and Δt is the illumination period. A 100 μm particle moving at greater than 0.05 m/s during a 1 ms period would create unacceptable blurring. With *cw* lasers, reducing the illumination period reduces the energy proportionately, so that any gain in maximum velocity is offset by insufficient illumination. The two principal wavelengths are close, and it may be difficult to separate the images acquired. Thus, the argon-ion laser would only be suitable for very low velocity flows with large seed particles.

Pulsed lasers avoid the problem of motion blurring, except at very high velocities, owing to the short pulse durations of 10 ns to 300 ns. A 10 μm particle illuminated for 40 ns could have a velocity as high as 125 m/s before exceeding the blurring criterion.

A copper-vapour laser, which is a high frequency pulsed gas laser, would require its two wavelengths to be separated and then switched on sequentially by placing a Pockels cell in each of the beams. This would limit the time interval between pulses to multiples of the repetition period for the laser. Although this would be a straightforward arrangement, it would only produce about 5 mJ of energy in each of the beams, which is not enough energy to image small particles. The wavelengths are at the high end of the visible spectrum, and thus the images

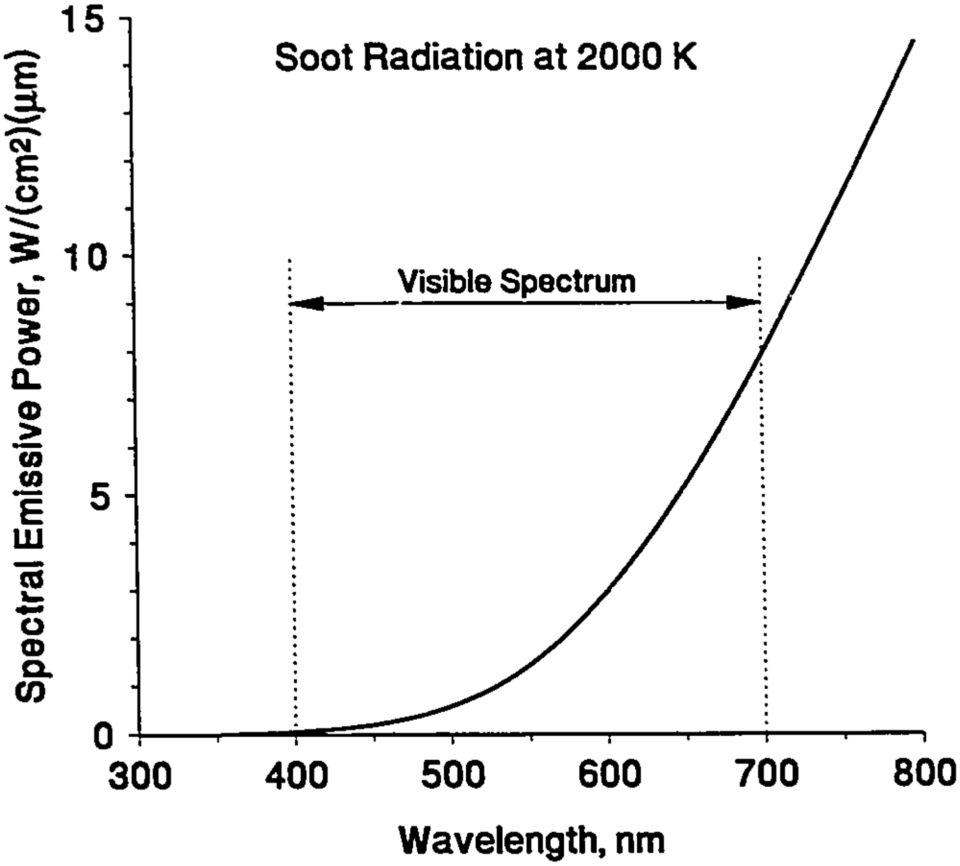

Figure 12. Soot radiation as a function of wavelength.

would be prone to interference from combustion radiation. This is illustrated in Figure 12, which shows that soot radiation increases dramatically from the low end of the visible spectrum to the high end. The cost of such a system would be about $150,000, which makes it moderately expensive. This system could be used with large particles in a non-luminous environment.

There are two feasible methods for creating two-colour pulsed illumination using solid-state lasers. The first is to double-pulse a frequency-doubled Nd:YAG laser, diverting a portion of the energy to pump a dye laser, and then using Pockels cells in each beam to sequentially allow first one, then the other, to be transmitted. The limitations imposed by this proposal are that the temporal separation between laser pulses is fixed (of the order of 100 µs), and the dye laser is only tunable from 570-700 nm, which is not a desirable range due to increased soot radiation at higher wavelengths. The second method is to use two Nd:YAG lasers, either with both frequency-tripled and used to pump dye lasers, or with one frequency-tripled to pump a dye laser and the other emitting frequency-doubled radiation. This allows a wide range of flow velocities to be studied due to the variable separation (each laser may be triggered independently) and the short pulse duration. The high energy permits small particles to be observed, and blue-green wavelengths can be selected to minimize interference from combustion radiation. This arrangement provides the flexibility necessary, at high cost ($250,000) and complexity. A similar apparatus with the same flexibility could be arranged using two excimer lasers, each pumping a dye laser, but this would be even more costly.

A more economical, less complex solution is to use two flashlamp-pumped broadband dye lasers. This provides the flexibility required for approximately $50,000. These lasers provide ample energy, tuning over the entire visible spectrum, and variable time separation between the two laser pulses. For high velocities, where motion blurring may become a factor, the pulse width, which is normally 300 ns at the full width of half maximum (FWHM), can be reduced to as low as 40 ns by inserting external Pockels cell pulse slicers into the beams (see Figure 13). The weakness of this approach is that it reduces the beam energy. Since the blurring criterion is proportional to particle diameter, it will be the smaller particles that require shorter pulse durations for a given velocity. However, smaller particles have a smaller scattering cross-section which, combined with the reduced laser energy, may lead to insufficient illumination.

Except for very high velocity flows with small particles, where two dye lasers pumped by two Nd:YAG lasers or two excimer lasers would be the only solution, the dual broadband flashlamp pumped dye lasers have the range of operating conditions, along with economy and

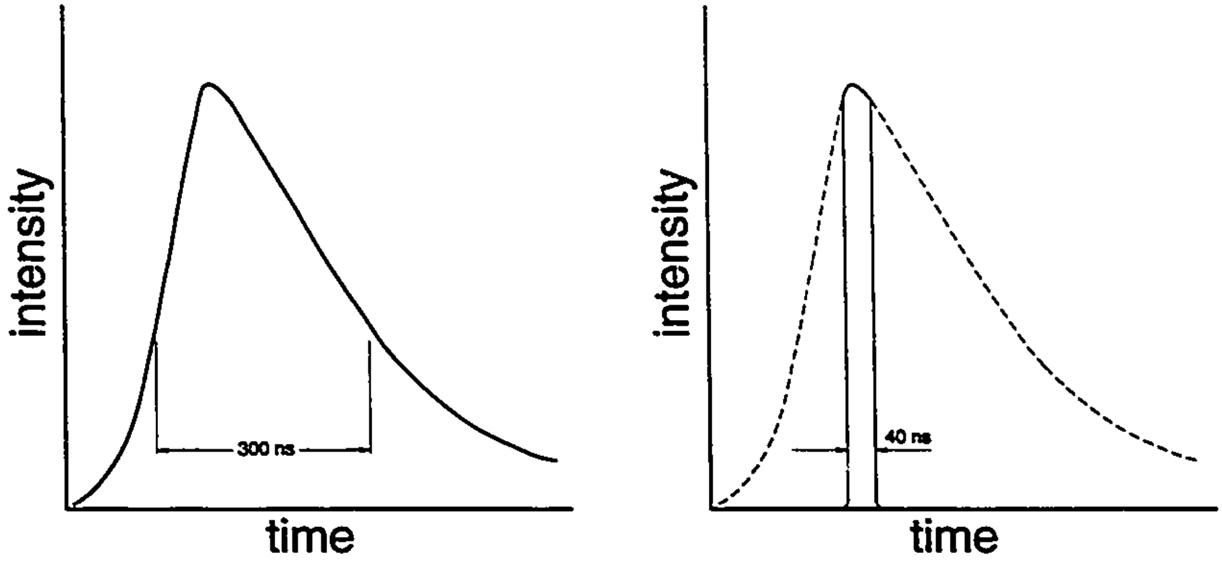

Figure 13. Typical laser intensity as a function of time for both the full pulse duration and for a beam shortened by the Pockels cell pulse slicers.

simplicity, to meet the goal of producing two-colour PIV imagery under the conditions of most flow fields, including combustion.

4.1.2 Sheet Formation Optics

To produce a PIV image, the laser beam crossing the flow field is formed into a sheet that should ideally be collimated, of constant thickness, and have a uniform intensity distribution throughout its entire volume, so that regardless of where a particle is located within the volume traversed by the sheet, it will scatter the same amount of radiation. A typical laser sheet is more likely to be nearly collimated, with the thickness converging to a minimum at the beam waist and then diverging again, and with the intensity varying in a Gaussian manner along the height and

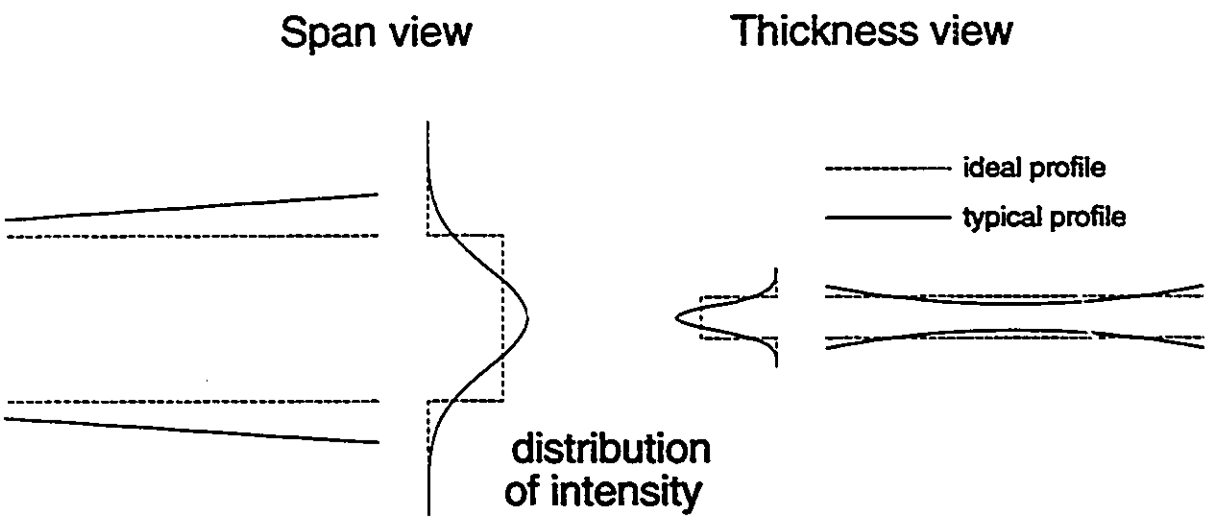

Figure 14. Laser sheet profiles, illustrating nonuniformities in intensity and sheet dimensions.

the thickness of the sheet (Figure 14).

The flashlamp pumped dye lasers have a relatively uniform intensity profile over the beam cross-section, which is an advantage over most lasers which have a Gaussian profile. This results in the variation in intensity over the span of the sheet being minimized, although the intensity still peaks at the centre and tapers away towards the edges.

The span of the laser sheet is determined primarily by the size of the region-of-interest to be measured, which is usually determined by the scale of the experiment itself. Another consideration which may limit the span and/or the width of the sheet is the required energy density (per unit area) to achieve sufficient scattering from the particles. For spans of less than 100 mm the beam may be collimated by using a negative lens to expand and a positive lens to recollimate. Since positive lenses with an aperture greater than 100 mm are uncommon, for spans of greater than 100 mm a second lens might not be used, allowing the beam to continue to expand. Another solution for large spans is to place a positive lens near enough to the negative lens to partially recollimate the beam while permitting the sheet to pass through the aperture uncropped.

Several factors affect the desired thickness of the laser sheet. Although PIV is a two-dimensional measuring technique, most flow-fields tend to be three-dimensional, so that there is an out-of-plane component to the velocity. The velocity measured with PIV is a projection of the true velocity onto the plane defined by the span of the laser sheet and its direction of propagation. However, to measure a velocity, the particle must remain within the laser sheet volume for both pulses. Thus the sheet must be thick enough to meet this condition. However, the sheet must be thinner than the depth-of-field of the camera system, or else the particles at the edges of the sheet will form out-of-focus images. Also, if the sheet is not thin, the number of particles illuminated may become too great to analyze, and/or the scattering from these particles may become so intense that secondary scattering from particles outside of the laser sheet occurs, obscuring the image. Other factors are the size of the region-of-interest, the size of the particles, and the anticipated velocities. Typical sheet thicknesses for PIV are 100 μm to 2 mm.

Since the sheet thickness is less than the beam diameter of the dye lasers (10-25 mm), a positive lens will have to be used to focus the laser beam in this plane. As a result, the sheet width will vary across the region-of-interest with the minimum (beam waist) centred in the region-of-interest. As a guideline, the focal length of the lens should be selected so that the sheet thickness at the edge of the region-of-interest is no greater than twice the beam waist. The sheet thickness can be estimated as

$$\Delta x_{edge} = f\theta_d + \frac{w\,d_l}{2f} \tag{20}$$

which is the sum of the diffraction-limited beam waist and the growth in the waist estimated by simple geometric optics. Δx_{edge} is the sheet thickness at the edge of the region-of-interest, f is the focal length of the lens, θ_d is the laser beam divergence, d_l is the diameter of the laser beam at the lens, and w is the width of the region-of-interest.

Due to the high divergence angle of these lasers (3 milliradians), creating thin sheets (<0.5 mm) is difficult. If a substantial loss in energy is acceptable, this can be done by focusing the beam onto slits in order to reduce the divergence by geometrical filtering. The beam passing the slits is then refocused to create the sheet.

4.1.3 Film Digitizer

In order to perform a quantitative analysis, the PIV images are required to be in a digital form. There are two distinct methods for achieving this: recording electronically with a CCD or similar type camera and then digitizing the analog signal; or recording on film and then scanning and digitizing the image on film. The primary consideration for determining the

Table VII Image recording choices

Recording Format	Advantages	Disadvantages
Electronic Camera (CCD)	Immediate Results	Low to medium resolution Need two cameras
35mm Film or 120 Format Roll Film	High resolution Results in one hour Easy to use Many lenses and accessories	Compromise on both resolution and time to view results
4" x 5" Format Sheet Film	Extremely high resolution	Cumbersome Processing takes days Difficult to digitize

recording method is the number of resolution elements in the image. Other influencing factors are cost, ease of use, and the time interval before the image may be viewed. The key features of the recording formats are summarized in Table VII.

Electronic cameras provide instant results, which allows one to form an immediate decision as to the success or failure of the experiment in terms of focus, exposure, and observation of phenomena. A typical resolution for commercial models is 384 x 576 pixels, which is far too low for PIV. These models also tend to provide a colour composite image, which is also interlaced. The composite image would be difficult to separate into the red, green, and blue (RGB) components without introducing noise. The interlacing degrades the single frame image resolution further by a factor of two. Scientific CCD cameras do provide medium-to-high resolutions, from 1024 x 1024 pixels up to 2048 x 2048 pixels, and there is no interlacing of the output. However, these are monochromatic cameras, and as they require more than one second to scan the array, two cameras would be necessary to acquire two-colour PIV images in the submillisecond time interval between laser pulses. This is unacceptable, as errors in aligning the images from two sources will increase the experimental error in the PIV technique, and the cost of two scientific grade CCD cameras would be prohibitive.

To achieve maximum resolution, film is the best choice. High sharpness, fine grain colour films offer resolving powers of 100 lines/mm at high contrast. Thus with 4" x 5" format sheet film one could obtain images with 10,000 x 12,500 pixels, or even 5,700 x 5,700 pixel images with 120 roll film. 35mm film offers 2,400 x 3,600 pixel resolution, which is considerably greater than that available from electronic cameras, although not as high as that offered by the larger format films. Thus, for the same film resolution, the 4" x 5" format offers a larger field-of-view than 35mm film. However, the 4" x 5" format sheet film was rejected due to the operational difficulties in using it, including cumbersome and time-consuming loading and unloading for each frame, cost of processing, and the several day turnaround time to see the results. The 35mm and 120 roll films both are easy to use in modern cameras and can be processed in one hour at a consumer film laboratory. Cameras in the 35mm format have available a greater selection of high quality lenses and accessories, but this is not a significant advantage. Due to the smaller format, the full-frame shutter speeds for 35mm format cameras are significantly faster than those for 120 format cameras, reducing the potential interference from background illumination or soot radiation.

Once the film is processed, the image must be digitized. The methods for this are listed in Table VIII. Flatbed scanners require direct contact with the image, so that there is a 1:1 relationship between the pixel size of the image and that of the scanner. At best, scanners offer 600 dots per inch (dpi), equivalent to 24 lines/mm, which is far lower than the film resolution, and makes flatbed scanners unsuitable. Post[3] has used a scientific CCD camera at this point in the analysis, employing an enlarger to project the image onto the CCD in order to maintain the resolution of the film. This method requires using an X-Y table to move the camera, as only a portion of the film is imaged at one time. This method may introduce error due to misalignment

Table VIII Digitizing methods

Method of Digitizing	Advantages	Disadvantages
Flatbed scanner	Can digitize any film format	Lower resolution than film
Imaging onto a CCD	Can digitize any film format Can maintain film resolution	Cumbersome method
35mm film/slide scanner	Can maintain film resolution Easy to use Automatically performs RGB colour separations	35mm format only

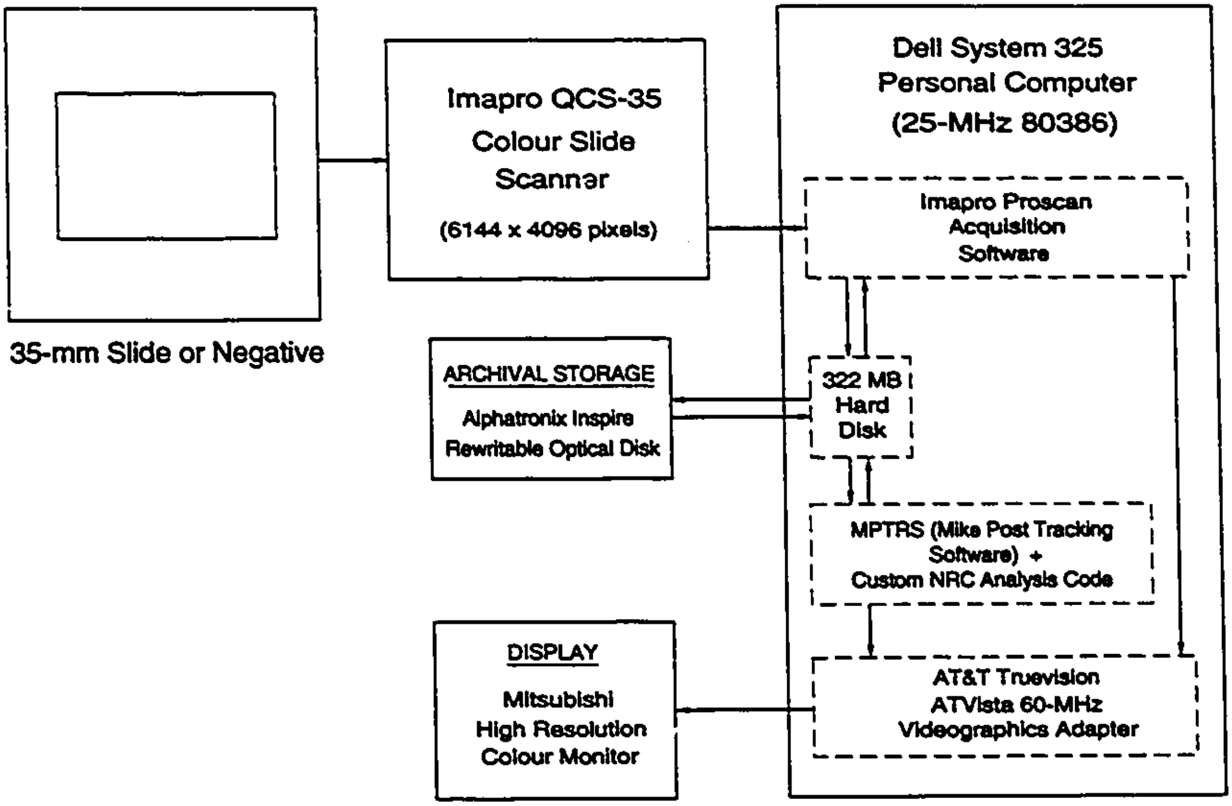

Figure 15. Schematic diagram of digital image processing workstation.

between image subsections. Also, the scan must be performed twice, once for each colour, with appropriate colour filters inserted between the film and CCD to separate the images. Thus, this technique is cumbersome, time-consuming, and potentially error-prone.

The method chosen for the two-colour PIV system is the 35mm film/slide scanner. The model selected for this project is the Imapro QCS-35 Colour Scanner, which is a fully automatic self-contained desktop unit that is operated from a personal computer. Either a Macintosh or an IBM AT compatible PC can be used as the controller. The latter, a Dell System 325 (25 MHz Intel 80386 processor) was chosen to operate the scanner. A Truevision ATVista videographics adapter was installed to display the images at resolutions up to 1024 x 768 pixels on a 20" monitor. The scanner is controlled by Proscan version 4.0 software from Imapro, which allows the user to calibrate the scanner, set the scan resolution, select the file type, determine the region of the frame to be scanned, and perform the scan itself. Figure 15 illustrates this setup. The scanner has a resolution of 166 pixels/mm, which is equivalent to 4096 x 6144 pixels for a 24 x 36 mm image from 35mm format film. This is greater than the resolution of most colour films, so that image quality is not degraded by the scanner. The red, green, and blue components for each pixel are digitized at 8 bits, providing 256 intensity levels for each colour. These values are stored independently in the TARGA file format on the host computer. Thus the scanner performs the colour separations of the blue and green images automatically.

The scanner includes a self-calibration procedure that performs a shading correction for both nonuniform source illumination and nonuniform gain response from pixel to pixel. There is a dark correction performed at 12 bit accuracy to eliminate baseline offset due to background noise, and a base density control to adjust for the fog level of the film in each of the three primary layers. Finally, a prescan of the image is performed to determine the minimum and maximum intensities, so that the actual range of intensities found in the image is divided into 256 levels. All these internal operations are performed at greater than 8 bits, and even the A/D converter operates at 9 bits, so that the 8 bit output is truly noise-free.

In summary, the Imapro QCS-35 Colour Scanner is extremely easy to use, maintains the full resolution of the film, separates the two colour images, and introduces no noise to the data.

4.1.4 Film Selection

Film attributes that are significant in obtaining images for two-colour PIV analysis are resolution, dynamic range, and colour separation. High resolution is required to observe small particles, to allow as large as possible a region-of-interest to be imaged, and to measure the particle locations (and thus the velocity vectors) with high precision. Increasing the difference between the minimum intensity necessary to exceed the gross fog level of the film and the maximum intensity possible without exceeding the maximum density (see Figure 16), which increases the dynamic range, is useful for two reasons. First, it extends the range of particle sizes which can be imaged, since the scattering intensity is a function of the particle diameter. Second, it increases the likelihood of a particle being imaged regardless of location, in spite of nonuniformities in the distribution of intensity through the span and thickness of the laser sheet which affect the scattered intensity.

Colour separation on film can be avoided by splitting the two scattered wavelengths with a dichroic mirror and imaging onto two cameras, each with black-and-white film. Although black-and-white films are available with higher resolution and dynamic range than the best colour films, this method is not suitable because the images are not recorded on the same frame. Using separate cameras for the two images would make it difficult to accurately determine the absolute coordinates for both images, which is essential for the PIV technique. Also, there is the possibility of variance in the lens imaging, such as slightly different magnifications or object focal planes. The use of colour film ensures that the two images have identical location registration and that both scattered

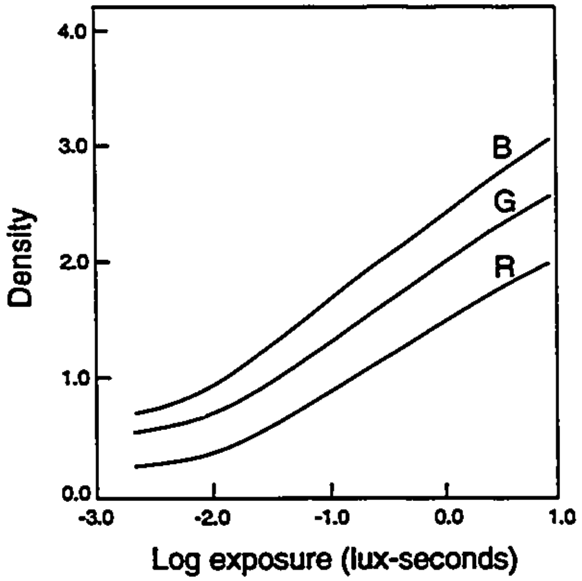

Figure 16. Characteristic curves for Kodak Gold 100 colour film.

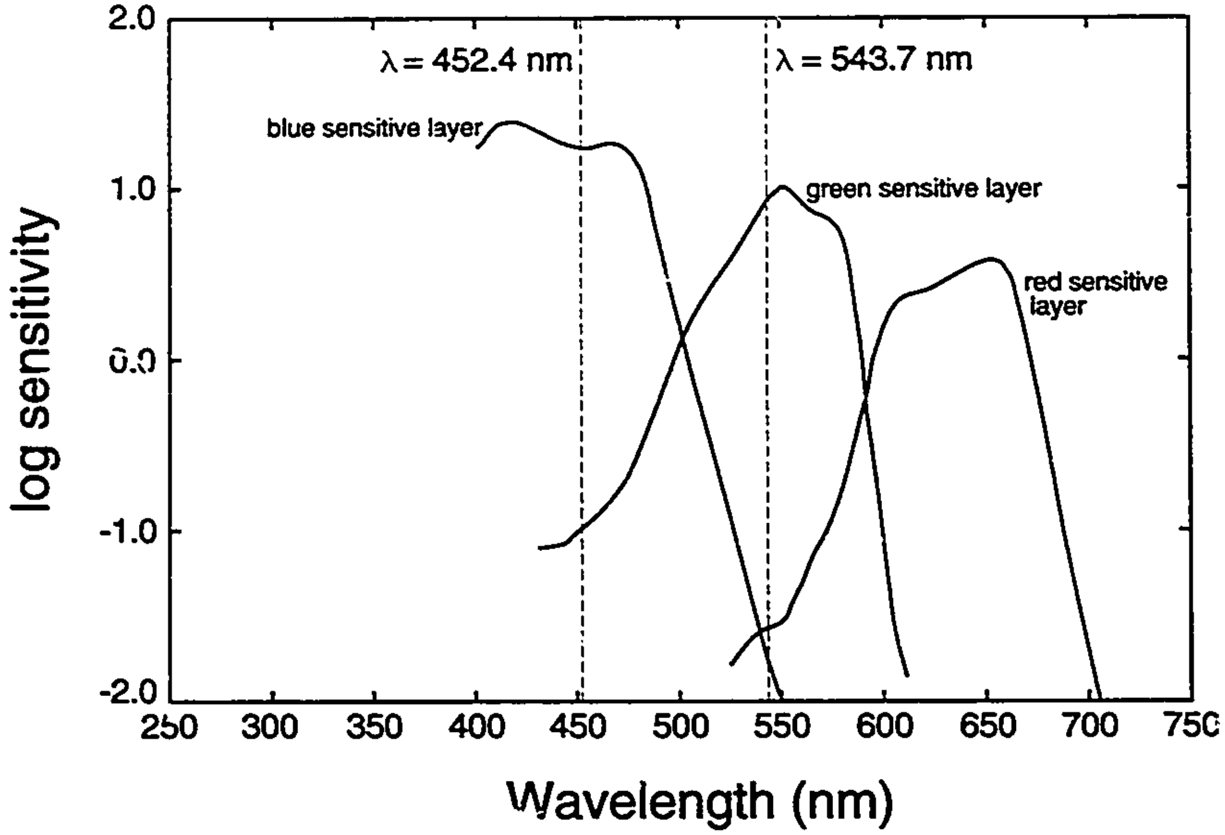

Figure 17. Spectral sensitivity curves for Kodak Gold 100 colour film (with laser wavelengths indicated by dashed lines).

wavelengths have the same lens imaging characteristics (assuming that the lens is achromatic).

To achieve colour separation on film, the scattered wavelengths must be exposed in different layers of the film. The spectral sensitivity curves (Figure 17) show that there are three primary layers in colour film, corresponding to the colours blue, green, and red. The film scanner used to digitize the photographs has a combination of lamp and filters with similar transmission characteristics (Figure 18). Since blue-green wavelengths are desirable to avoid combustion radiation, the two laser wavelengths should be in the ranges 400-460 mm and 520-570 nm, to avoid colour cross-sensitivity in the scanning process. Colour cross-sensitivity is defined here as the response by two different filters to the same wavelength, and this occurs from

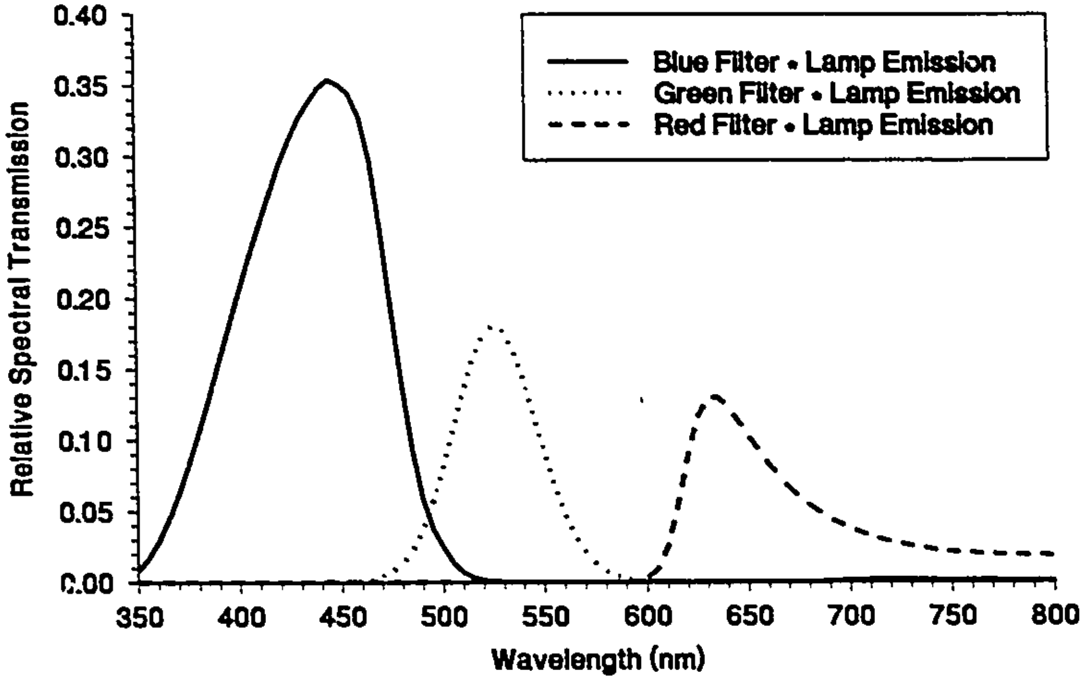

Figure 18. Transmission characteristics for colour filters in Imapro QCS-35 Slide Scanner multiplied by the relative spectral emission of the projection lamp.

460 nm to 520 nm for the film scanner. On film, colour cross-sensitivity is defined as two or more layers responding to the same wavelength. From the spectral sensitivity curves (Figure 17), it can be observed that this occurs to some degree at almost all wavelengths. In this regard, at the laser wavelengths, the film should have a maximum difference in sensitivity between the intended recording layer and the other layers. For colour films, this difference is typically greatest at approximately 450 nm for the blue layer and 550 nm for the green layer, with respect to each other. Response in the red layer is not a factor in consideration of the analysis of the images.

Selection of an appropriate film thus requires finding the best compromise between high resolution, high dynamic range, and maximum difference in sensitivity at the laser wavelengths. Two good choices are Kodak Ektar 125 and Kodak Gold 100. The Ektar 125 provides the maximum resolution available in 35 mm colour film but suffers from colour cross-sensitivity. The Gold 100 is a good compromise, offering less resolution but increased immunity to colour cross-sensitivity. Data for both films are presented in Table IV for wavelengths of 452.4 nm and 543.7 nm. These are the wavelengths closest to the conditions specified above for optimum performance of the colour film and the scanner that were obtainable with the dye lasers.

4.1.5 Seed Particles

Large particles with a low seeding density are preferred for two-colour PIV owing to the fact that the analysis method is intended to track individual particles. Conventional monochromatic PIV analysis, whether using the Young's fringe method or spatial autocorrelation, can accommodate high seed densities since only a global average is calculated at each analysis location, and not velocities of individual particles. Large particles are desirable because they have a higher scattering cross-section, resulting in more exposure for a given laser energy. It is far easier to attenuate excess scattered light than it is to generate more laser energy if there is insufficient scattering.

Excess scattering from particles within the laser sheet (defined as primary scatterers), due to high seed densities or to large particles, may cause unwanted scattering from particles outside the laser sheet (defined as secondary scatterers). This secondary scattering could cause obscuration, increased background noise, and incorrect particle matching. When the area of particle images exceeds 30% of the frame area on the film, the analysis software becomes unreliable. Therefore the maximum seed density recommended is

$$N_{\max} = \frac{Q_{i_{\max}} M^2}{A_e \Delta x} = \frac{0.3\, M^2}{\frac{\pi}{4} d_e^2 \Delta x} \tag{21}$$

where N is the number density of seed particles, Q_i is the degree of coverage in the image plane, M is the magnification of the camera, A_e is the cross-sectional area of an average sized image,

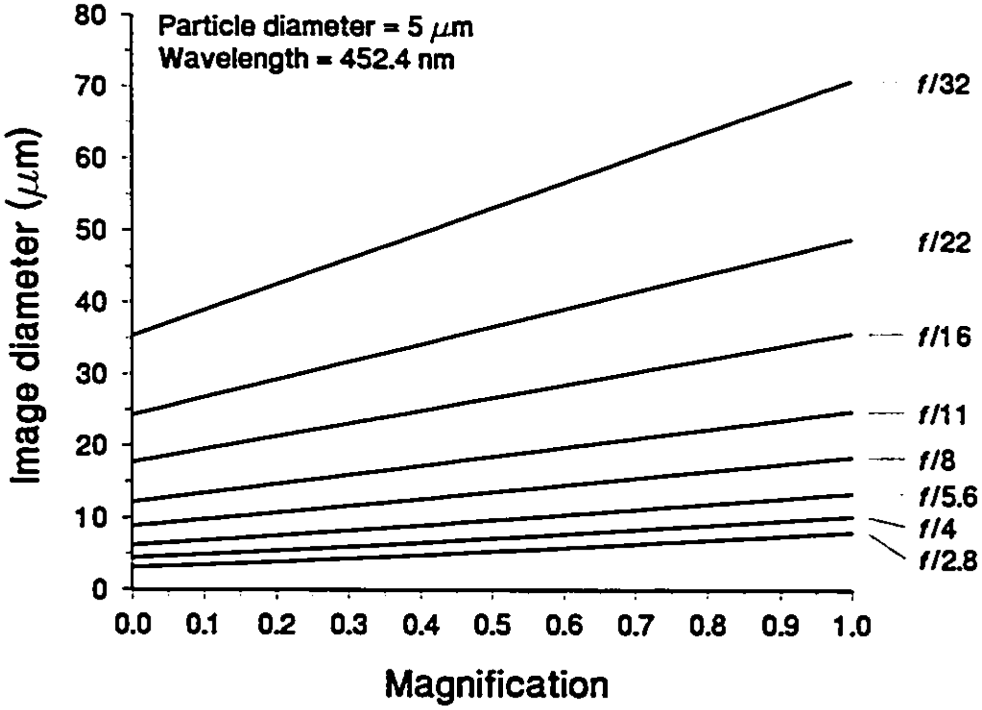

Figure 19. Image diameter for a 5 μm particle, calculated as a function of magnification and aperture for a diffraction-limited lens.

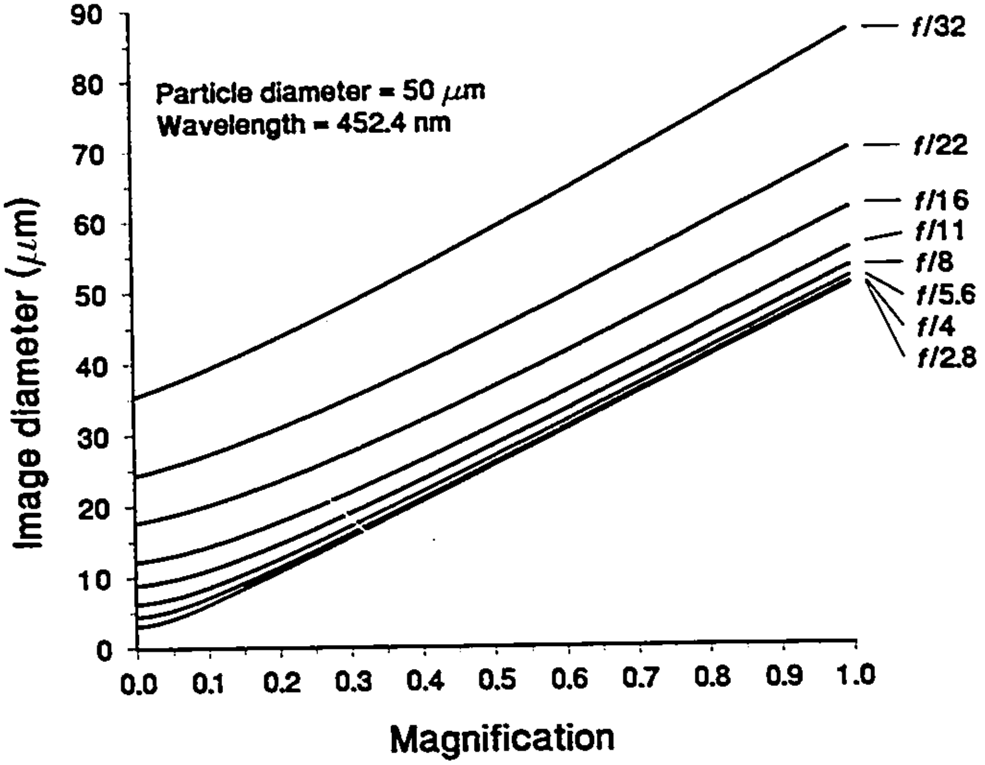

Figure 20. Image diameter for a 50 μm particle, calculated as a function of magnification and aperture for a diffraction-limited lens.

d_e is the particle image diameter, and Δx is the sheet thickness. From Section 3.2, the image size is determined by the particle size and the lens magnification and *f*-number. For small particles, the image diameter is usually much larger than the particle diameter (Figure 19), increasing the maximum velocity permitted by the motion blurring criterion (Equation (19)) for a given laser pulse duration (Figure 21). Figure 20 shows the results of image size calculations for a 50 μm particle, which represents a typical droplet diameter.

The objective of particle seeding is to measure the fluid velocity, so it is important that the seed particles follow the flow as closely as possible, with minimal slip velocity between the

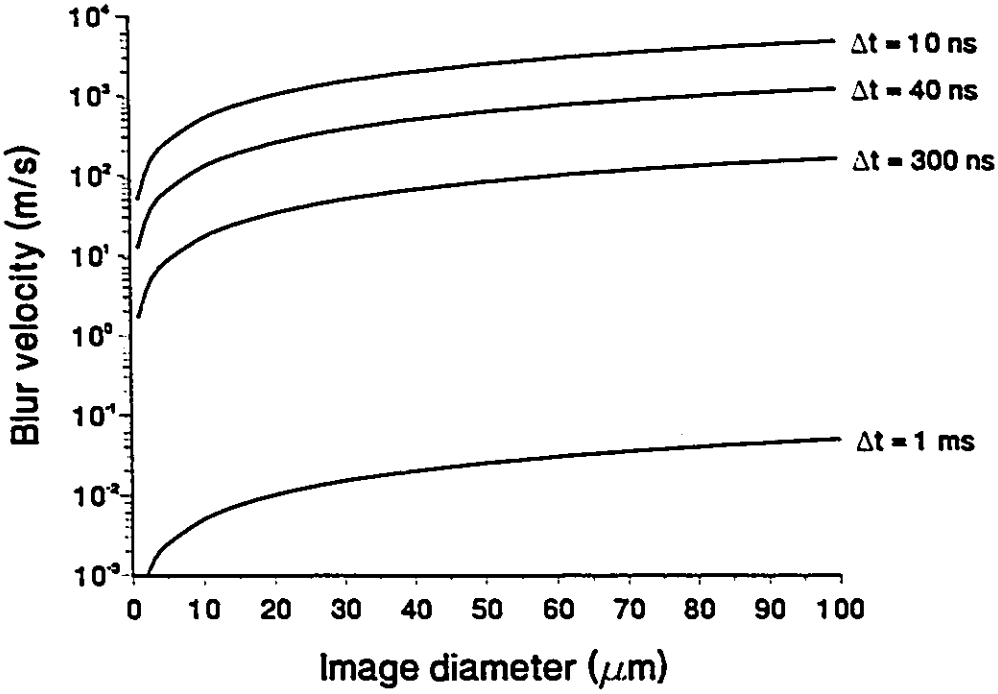

Figure 21. Maximum velocity permitted under the acceptable blurring criterion for various laser pulse durations and image sizes.

particle and the fluid. This can be achieved by minimizing the response time of the particles, τ_p, which can be determined from[64]

$$\tau_p = \frac{\rho_p \, d_p^2}{18 \, \mu} \tag{22}$$

where ρ_p and d_p are the particle density and diameter, respectively, and μ is the fluid dynamic viscosity. The slip velocity is minimized by reducing the particle diameter and density. To minimize the density for a given particle diameter and material, hollow spheres or microballoons are better than solid particles. These are characterized by their effective aerodynamic diameter, d_{aero}, which is defined as

$$d_{aero} = \left(\frac{\rho_h}{\rho_s} \right)^{\frac{1}{2}} d_p \tag{23}$$

where ρ_h and ρ_s are the densities of hollow and solid spheres of the same material.

A good compromise between the requirement for large, easily imaged particles and small, well-entrained particles is the hollow alumina microsphere (Table IX). These particles have a mean diameter of 6 μm, yet the effective aerodynamic diameter is approximately 3 μm, so that particle visibility is maximized while aerodynamic response is maintained. These particles have an estimated response time of 110 μs at room temperature and 33 μs at a combustion temperature

Table IX Seed material specifications (data provided by suppliers)

Seed Material		Specific Gravity	Refractive Index	Typical Size (μm)	Melt Temperature
Alumina	Al_2O_3	3.97	1.765	0.05 ~ 2.0	2300 K
Hollow alumina microspheres	Al_2O_3	1.0	1.765	6	2300 K
Glass microballoons	SiO_2	0.30	1.5	13	1200 K
Phenolic microballoons		0.25	N/A	43	N/A
Sodium chloride	NaCl	2.16	1.54		1074 K
Titanium dioxide	TiO_2	4.17	2.6	0.2	2100 K
Zirconium oxide	ZrO_2	5.89	2.20	1.5	3000 K

of 1900 K. The hollow alumina microsphere can be used for combusting environments, as alumina will withstand the high temperatures found in the reaction zone. For noncombusting flows, phenolic or glass microballoons are less expensive materials, although the large sizes are not suitable for flows with high turbulence intensities.

In liquid spray-fuelled combustion, the fuel droplets themselves may be used as the tracking particles. This is most useful if the intention is to measure droplet velocities or trajectories. However, droplets are less desirable for measuring the velocity of the gas phase flow due to their high slip velocities. Fuel sprays typically have a wide size distribution, which makes imaging a greater challenge than with solid particles, which can be sorted by size prior to seeding. Also, the spatial distribution of droplets is often uneven, resulting in regions where the number density of droplets is too great to allow particle pairs to be matched or even to identify individual droplets. It is difficult to obtain correct exposure due to the wide size distribution. However, it should be possible to determine an exposure level at which most droplet diameters can be imaged.

4.2 EXPERIMENTAL APPARATUS

The optical arrangement of the two-colour double-pulse PIV apparatus is shown in Figure 22. The lasers used to form the light sheets are Candela SLL-250 flashlamp-pumped dye lasers. These have an output beam diameter of 10 mm, with a top-hat (spatially uniform) energy distribution profile. The pulse duration is 300 ns FWHM (full width of half maximum), and the maximum repetition rate is 0.5 Hz. The maximum output energy is up to 1.0 J, depending upon the dye and solvent used. For the dyes used, the actual maximum energy available for each

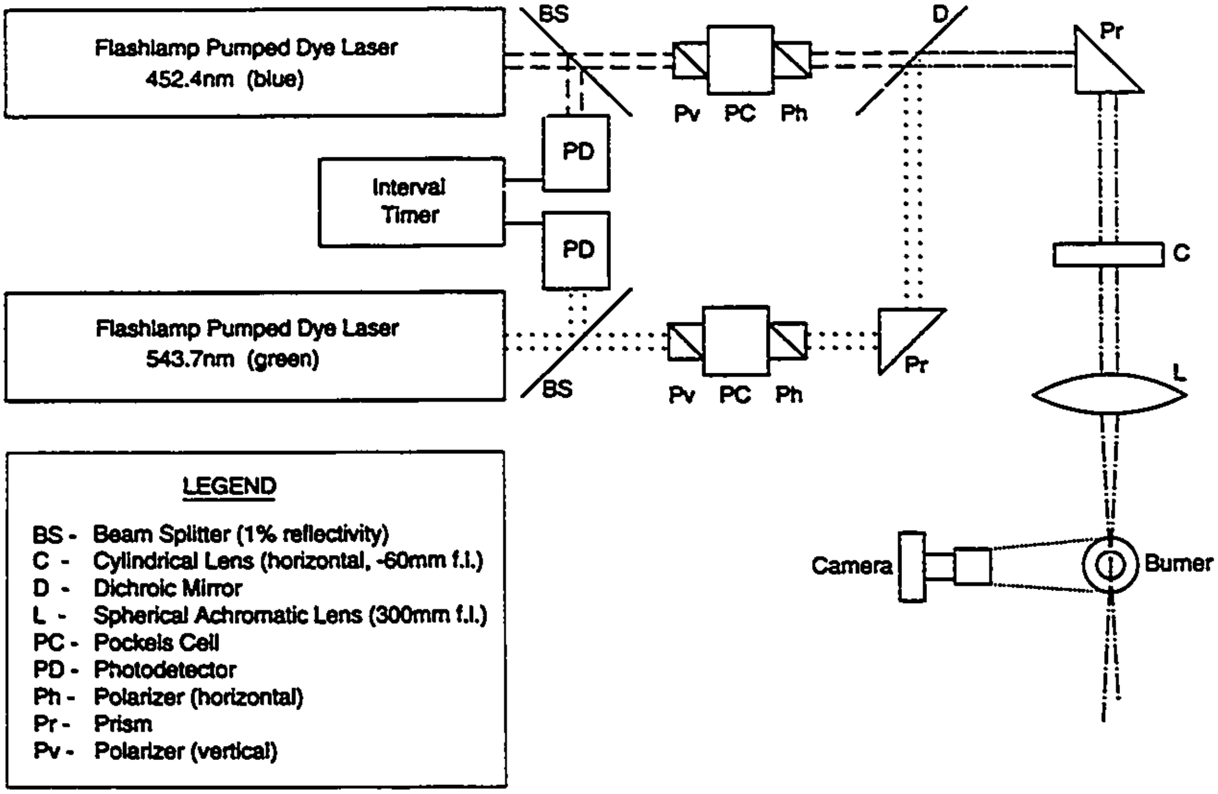

Figure 22. Top-view schematic showing optical layout of the two-colour double-pulse PIV apparatus.

colour is approximately 500 mJ. Pure methanol is used as the solvent because it prolongs the dye lifetime and improves the spatial uniformity of the output beam. To minimize the effects of combustion radiation, blue-green wavelengths are desirable, and from colour film restraints, 450 nm and 550 nm are the best choices. Coumarin 450 was selected as the blue dye, and Rhodamine 560 Chloride mixed with LD490 was selected as the green dye. The blue dye lases at 452.4 nm with a bandwidth of 4.7 nm FWHM (Figure 23), and the green at 543.7 nm with a bandwidth of 1.6 nm FWHM (Figure 24).[76]

To determine the time separation between the pulses from the two lasers, 1% of each beam is steered onto photodetectors which are the inputs to an interval timer. Following this,

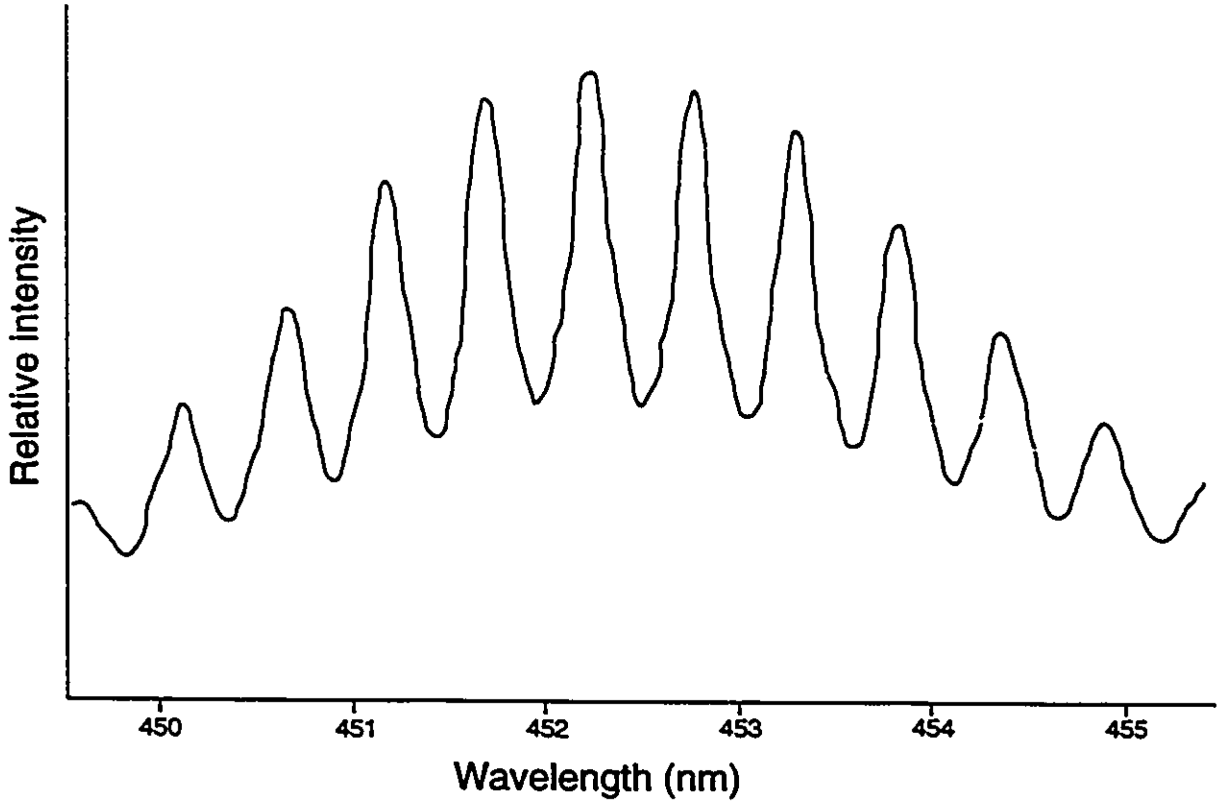

Figure 23. Blue laser spectral profile.

each beam passes through a Pockels cell to reduce the pulse duration, if required. The two beams are then combined by a dichroic mirror, and are formed into coincident laser sheets. A -60 mm focal length cylindrical lens expands the beam on its vertical axis. Spaced 240 mm away, so that its object is at the same location as the virtual object of the cylindrical lens, is a 300 mm focal length spherical lens (75 mm diameter). This recollimates the beam in the vertical plane at a span of 50 mm, and focuses the sheet in the horizontal plane 300 mm from the lens, where the test section is located. The angular divergence of the laser beam is 3 milliradians, so from

$$\Delta x_{\min} = f\,\theta_d \tag{24}$$

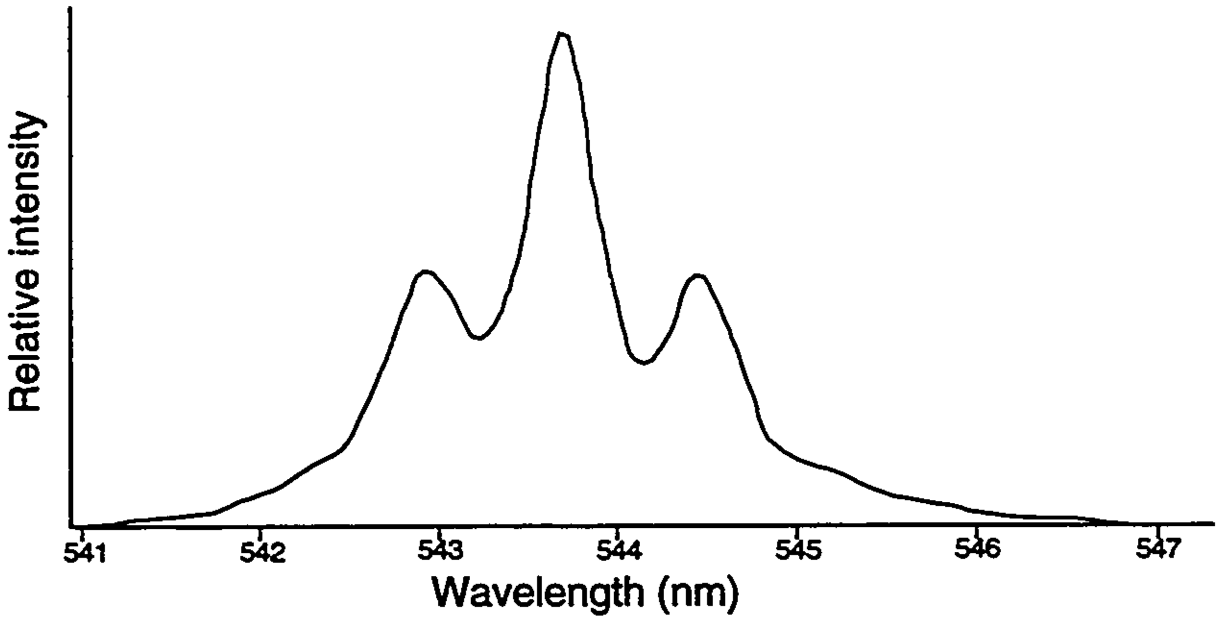

Figure 24. Green laser spectral profile.

where Δx is the sheet width, f is focal length of the lens, and θ_d is the beam divergence, the beam waist (minimum sheet thickness) is 0.9 mm.

To discriminate against background radiation, a fast shutter speed is desired. However, 35 mm cameras employ focal-plane shutters, which traverse a narrow slit across the frame to achieve high speeds. At the flash synchronization speed and slower, this slit is the full width of the frame, so that all of the film is exposed simultaneously. Thus, a fast flash synchronization speed is the requirement for this experiment. The Nikon F-801 35 mm SLR camera body was selected for its 1/250 s (4 ms duration) full-frame shutter speed, which is the fastest flash synchronization speed commercially available. The lens used is a Nikon Micro-Nikkor 105 mm focal length *f/2.8* macro lens, selected for its excellent flat-field and close-up imaging characteristics, which provide uniform image quality and allow high magnification.[77] Kodak Ektar 125 film was used to record the two-colour PIV images, and it was processed commercially.

The lasers are powered by a common power supply (Candela HVD-250A) and controlled by a dual trigger generator (Candela DDT-20A). Due to the charging arrangement, the second laser must be fired within 3 ms of the first, or else it will not lase owing to too much energy being drained from its capacitor. This is not considered a limitation, since even for low speed flows the maximum anticipated pulse separation is 1 ms. The minimum separation is 600 ns, which is the full width of the laser pulse. The lasers are synchronized to the camera by using the signal from the camera hot-shoe, which indicates that the shutter is fully open, as the input to the trigger generator.

The digital image processing workstation is shown diagrammatically in Figure 15. The negative film is digitized by the Imapro QCS-35 Colour Slide Scanner, which uses three passes to record the red, green, and blue components of the image. This is accomplished by running Imapro Proscan version 4.0 software on a Dell System 325 personal computer. This is a 25 MHz 80386 based AT-compatible computer. At maximum resolution (6144 x 4096 pixels), a single image file can occupy 92 MB of mass storage. An Alphatronix Inspire drive is used to store the images on rewritable, erasable optical disks. The MPTRS Tracker code, modified for use on the PC platform, is used to analyze the images. This code was made available from Systems Research Laboratories as a VAX-based code.

To test the capabilities of the two-colour PIV apparatus, a small-scale (<5 kW) liquid fuelled burner was developed. A cross-section view of this burner is shown in Figure 25. This is an unconfined axisymmetric bluff-body stabilized diffusion flame design. The bluff-body produces an axisymmetric recirculating flow field. The recirculation provides a complex flow pattern which should demonstrate the advantage of the two-colour PIV method in resolving the directional ambiguity common to monochrome PIV. The axisymmetry is desired to reduce out-of-plane motion by the droplets, so that they will remain in the laser sheet. PIV (conventional or two-colour) would be less successful in swirl-stabilized flow-fields where droplets can move tangentially as well. The fuel is delivered through a Global Thermoelectric piezoelectric atomizer, which produces a full-cone spray. This is the only type of atomizer known to deliver

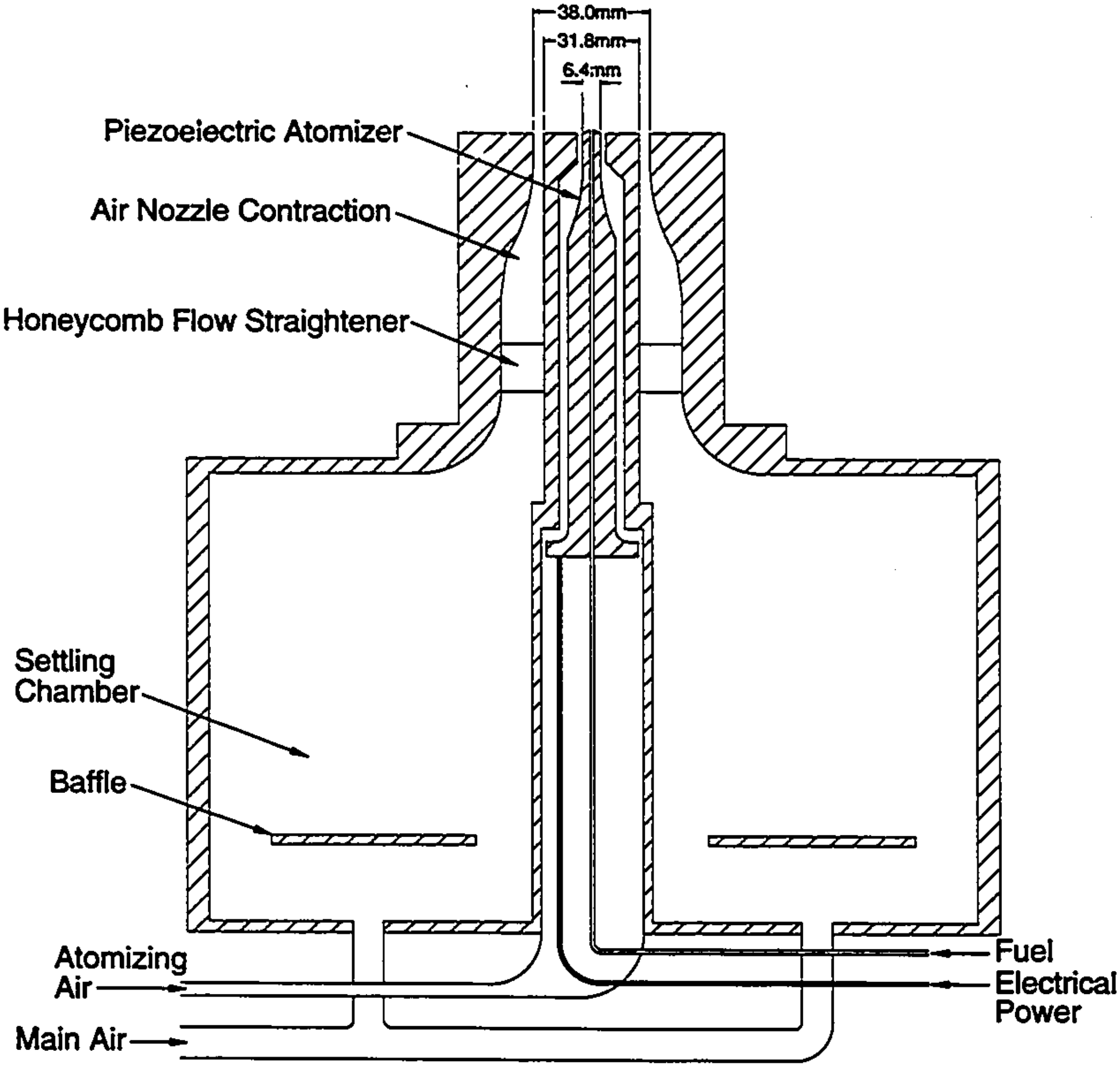

Figure 25. Unconfined bluff-body stabilized liquid fuelled diffusion flame burner.

fuel with the small flow rate desired for this burner. The range of fuel delivery rates is 1 - 6 cm^3/min. The drop size produced by this atomizer, oscillating at 50 kHz, is 40 μm SMD (Sauter Mean Diameter) for diesel No. 2-D (manufacturer's data). This atomizer imparts very little momentum to the fuel droplets. To carry the droplets away from the nozzle tip, atomizing air is forced through the annulus between the nozzle tip and the bluff-body at rate such that the exit velocity is similar to that of the main air flow. The main air flow exits through a 3.1 mm annulus surrounding the 31.8 mm bluff-body and is conditioned to have a uniform exit velocity profile. To accomplish this, the four main air inlets direct the flow onto baffles from which it disperses into a 7.75 L settling chamber, then exits through a bellmouth, passes through a honeycomb flow straightener, and finally goes through a nozzle with a contraction ratio of 10:1 in area.

4.3 PROCEDURE

The burner was operated with n-heptane as the fuel, flowing at 1.95 ml/min. It was positioned with its centreline at the beam waist of the laser sheets. The main air was fed at 100 SLPM (standard litres per minute), measured with a Sierra Instruments mass flow meter. This produced a calculated exit velocity of 5.00 m/s for the main air. The atomizing air, measured with a Matheson 604 Rotameter, was flowing at 2.70 SLPM. The calculated exit velocity of the atomizing air was 2.50 m/s. With a maximum velocity of 5 m/s, there is no need to reduce the 300 ns pulse duration of the lasers to meet the motion blur criterion: for these conditions the criterion requires that the particle image diameter exceed 3.0 μm, which it certainly will. For high velocity flows, the pulse duration can be reduced by the Pockels cell pulse slicers

(Lasermetrics Model 5016C) in each of the beams, as shown in Figure 22. These allow control of the pulse duration from below 40 ns up to 250 ns. For these experiments the pulse slicers were removed.

The lasers were fired at maximum energy, which was measured, using Scientech energy meters, to be 330 mJ for the blue laser and 352 mJ for the green laser. This is less than the 500 mJ peak energy due to dye degradation. The overlap of the two laser sheets was adjusted to within 25 μm of full coincidence by inserting a 256 element Reticon linear photodiode array at the beam waist and adjusting the dichroic mirror until the peak intensities of the two sheets were superimposed. The width of a single diode was 25 μm.

The camera was set up with its image plane 0.45 m from the laser sheet plane. The magnification ratio was 0.41, which is the maximum attainable with the lens used without employing extension tubes. At this magnification, the field-of-view was 86 mm (v) x 57 mm (h). Graph paper (10x10/cm), placed in the plane of the laser sheet and on the burner centreline, was photographed at a shutter speed of 1/15 s at *f/2.8*, so that the spray images could be accurately scaled. The two-colour PIV images were recorded at 1/250 s, at *f*-stops ranging from *f/2.8* to *f/22*. At these lens conditions, the depth-of-field varied from 2 mm (*f/2.8*) to 12 mm (*f/22*). Even at the edges of the field-of-view the laser sheet was only 1.85 mm thick, so that all illuminated droplets were in focus.

To determine the desired separation between laser pulses, one must consider the maximum anticipated distance between corresponding blue and green images of the same droplet. The units of measurement become pixels once the film is digitized. As the number of pixels separating the corresponding images increases, so does the dynamic range and accuracy of the velocity measurement. However, the data processing required increases by the square of this distance, since an area with radius equal to the maximum anticipated distance must be searched. The

Table X LDA test conditions

Condition	Main Air (SLPM - Standard Litres per Minute)			Atomizing air (SLPM)
	Unseeded	Seeded	Total Main Air	
1	30	20	50	1.48
2	188	20	208	3.25*
3	275	20	295	8.87
4	473	20	493	14.79

* should have been 6.15 SLPM to maintain same ratio of centre jet velocity to main air velocity

analysis code limits this maximum distance to 100 pixels. To ensure that all velocities are measured correctly, one should analyze for velocities up to 50% greater than the maximum anticipated velocity. The pulse separation can then be calculated as

$$t_{sep} = \frac{d_{sep}}{1.5\,V_{max}} = \frac{P_{max}}{1.5\,V_{max}\,M\,R_s} \tag{25}$$

where t_{sep} is the time separation between laser pulses, P_{max} is the maximum separation in pixels, V_{max} is the maximum anticipated velocity, M is magnification, and R_s is the scanner resolution in pixels/mm. For the conditions stated above, at the maximum scanner resolution of 166 pixels/mm, the time separation should be set to 196 μs. The measured separation between the blue and green laser pulses was 201.5 μs. Thus, a droplet moving at 5 m/s would move approximately 1 mm between the laser pulses.

To complement the PIV work, the mean air velocities above the burner were measured using a two-component TSI laser Doppler anemometer instrument. These measurements were made in isothermal flow, and fuel was not injected. Table X summarizes the flow conditions.

5 RESULTS

The two-colour method was applied to examine the flowfield in the wake of an unconfined axisymmetric liquid-fuelled bluff-body diffusion flame burner. Initial attempts were made in combusting flow with n-heptane as the fuel. An example of the two-colour photographs obtained is shown in Figure 26. The fuel droplets are evaporated rapidly and are not visible more than a few millimetres away from the nozzle. This is not a good condition to test the capabilities of the two-colour PIV acquisition system. A less volatile fuel, Diesel No. 2-D, was evaluated, but stable combustion could not be maintained.

At this point, three options were considered. The first was to continue trying other fuels until one was found that supported stable combustion, had low volatility so that the droplets might penetrate further, and could be atomized successfully by the piezoelectric atomizer. The second was to continue burning n-heptane and seed the incoming air flow with particles that could withstand combustion, such as the hollow alumina microspheres. The third option was to observe the heptane droplets in a noncombusting regime. The first option was considered time consuming and possibly unsuccessful. The choice between options two and three was whether the presence of soot radiation (with monosized particles) or multi-sized fuel droplets (without flame interference) would pose a greater challenge for two-colour PIV. From inspection of the photograph in Figure 26, it appears that flame radiation does not expose the blue and green sensitive layers of the film, and that it may be eliminated during the scanning process when the image is separated into its red, green, and blue components. Also, a simple cutoff filter to block wavelengths above 550 nm while passing the shorter wavelengths could be attached to the camera

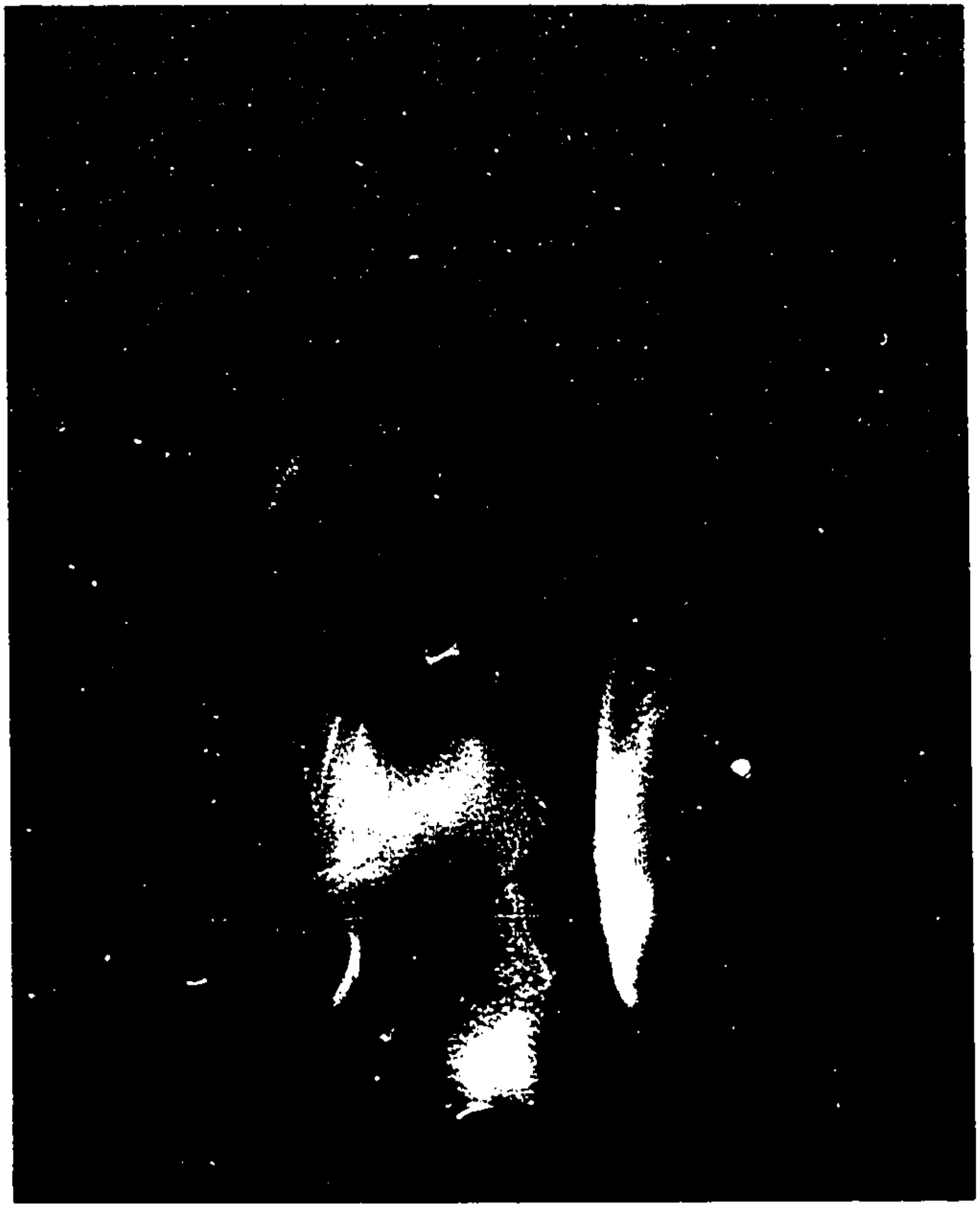

Figure 26. Two-colour PIV photograph of burning heptane spray in the wake of a bluff-body, obtained at *f/11*.

lens to reduce the flame radiation reaching the film. Thus, it was concluded that the presence of a distribution of droplet sizes would be a more difficult test for the system than the presence of flame radiation.

The exposure calculations performed in Section 3.2 were used to determine appropriate conditions for observing the n-heptane droplets. To observe the widest distribution of droplet sizes, conditions were sought such that diameters in the range 1-10 μm would produce good exposures, even though larger droplets would produce overexposures. This was predicted to be acceptable, since the two-colour PIV analysis procedure should be able to manage overexposed images but cannot identify underexposed or nonexistent droplet images.

Following this, experiments were performed with n-heptane in isothermal flow. Photographs were taken at apertures of *f/2.8*, *f/4*, *f/5.6*, *f/8*, *f/11*, *f/16*, and *f/22* (Figure 27 and Figure 28). At *f/22*, the large droplets are exposed correctly, but the small droplets are not imaged since the scattered radiation from them has dropped below the gross fog level of the film. Conversely, at *f/2.8*, the small droplets are visible, but the large droplets have been so grossly overexposed that analysis would be impossible. The best compromise appears in the photographs recorded at *f/11* and *f/16*. The results of the mean exposure theory of Section 3.2 predicted that *f/16* would produce the best exposure for droplets in the range 1-10 μm (Figure 10 and Figure 11), which agrees well with the experimental results. Figure 28(c) was selected for testing the two-colour PIV analysis system, and is shown enlarged in Figure 29. Table XI summarizes the experimental conditions for this photograph.

Examination of Figure 29 reveals that the droplets are carried upwards by the atomizing air to about 25 mm above the burner surface, at which point there appears to be stagnation on the centreline. The centres of some of the blue images of droplets appear cyan, and those of

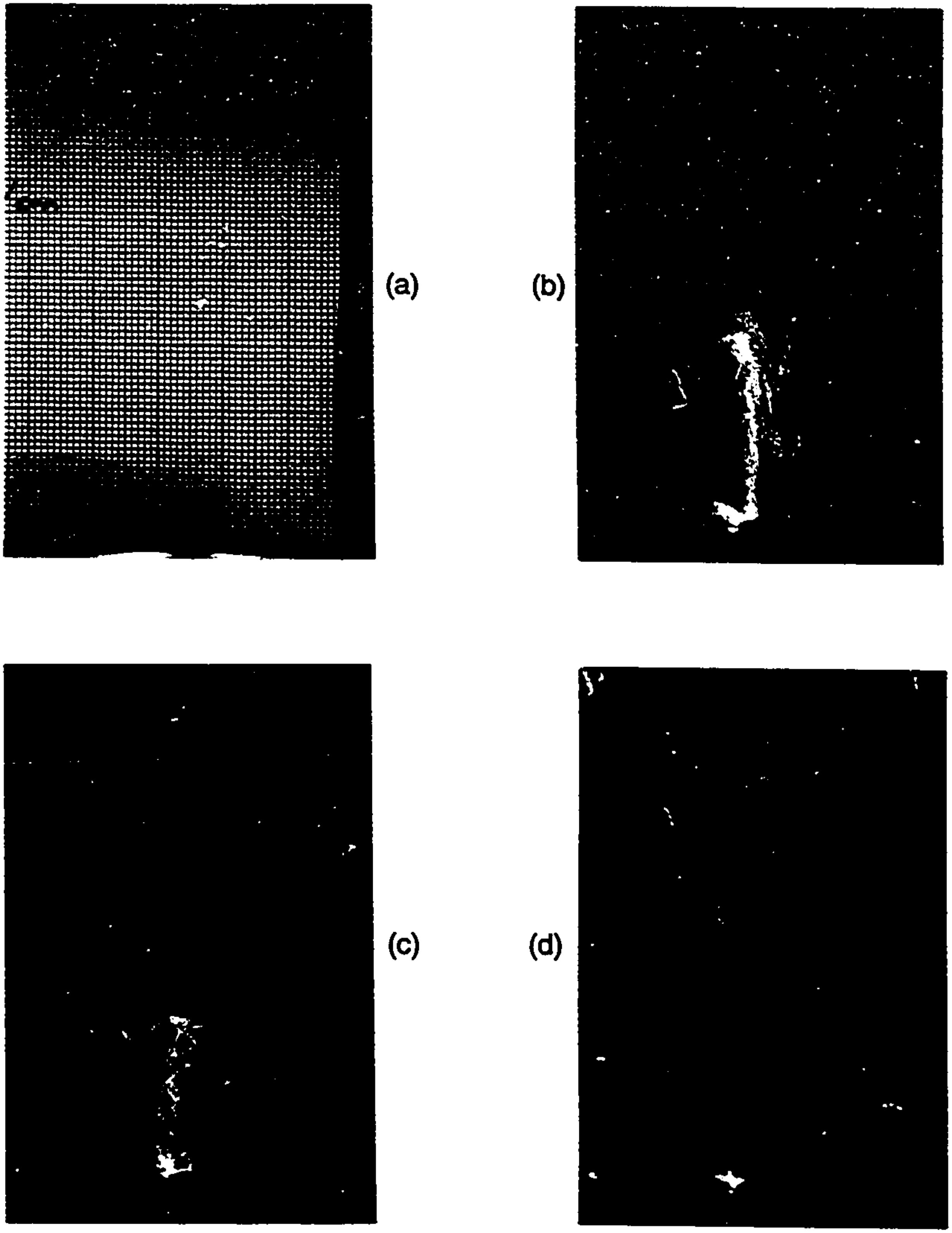

Figure 27. Two-colour photographs of isothermal heptane spray: (a) scale; (b) *f/2.8*; (c) *f/4*; (d) *f/5.6*.

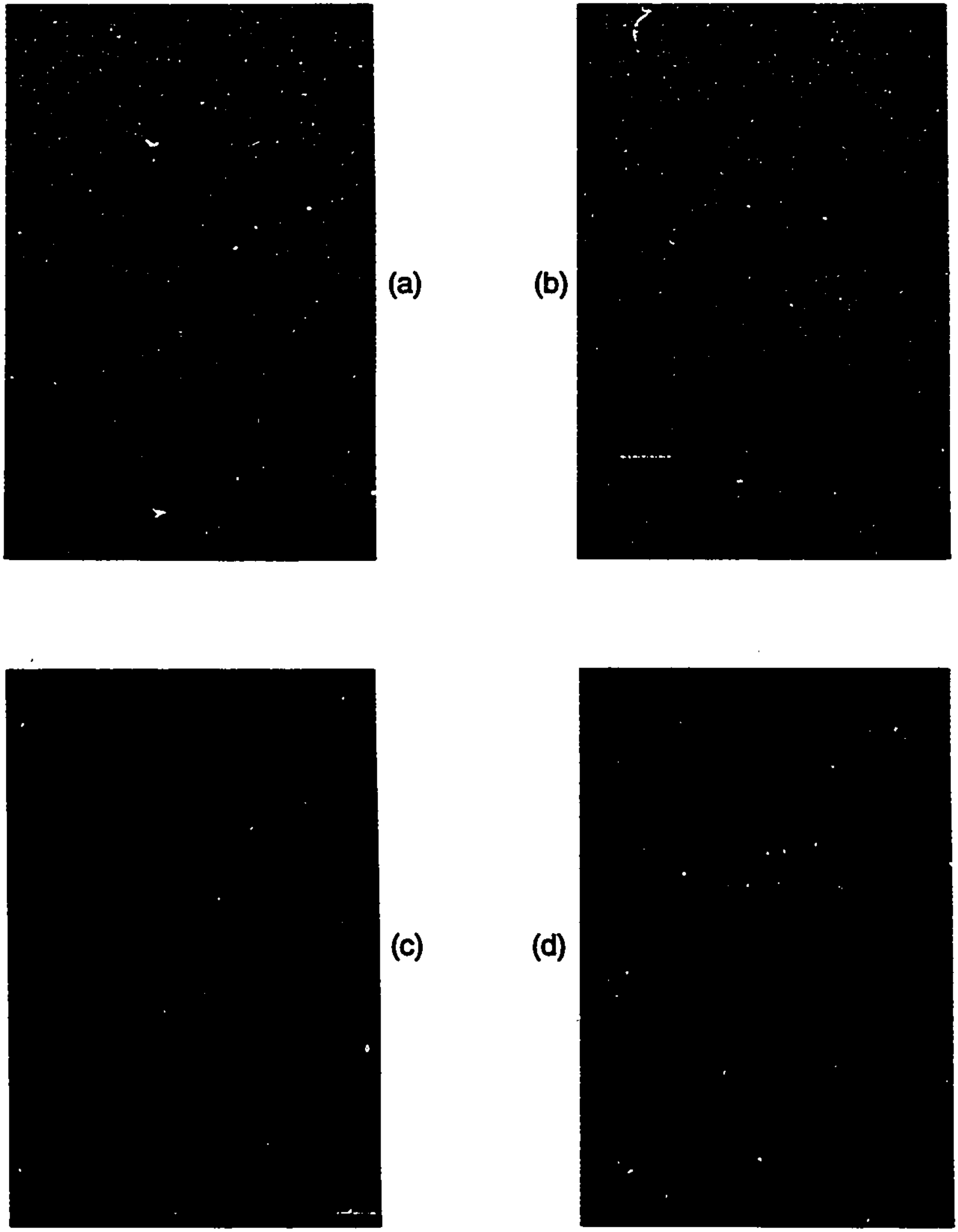

Figure 28. Two-colour photographs of isothermal heptane spray: (a) *f/8*; (b) *f/11*; (c) *f/16*; (d) *f/22*.

Table XI Experimental conditions used to produce photograph selected for evaluating the two-colour PIV analysis system

OPTICAL CONDITIONS

VARIABLE	AVAILABLE RANGE	ACTUAL VALUE
Wavelength / bandwidth	400 nm ~ 700 nm	452.4 nm / 4.7 nm FWHM (blue) 543.7 nm / 1.6 nm FWHM (green)
Pulse energy	<1 mJ ~ 500 mJ	330 mJ (blue) 352 mJ (green)
Pulse duration (FWHM)	300 ns (40 ns ~ 250 ns with Pockels cell)	300 ns
Pulse separation	500 ns ~ 3 ms	201.5 μs
Sheet dimensions	Dependent upon optics	Span = 50 mm Thickness = 0.9 mm at waist; 1.85 mm at edges
Camera		Nikon F-801 35 mm SLR
Lens	*f/2.8 ~ f/32*	105 mm Micro-Nikkor @ *f/16* Focus distance = 0.45 m Depth of field = 8 mm Magnification = 0.41
Shutter speed (full-frame)		1/250 s (4 ms)
Film		Kodak Ektar 125 35 mm size 160 lines/mm @ TOC 1000:1

FLOW CONDITIONS

FLUID	FLOW RATE	ADDITIONAL DATA
Main air	100 SLPM	Velocity = 5.0 m/s at exit
Atomizing Air	2.70 SLPM	Velocity = 2.5 m/s at exit
Fuel (n-heptane)	1.95 mL/min	SMD ≈ 40 μm

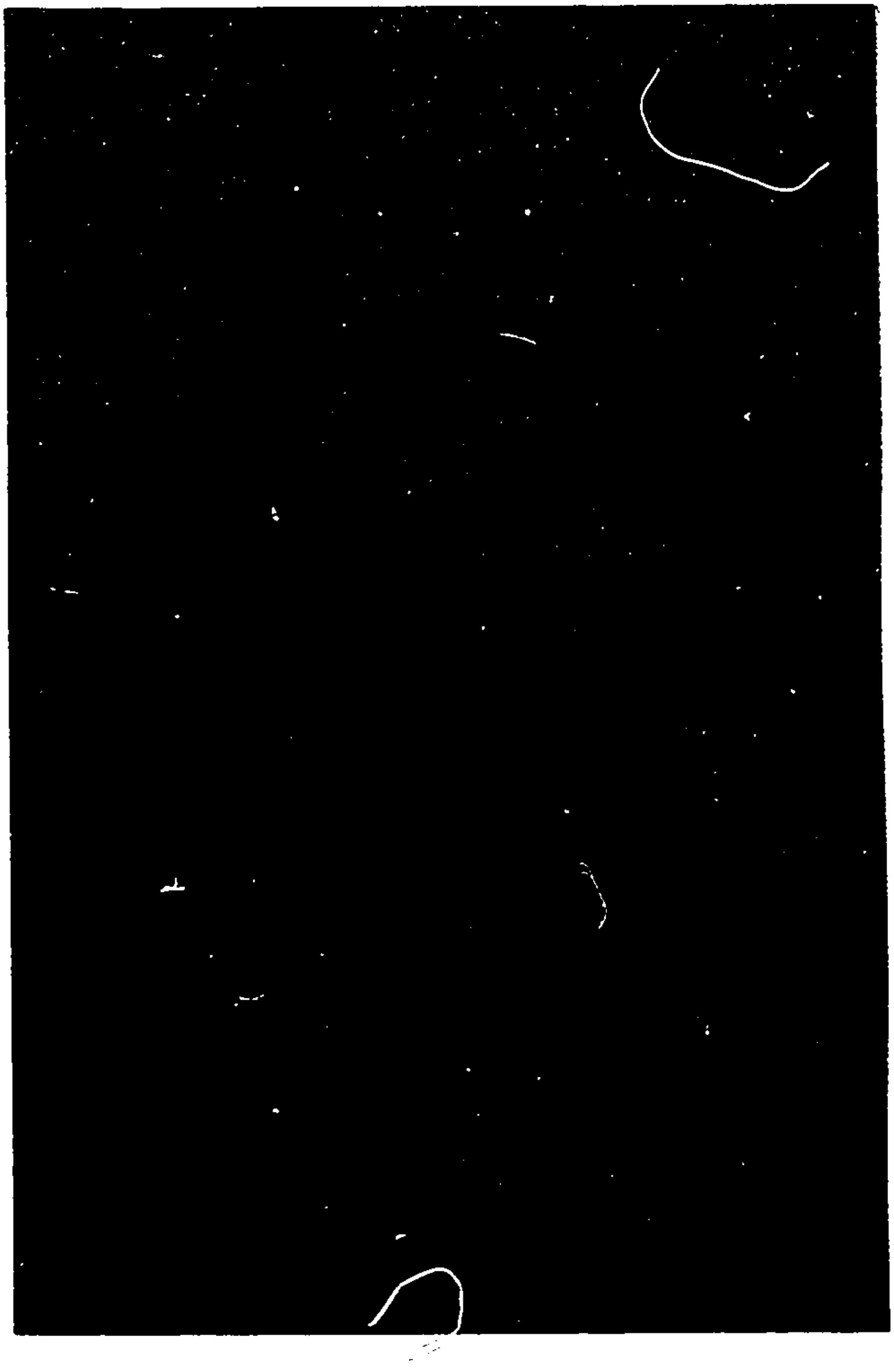

Figure 29. Enlargement of Figure 28(c), isothermal spray recorded at *f/16*, used to evaluate PIV analysis code.

some green images appear yellow, indicating exposure of the green and red layers of film respectively. This overexposure appears to be minimal, but it will result in more green particles being detected than blue. The red particle image centres are inconsequential because the red layer is not analyzed. By setting the minimum droplet velocity to greater than zero, the problem of more green particle images than blue can be minimized since blue and green images superimposed on each other will not be considered for vector matching. Further visual inspection of Figure 29 indicates that the particle images stand out well against the black background, so that the noise level in this image appears to be relatively low. The droplet density in the first 25 mm above the nozzle probably exceeds the allowable source density for PIV analysis, and it is unlikely that vectors (or even individual droplets) will be found in this region.

The scale photographed on the burner centreline is shown in Figure 27(a). The negative was scanned at the maximum resolution of the scanner, 166 pixels/mm, to determine the actual magnification ratio and the velocity represented by each pixel. The magnification can be determined by

$$M = \frac{N_p}{R_s} \tag{26}$$

where M is magnification, N_p is the number of pixels per unit on the scanned scale image, and R_s is the scanning resolution. Analysis of the scanned scale image resulted in a measurement of 678 pixels/cm in the horizontal direction and 683 pixels/cm in the vertical direction, for an average of 680.5 pixels/cm. The actual magnification is therefore 0.410. Nikon quotes a reproduction ratio of 1/2.43 at a focused distance of 0.45 m,[77] which would be a magnification of 0.412 and agrees well with the measured magnification. The velocity represented by each pixel of separation between the blue and green images of the same droplet is determined by

$$V_{pix} = \frac{1}{N_p \, t_{sep}} \tag{27}$$

where V_{pix} is the velocity per pixel and t_{sep} is the time separation between the blue and green laser pulses. For a separation of 201.5 μs and 680.5 pixels/cm, each pixel of separation represents an actual velocity of 0.0729 m/s.

The negative for the photograph in Figure 29 was scanned at maximum resolution to evaluate the PIV analysis code. The image produced by the scan is 3900 pixels in the horizontal (h) direction by 5850 pixels in the vertical (v) direction, creating a file 91,260,018 bytes in size. Due to memory limitations on the computer, the maximum image size that the MPTRS code can process is 1024 (h) x 1024 (v) pixels, and the display adapter has a maximum resolution of 1024

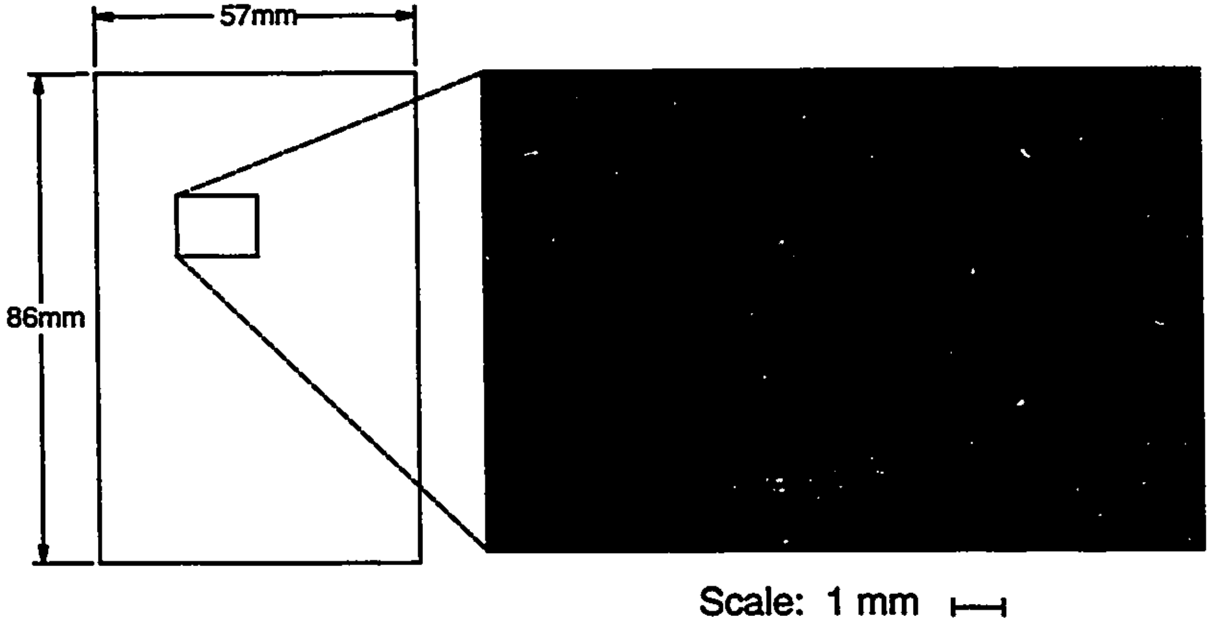

Figure 30. Subsection for analysis, showing region of Figure 29 that it represents.

(h) x 768 (v) pixels. A utility was used to divide the large image into a matrix of 4 (h) x 8 (v) subimages, for a total of 32, which could be processed and displayed. This utility extended the border of each subimage eight pixels into the neighbouring image on all sides, thus creating an overlap region of sixteen pixels for adjacent subimages. Each of these subimages had a size of 991 (h) x 747 (v) pixels. Shown in Figure 30 is subimage {2,6} along with a sketch indicating the region of the original photograph that it occupies.

All of the subimages were then processed following the procedure described in Section 3.3 by applying the MPTRS code. Initially, the subimages were separated into their blue and green components respectively, with the red portion of the image being discarded. The blue and green subimages were then examined to determine the droplet locations. The blue and green droplet locations for subimage {2,6} are shown in Figure 31. The presence of more green

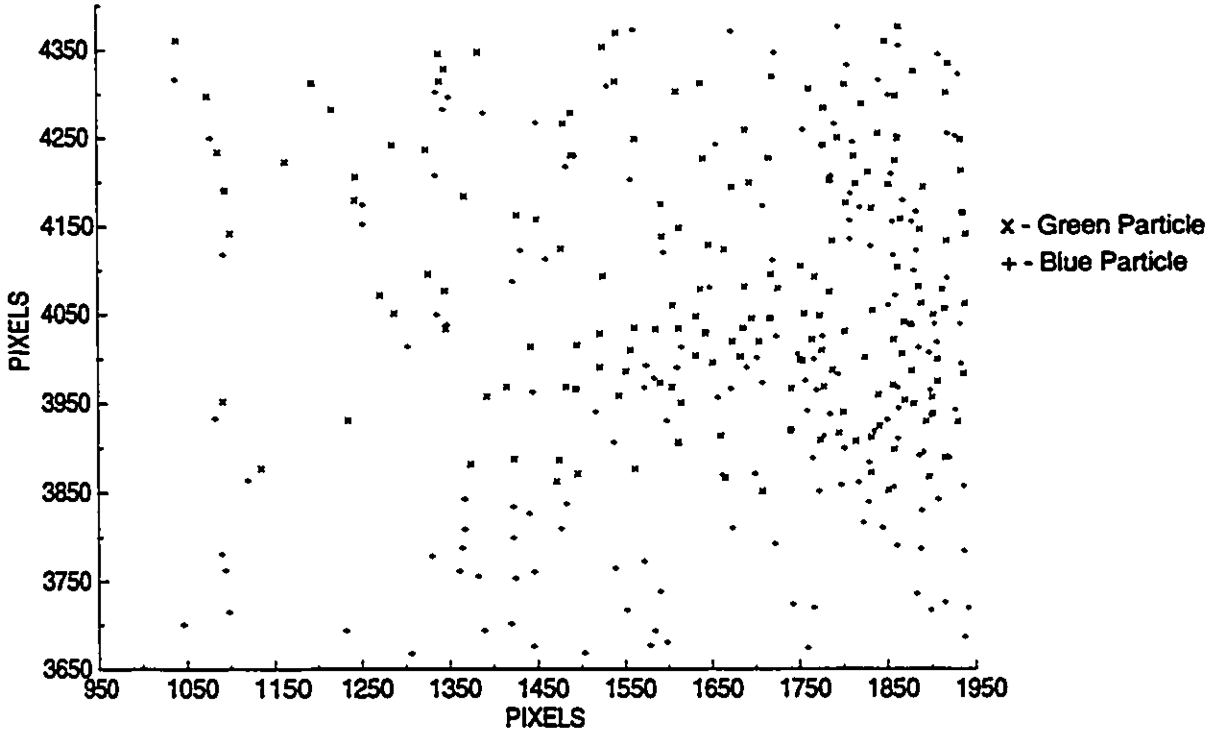

Figure 31. Blue and green particle locations determined from Figure 30 with the PIV analysis code.

images than blue was expected since some of the blue images are overexposed, causing response in the green layer of the film at the same location. Once the droplet locations are known, the analysis then calculates the most probable vector direction first for the subimage, and then, following further division, for each of its fourths and sixteenths. The most probable vector for each of the sixteenth regions was then applied to each blue image in the relevant region in an attempt to find a matching green particle. The result for subimage {2,6}, shown in Figure 32, is a vector representation of all the droplets that were successfully tracked.

The droplet tracking vectors from all 32 subimages were assembled and are shown in Figure 33, along with a schematic of the burner surface. A total of 985 droplets were tracked in the entire image, with velocities ranging from 0.3 m/s to 6.0 m/s. The maximum velocity was

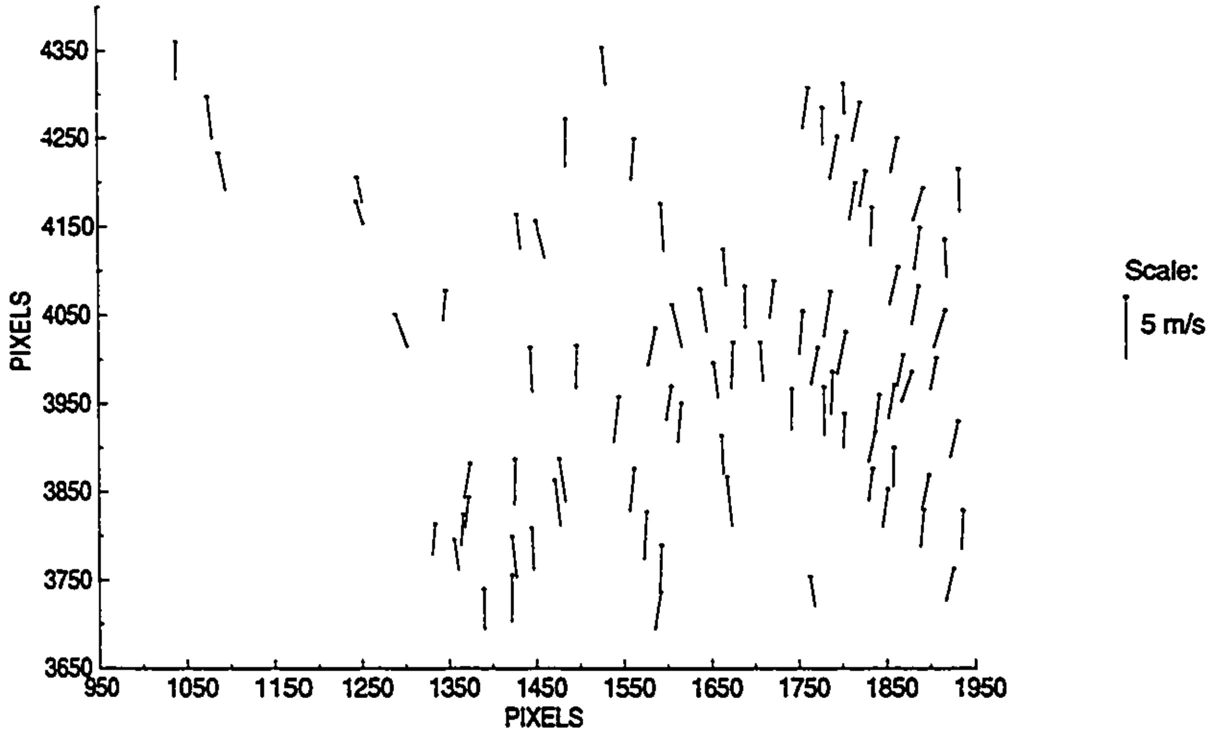

Figure 32. Velocities determined by PIV analysis code for the subsection shown in Figure 30. Each pixel of length in a vector represents a velocity of 0.0729 m/s.

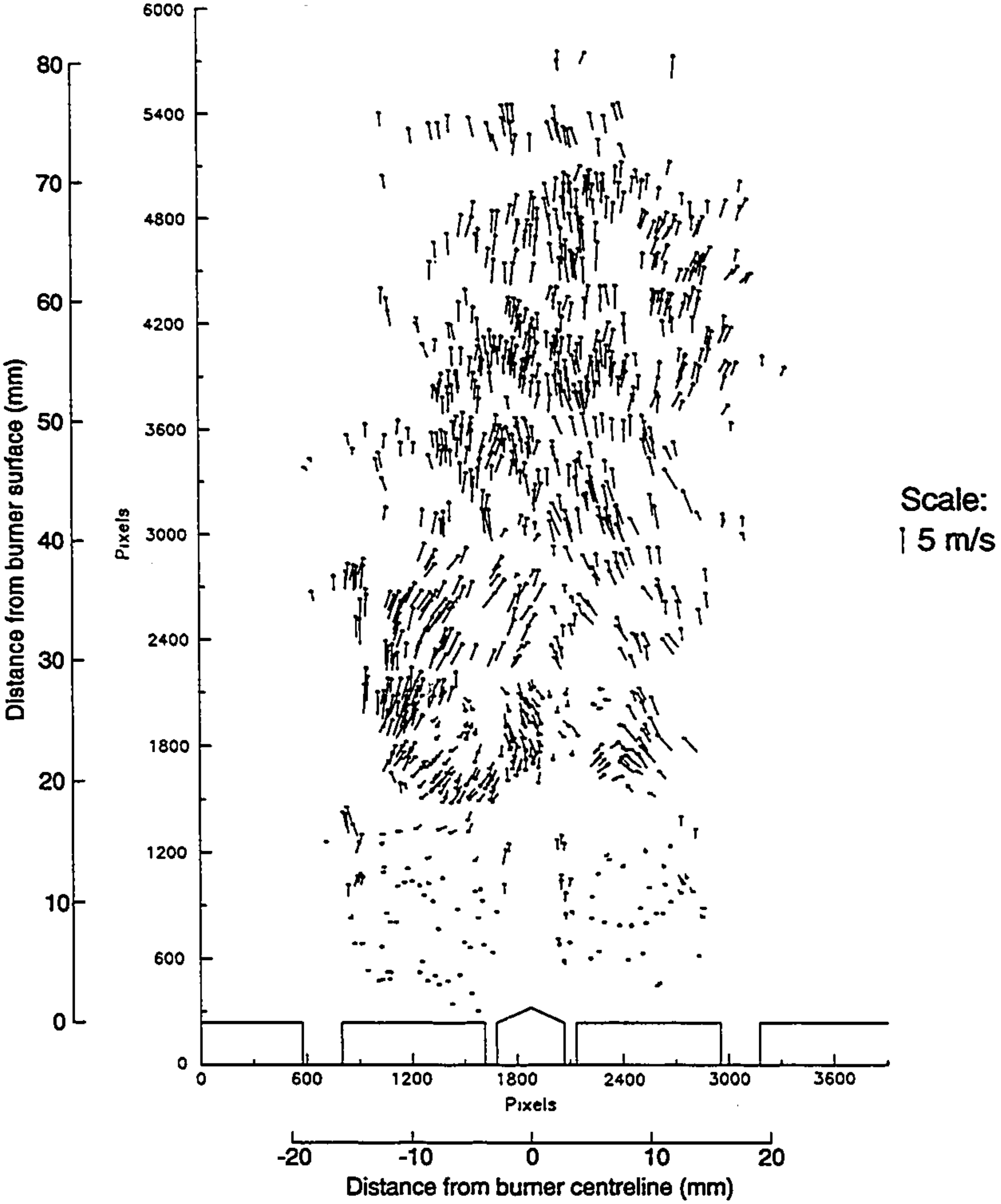

Figure 33. Velocities as determined for the full image (Figure 29). Each pixel of length in a vector represents a velocity of 0.0365 m/s.

greater than was expected. This may be due to a nonuniform velocity profile at the exit of the main air annulus. Inspection of Figure 33 reveals that no droplets were tracked in the region immediately above the nozzle, due to the high source density in this region. Also, one can visualize the boundaries of the subimages, since vectors cannot cross the boundaries past the 16 pixel overlap. A recommendation would be to increase the overlap to the maximum anticipated vector length so that these artificial boundaries do not interfere with the processing. The predicted centreline stagnation point is visible approximately 25 mm above the surface, with a second point appearing a further 10 mm up. There is a reverse flow zone on the centreline, as would be expected with a bluff-body design, although it has been lifted above the burner surface by the atomizing air flow. Many of the droplets appear in an intense recirculation zone that is also apparent at this elevated location. Closer to the burner surface a few droplets are entrained in a lazy, counter-rotating recirculation zone. Above approximately 35 mm from the burner all of the droplets are flowing upwards with no major structures evident.

Although the droplets are too large to fully respond to the air flow fluctuations, they are entrained sufficiently to represent the major structures in the flow. The randomly located data of Figure 33 have been interpolated to show a smoothed representation of the flowfield (Figure 34). This shows the same structures discussed above in a more coherent form. As outlined in Section 3.3, the interpolation algorithm uses inverse distance weighting in calculating the velocities, and does not extrapolate at all, since it is droplet, not flowfield, velocities that are being measured. If it were the flowfield velocity being measured, with small particles, then some extrapolation would be permitted to fill gaps in the data set.

To complement the instantaneous droplet velocity map that has been obtained, mean velocity measurements using LDA (laser Doppler anemometry) have been performed in the wake of this bluff-body burner under a number of noncombusting flow conditions. The conditions are

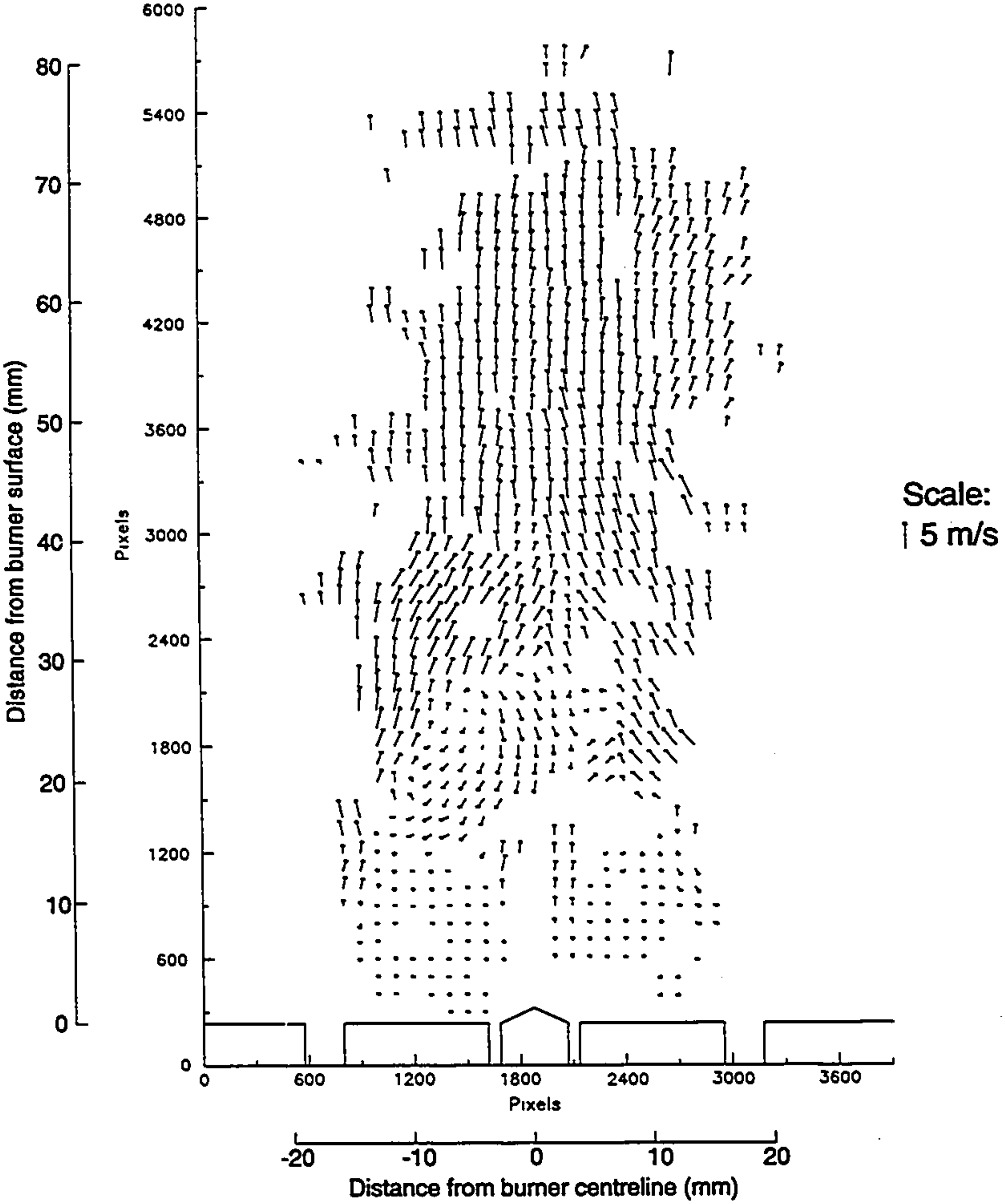

Figure 34. Velocity map interpolated from droplet velocities shown in Figure 33.

summarized in Table X, and the vector plots are shown in Figure 35 - Figure 38. Although the conditions are not identical to those used for the two-colour PIV experiments, the LDA results show the same large structures in the flow-field over a wide range of conditions encompassing those used for PIV photographs. The LDA data was acquired with 1 μm alumina particles as the seed, and represent the mean air velocity over a period of time at a point in space. As a contrast, the PIV data represents the instantaneous droplet velocities over a two-dimensional area at a point in time.

The LDA data were measured at locations from 5 mm to 80 mm above the burner surface, and from 6 mm on one side of the burner centreline to 16 mm on the other side. The results indicate that there may have been some asymmetry in the flowfield, probably due to the bluff-body not being centred perfectly with respect to the outer body of the burner. All conditions do show centreline flow reversal in the region above 15 mm and below 30 mm from the burner surface. This is closer to the burner than the PIV velocity map indicated. One explanation for this is that the momentum of the relatively larger droplets carries them beyond the air stagnation point to a higher location. Another possibility is that the location of this region of centreline flow reversal is fluctuating axially, and that the PIV photograph was taken at an instant when the axial position was further from the surface than the mean. The greatest mean air velocities measured by the LDA for flow conditions 1 and 2 are 3.7 m/s and 6.8 m/s, respectively. The instantaneous droplet velocities, obtained with PIV at conditions between these two, appear reasonable.

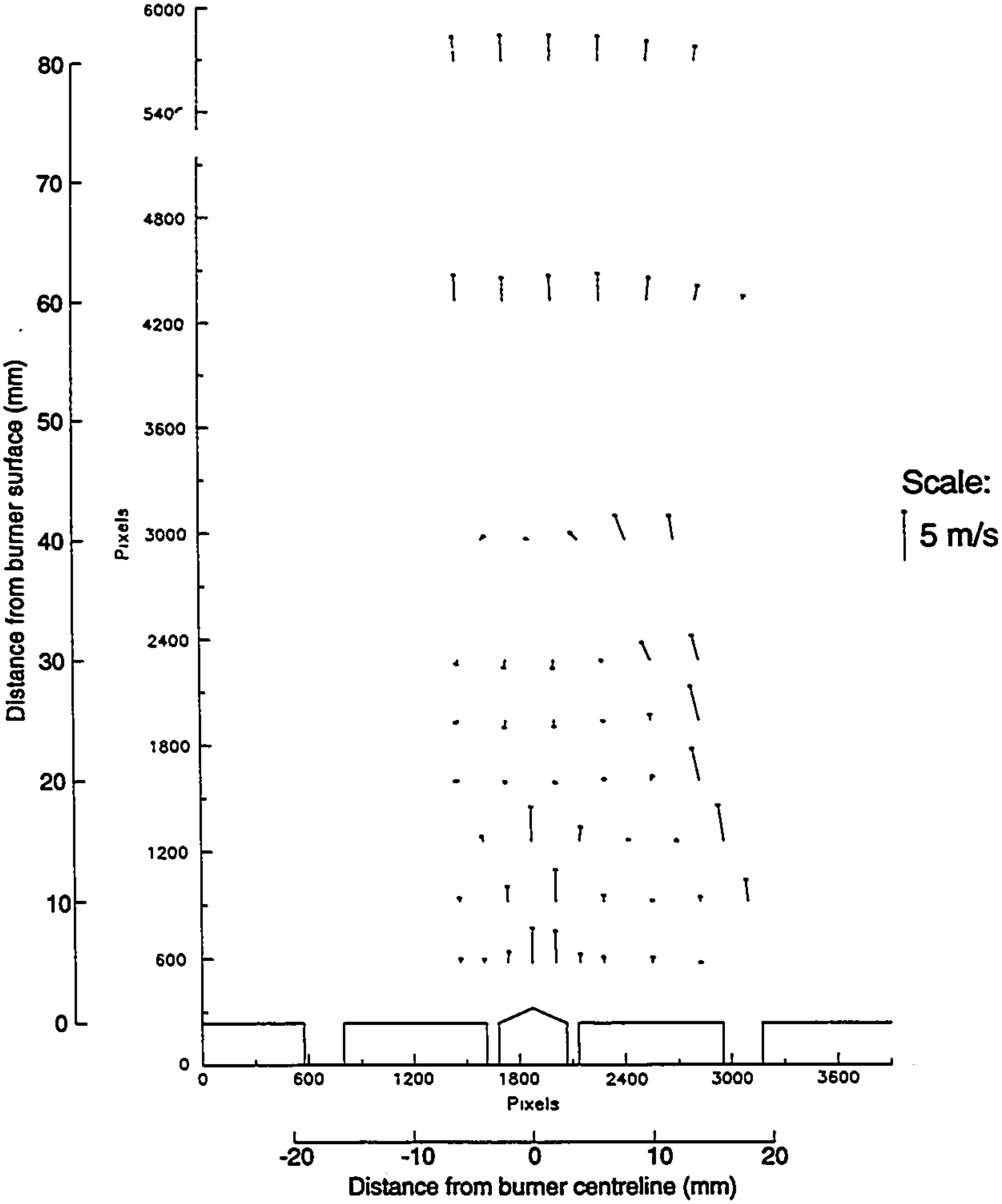

Figure 35. Particle velocities measured with LDA (flow condition 1).

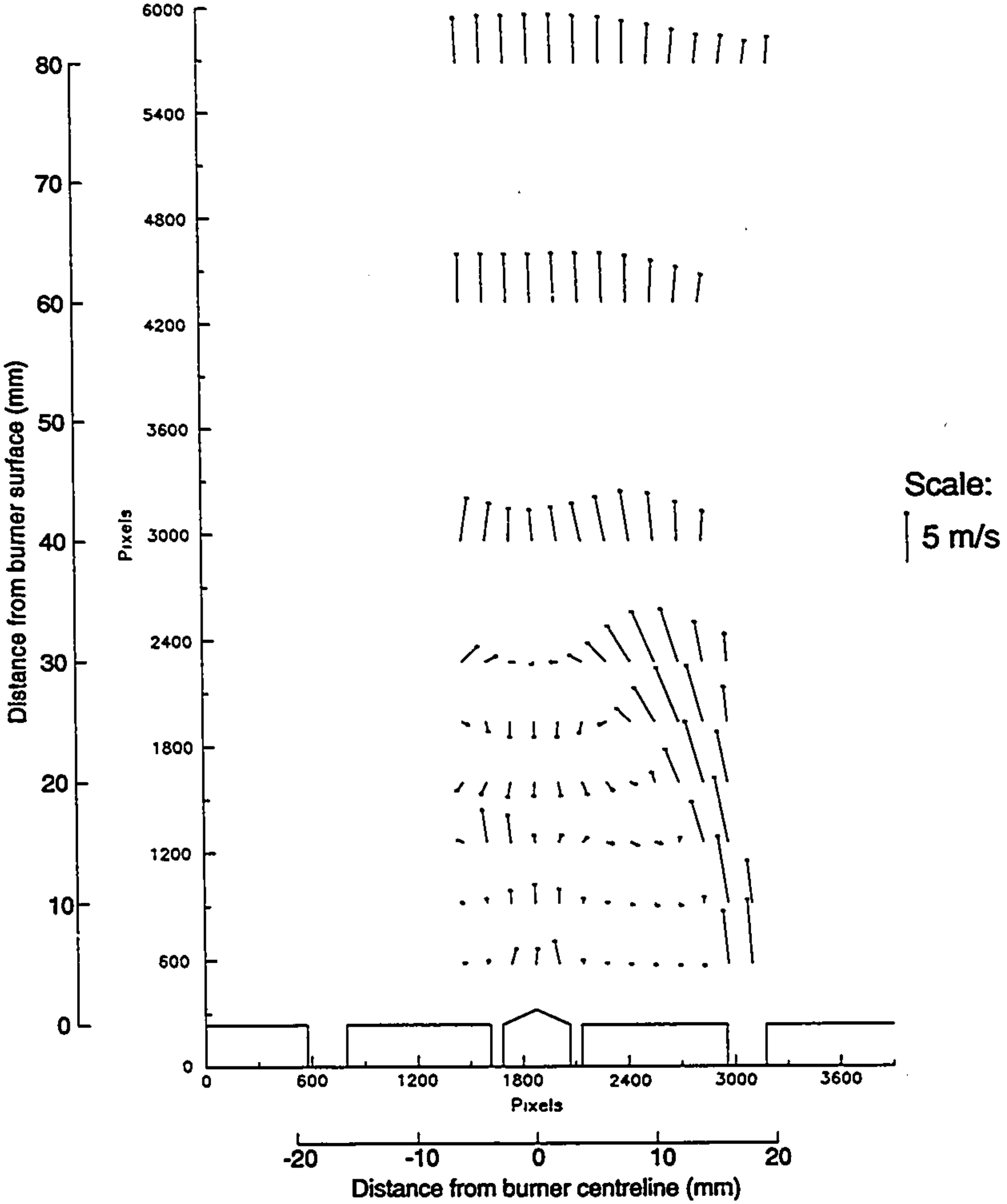

Figure 36. Particle velocities measured with LDA (flow condition 2).

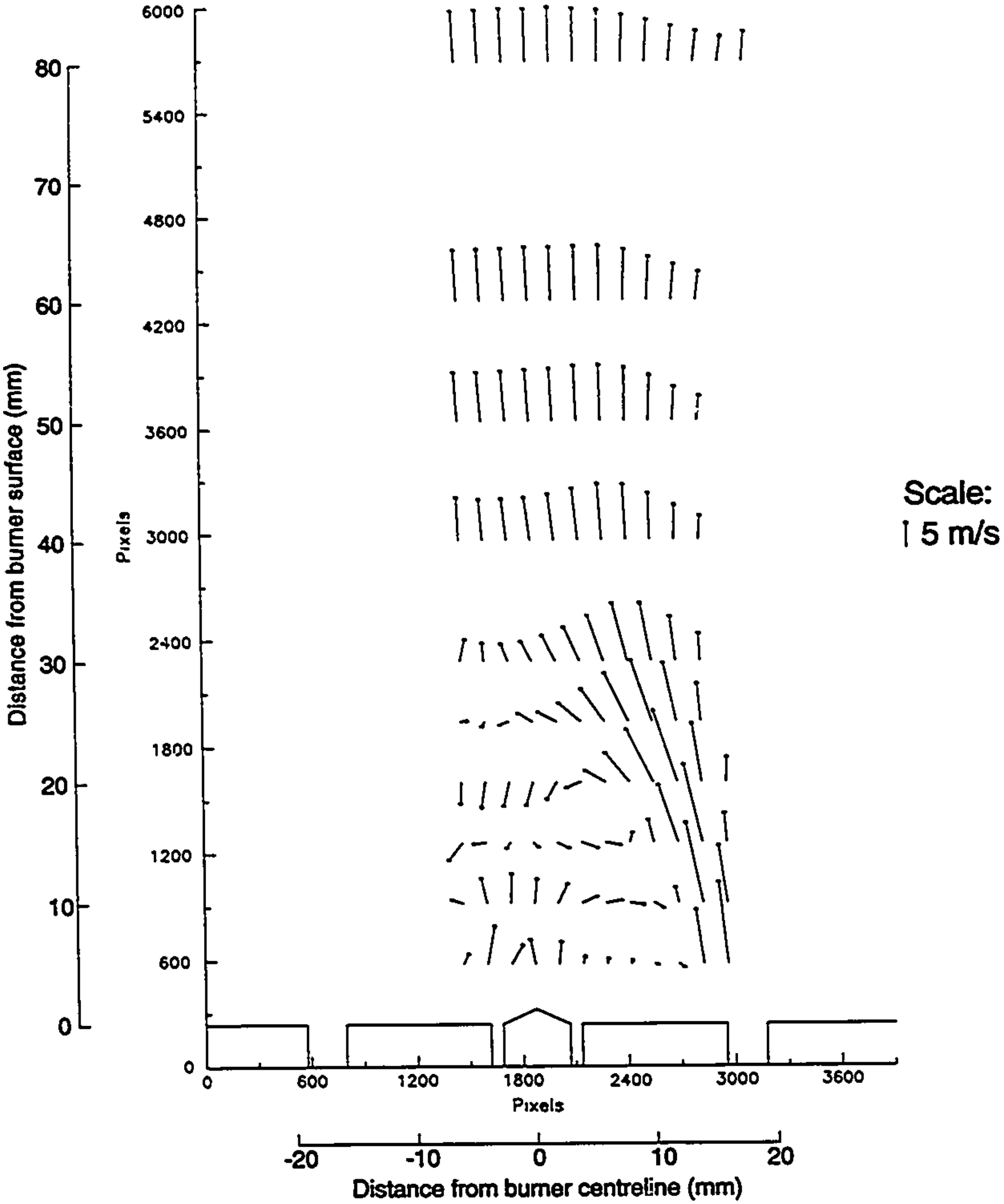

Figure 37. Particle velocities measured with LDA (flow condition 3).

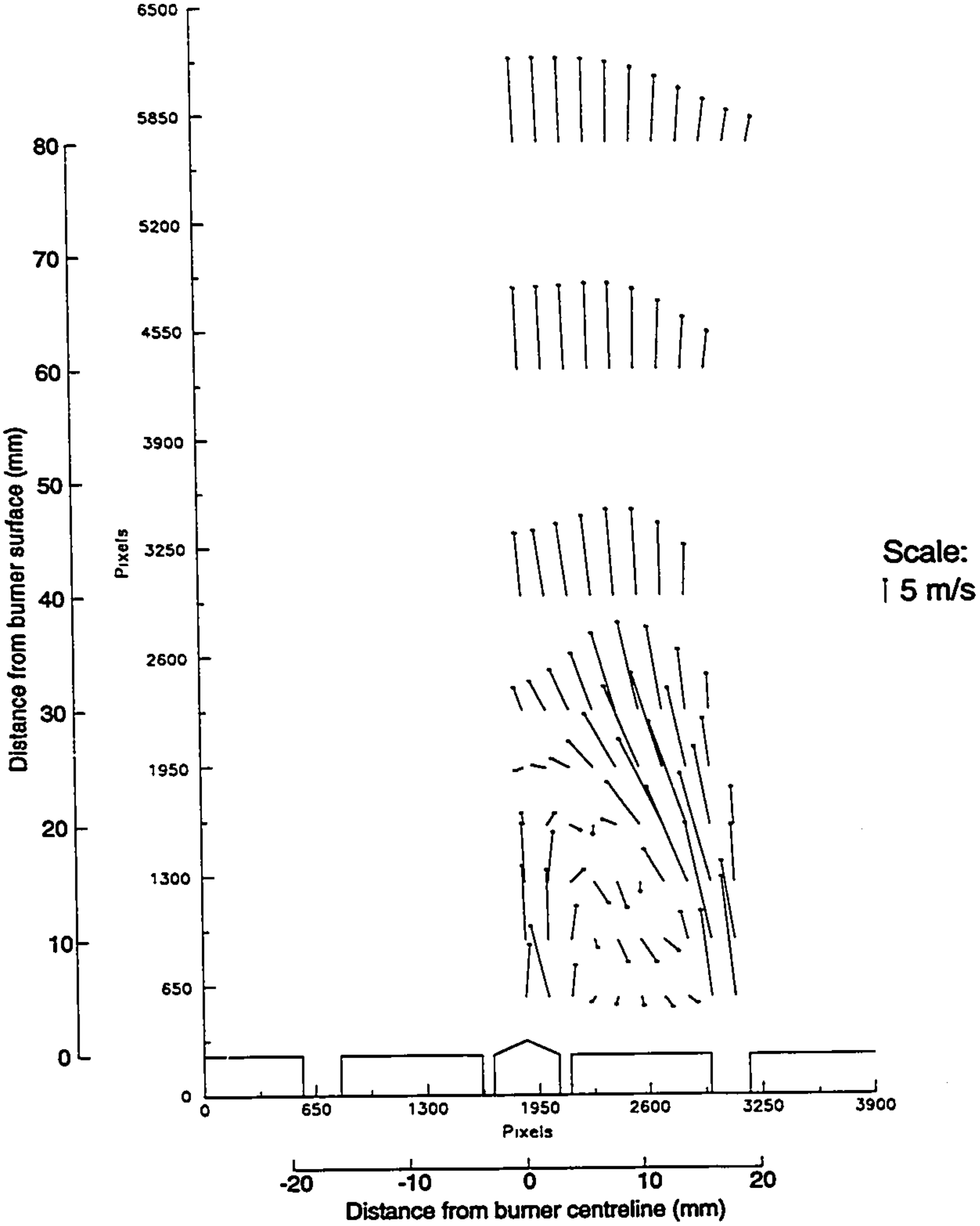

Figure 38. Particle velocities measured with LDA (flow condition 4).

6 CONCLUSIONS AND RECOMMENDATIONS

6.1 CONCLUSIONS

A technique for the acquisition of photographs for analysis by the two-colour particle image velocimetry method has been designed, developed, and evaluated. The primary advantages of the two-colour PIV method over conventional monochromatic double-pulse PIV are the lack of directional ambiguity and the reduced data analysis requirements. This technique is suitable for application to most of the wide range of complex flowfields encountered in combustion and related studies. These complex flowfields may include recirculation, flow reversal, combustion, soot radiation, liquid fuel sprays, scattering particle sizes from submicron seed particles to 100 μm droplets, and velocities from below 1 m/s to greater than 200 m/s.

The two-colour PIV technique was successfully applied in the wake of an unconfined axisymmetric liquid fuelled bluff-body stabilized diffusion flame burner. This was operated in a noncombusting condition which included two counter-rotating recirculation zones, two centreline stagnation points, centreline flow reversal, a liquid fuel spray with a wide droplet size distribution of 40 μm Sauter Mean Diameter, and droplet velocities from 0.4 m/s to 7.3 m/s. The dynamic range of measurable velocities is almost 20:1 in the configuration evaluated. These results indicate that this technique can be used to track particles in flowfields with large changes in velocity direction and magnitude.

These are the first reported measurements of spray velocities using PIV. No other single technique has been demonstrated with the flexibility to acquire images suitable for PIV analysis over the range of conditions that this method is applicable to. The dual flashlamp-pumped dye laser approach is more economical than the double-pulsed solid-state laser arrangements used in conventional monochromatic PIV, and is certainly less expensive than any of the other two-colour methods.

PIV has been shown to be a complementary technique to laser Doppler anemometry. LDA provides mean and turbulence intensity velocity data from local instantaneous velocities at a point in space over a period of time whereas PIV gives instantaneous velocities at a point in time over a planar region of space. PIV has been used to measure spatial features such as vorticity and strain rate,[4] and is more suited than LDA for velocity measurements in transient flow. The PIV results obtained are consistent with LDA measurements in the same burner.

Quantitative methods and related considerations for selecting the film and the seed particles have been presented. A method for determining the optimal exposure based on Mie scattering theory has been described. This accounts for the characteristics of the laser sheets, seed particle, fluid, lens and film.

The method used to analyze two-colour PIV images has been outlined. This separates the blue and green images, locates the particle positions in each, uses histogram analysis to determine the most probable velocity for a small region, and applies this velocity to match blue/green particle images in each region, resulting in actual particle velocities for successful matches. An inverse distance weighted interpolater has been used to represent the randomly spaced velocity vectors on an even grid for a different visual perception, smoothing the data in the process. This is useful for comparison with LDA data or with data produced by computer modelling.

6.2 RECOMMENDATIONS

Future experimentation should include combusting flows seeded with hollow alumina microspheres to verify the suitability of two-colour PIV under reacting conditions. To observe sprays under combusting conditions, a two-component fuel could be used to increase the droplet lifetime while maintaining flame stability. An example of this would be a mixture of hexadecane and heptane where the low volatility of the hexadecane would provide the increased lifetime and the higher volatility of the heptane would provide the flame stability.

Unless maximum resolution is absolutely required, high dynamic range should take precedence in selecting a film. Kodak Gold 100 is an example of a film with excellent dynamic range and good resolution.

The PIV analysis code requires rewriting to reduce execution time. The tracking portion of the code should be based only on particle coordinates, rather than an image containing particles as it now does. For seeded flows, analysis to provide vorticity and rate-of-strain data should also be performed.

When performing the particle tracking, the overlap between sections should be increased so that pairing of blue particles with green particles outside the section could occur. This would reduce the section boundary "banding" observed in the sample PIV analysis.

REFERENCES

1. L. Lourenco and A. Krothapalli, "Instantaneous Velocity Field Measurements of a Turbulent Rectangular Jet (AR-4) Using Particle Image Displacement Velocimetry," AIAA Paper 88-0498 (1988).

2. I. Grant, E. H. Owens, and G. H. Smith, "Particle image velocimetry fringe visibility as a means of turbulence estimation," Applied Optics **28**, 2982-2984 (1989).

3. M. E. Post, L. P. Goss, and L. F. Brainard, "Two-color particle-imaging velocimetry in a turbine cascade," AIAA Paper 91-0274 (1991).

4. D. L. Reuss, R. J. Adrian, C. C. Landreth, D. T. French, and T. D. Fansler, "Instantaneous planar measurements of velocity and large-scale vorticity and strain rate in an engine using particle-image velocimetry," SAE Paper 890616 (1989).

5. K. Wozniak, G. Wozniak, and T. Rösgen, "Particle-image-velocimetry applied to thermocapillary convection," Experiments in Fluids **10**, 12-16 (1990).

6. C. E. Camp, W. B. Kolb, K. L. Sublette, and R. L. Cerro, "The measurement of square channel velocity profiles using a microcomputer-based image analysis system," Experiments in Fluids **10**, 87-92 (1990).

7. R. Höcker and J. Kompenhans, "Application of particle image velocimetry to transonic flows," *Fifth International Symposium on Application of Laser Techniques to Fluid Mechanics, Lisbon, Portugal*, paper 15.1 (1990).

8. C. C. Landreth and R. J. Adrian, "Impingement of a low Reynolds number turbulent circular jet onto a flat plate at normal incidence," Experiments in Fluids **9**, 74-84 (1990).

9. D. L. Reuss, R. J. Adrian, and C. C. Landreth, "Two-dimensional velocity measurements in a laminar flame using particle image velocimetry," Combustion Science and Technology **67**, 73-83 (1989).

10. M. E. Post, L. P. Goss, and L. F. Brainard, "Two-color particle-imaging velocimetry in a diffusion flame," *1991 Spring Technical Meeting, Central States Section of the Combustion Institute, Nashville, TN* (1991).

11. P. R. Ereaut, "A laser light-sheet investigation of a laboratory coal flame," Journal of the Institute of Energy **62**, 14-20 (1989).

12. N. A. Chigier, "Optical imaging of sprays," Progress in Energy and Combustion Science **17**, 211-262 (1991).

13. G. J. Smallwood and D. R. Snelling, "A two-colour technique for two-dimensional particle image velocimetry," presented at *NATO Advanced Study Institute on Combusting Flow Diagnostics, Algarve, Portugal* (1990).

14. G. J. Smallwood and D. R. Snelling, "A two-colour technique for velocity mapping in spray combustion," *1991 Spring Technical Meeting, Canadian Section of the Combustion Institute, Ottawa, ON* (1991).

15. A. C. Eckbreth, *Laser Diagnostics for Combustion Temperature and Species* (Abacus, Cambridge, MA, 1988).

16. R. J. Adrian, "Particle-imaging techniques for experimental fluid mechanics," Annual Review of Fluid Mechanics **23**, 261-304 (1991).

17. A. Cenedese and A. Paglialunga, "Digital direct analysis of a multiexposed photograph in PIV," Experiments in Fluids **8**, 273-280 (1990).

18. J. C. Hunter and M. W. Collins, "The processing of data from optical whole-field measurement methods and large eddy simulation predictions to investigate coherent structures in fluid flow," International Journal of Optoelectronics **5**, 405-438 (1990).

19. L. M. Lourenco, A. Krothapalli, and C. A. Smith, "Particle image velocimetry," in *Advances in Fluid Mechanics Measurements*, M. Gad-el-Hak, Ed. (Springer-Verlag, Berlin, 1989), pp. 127-199.

20. L. Hesselink, "Digital image processing in flow visualization," Annual Review of Fluid Mechanics **20**, 421-485 (1988).

21. T. D. Dudderar and P. G. Simpkins, "Laser speckle photography in a fluid medium," Nature **270**, 45-47 (1977).

22. D. B. Barker and M. E. Fourney, "Measuring fluid velocities with speckle patterns," Optics Letters **1**, 135-137 (1977).

23. R. Meynart, "Flow velocity measurement by a speckle method," *Second European Congress on Optics Applied to Metrology*, SPIE **210**, 25-28 (1977).

24. R. Meynart, "Speckle velocimetry study of vortex pairing in a low-Re unexcited jet," Physics of Fluids **26**, 2074-2079 (1983).

25. C. J. D. Pickering and N. A. Halliwell, "Laser speckle photography and particle image velocimetry: photographic film noise," Applied Optics **23**, 2961-2969 (1984).

26. R. J. Adrian, "Scattering particle characteristics and their effect on pulsed laser measurements of fluid flow: speckle velocimetry vs particle image velocimetry," Applied Optics **23**, 1690-1691 (1984).

27. R. J. Adrian and C. S. Yao, "Development of pulsed laser velocimetry (PLV) for measurement of turbulent flow," *Proceedings of the Eighth Symposium on Turbulence*, X. B. Reed, G. K. Patterson, and J. L. Zakin, Eds. (University of Missouri, Rolla, 1984), pp. 170-186.

28. C. C. Landreth, R. J. Adrian, and C. S. Yao, "Double pulsed particle image velocimeter with directional resolution for complex flows," Experiments in Fluids **6**, 119-128 (1988).

29. L. Lourenco, "Application of laser speckle and particle image velocimetry in flows with velocity reversal," Bulletin of the American Physical Society **31**, 1723 (1986).

30. C. C. Landreth and R. J. Adrian, "Electrooptical image shifting for particle image velocimetry," Applied Optics **27**, 4216-4220 (1988).

31. I. Grant and A. Liu, "Directional ambiguity resolution in particle image velocimetry by pulse tagging," Experiments in Fluids **10**, 71-76 (1990).

32. G. J. Smallwood, W. S. Neill, and D. R. Snelling, "Diesel engine combustion program at the Defence Research Establishment Ottawa," DREO Report No. 926 (1985).

33. L. P. Goss, M. E. Post, D. D. Trump, B. Sarka, C. D. MacArthur, and G. E. Dunning, "A novel technique for blade-to-blade velocity measurements in a turbine cascade," AIAA Paper 89-2691 (1989).

34. L. P. Goss, M. E. Post, D. D. Trump, and B. Sarka, "Two-color particle velocimetry," *Proceedings, ICALEO '89, Orlando, FL*, Laser Institute of America **68**, 101-111 (1988).

35. D. A. Nye and D. A. Santavicca, "Two color particle image velocimetry," *1991 Fall Technical Meeting, Eastern Section of the Combustion Institute, Ithaca, NY* (1991).

36. A. A. Adamczyk and L. Rimai, "2-dimensional particle tracking velocimetry (PTV): technique and image processing algorithms," Experiments in Fluids **6**, 373-380 (1988).

37. B. Khalighi, "Quantitative fluid velocity measurements by automatic analysis of flow visualization images," Experiments in Fluids **7**, 142-144 (1989).

38. B. Khalighi and Y. H. Lee, "Particle tracking velocimetry: an automatic image processing algorithm," Applied Optics **28**, 4328-4332 (1989).

39. M. P. Wernet and R. V. Edwards, "New space domain processing technique for pulsed laser velocimetry," Applied Optics **29**, 3399-3417 (1990).

40. M. P. Wernet "Two-dimensional particle displacement tracking in particle imaging velocimetry," Applied Optics **30**, 1839-1846 (1991).

41. B. R. Frieden and C. K. Zoltani, "Fast tracking algorithm for multiframe particle image velocimetry data," Applied Optics **28**, 652-655 (1989).

42. Y. A. Hassan, T. K. Blanchat, and R. D. Hild, "Full-field velocity imaging technique using high-energy pulsed laser velocimetry," *Image Processing Algorithms and Techniques*, SPIE **1244**, 130-142 (1990).

43. R. E. Canaan and Y. A. Hassan, "Full-field bubbly flow velocity measurements near a heated cylindrical conductor using digital pulsed laser velocimetry," *Proceedings of the Twelfth Symposium on Turbulence*, (University of Missouri, Rolla, 1990), pp. B17.1-B17.9.

44. Y. A. Hassan and T. K. Blanchat, "Full-field bubbly flow velocity measurements by digital image pulsed laser velocimetry," Experiments in Fluids **11**, 293-301 (1991).

45. Y.-C. Cho, "Digital image velocimetry," Applied Optics **28**, 740-748 (1989).

46. Y.-C. Cho and H. Park, "Instantaneous velocity field measurement of objects in coaxial rotation using digital image velocimetry," *Ultrahigh- and High-Speed Photography, Videography, Photonics, and Velocimetry '90*, SPIE **1346**, 160-171 (1990).

47. C. E. Willert and M. Gharib, "Digital particle image velocimetry," *Fluid Measurement and Instrumentation Forum - 1990, Toronto, ON*, ASME FED **95**, 39-44 (1990).

48. A. Cenedese and A. Paglialunga, "A new technique for the determination of the third velocity component with PIV," Experiments in Fluids **8**, 228-230 (1989).

49. G. R. Denger and M. W. McBride, "Three-dimensional flow field characteristics measured in a forward-curved centrifugal blower using particle tracing velocimetry (PTV)," *Fluid Measurement and Instrumentation Forum - 1990, Toronto, ON*, ASME FED **95**, 49-56 (1990).

50. A. A. Adamczyk and L. Rimai, "Reconstruction of a 3-dimensional flow field from orthogonal views of seed track video images," Experiments in Fluids **6**, 380-386 (1988).

51. R. G. Racca and J. M. Dewey, "A method for automatic particle tracking in a three-dimensional flow field," Experiments in Fluids **6**, 25-32 (1988).

52. H.-G. Maas, "Digital photogrammetry for determination of tracer particle coordinates in turbulent flow research," *Close-Range Photogrammetry Meets Machine Vision*, SPIE **1395**, 391-398 (1990).

53. I. Grant and J. H. Qiu, "Digital convolution filtering techniques on an array processor for particle image velocimetry," Applied Optics **29**, 4327-4329 (1990).

54. J. M. Coupland and N. A. Halliwell, "Particle image velocimetry: rapid transparency analysis using optical correlation," Applied Optics **27**, 1919-1921 (1988).

55. A. Kirita, C. J. D. Pickering, and N. A. Halliwell, "Particle image velocimetry: a new approach to fringe analysis," Optics in Lasers and Engineering **7**, 137-147 (1987).

56. C.-S. Yao and R. J. Adrian, "Orthogonal compression and 1-D analysis technique for measurement of 2-D particle displacements in pulsed laser velocimetry," Applied Optics **23**, 1687-1689 (1984).

57. C. J. D. Pickering and N. A. Halliwell, "Particle image velocimetry: improving fringe signal-to-noise ratio with a two-step photographic process," Journal of the Optical Society of America A **2**, 610-615 (1985).

58. C. J. D. Pickering and N. A. Halliwell, "Particle image velocimetry: improving fringe signal-to-noise ratio with a two-step photographic process. Part II," Journal of the Optical Society of America A **2**, 1721-1724 (1985).

59. I. Grant and A. Liu, "Accuracy considerations in incoherent analysis of PIV images," Applied Optics **28**, 4508-4510 (1989).

60. A. K. Prasad, R. J. Adrian, C. C. Landreth, and P. W. Offutt, "Effect of resolution on the speed and accuracy of particle image velocimetry interrogations," *Proceedings of the Twelfth Symposium on Turbulence* (University of Missouri, Rolla, 1990), pp. B14.1-B14.10.

61. R. D. Keane and R. J. Adrian, "Optimization of particle image velocimeters. Part I: double pulsed systems," Measurement Science and Technology **1**, 1202-1215 (1990).

62. S. K. Sinha, "Improving the accuracy and resolution of particle image or laser speckle velocimetry," Experiments in Fluids **6**, 67-68 (1988).

63. Y. G. Guezennec and N. Kiritsis, "Statistical investigation of errors in particle image velocimetry," Experiments in Fluids **10**, 138-146 (1990).

64. W. V. Feller and J. F. Meyers, "Development of a controllable particle generator for LDV seeding in hypersonic wind tunnels," *Proceedings, 1975 Minnesota Symposium on Laser Anemometry*, E. R. G. Eckert, Ed. (University of Minnesota, Minneapolis, 1976), pp. 342-357.

65. W. D. Bachalo, Aerometrics Inc., Sunnyvale, CA (personal communication, 1992).

66. R. J. Adrian and W. L. Earley, "Evaluation of LDV performance using Mie scattering theory," *Proceedings, 1975 Minnesota Symposium on Laser Anemometry*, E. R. G. Eckert, Ed. (University of Minnesota, Minneapolis, 1976), pp. 426-454.

67. R. J. Adrian and C.-S. Yao, "Pulsed laser technique application to liquid and gaseous flows and the scattering power of seed materials," Applied Optics **24**, 44-52 (1985).

68. D. L. Hofeldt and R. K. Hanson, "Instantaneous imaging of particle size and spatial distribution in two-phase flows," Applied Optics **30**, 4936-4948 (1991).

69. M. Kerker, *The Scattering of Light and Other Electromagnetic Radiation* (Academic, New York, 1969).

70. H. C. van de Hulst, *Light Scattering by Small Particles* (Dover, New York, 1957).

71. S. V. Sankar and W. D. Bachalo, "Response characteristics of the phase Doppler particle analyzer for sizing spherical particles larger than the light wavelength," Applied Optics **30**, 1487-1496 (1991).

72. C. F. Bohren and D. R. Huffman, *Absorption and Scattering of Light by Small Particles* (Wiley, New York, 1983).

73. *Kodak Publication E-122*

74. *Kodak Publication Z-22-ED*

75. *Kodak Publication E-2*

76. M. Mitchell, "The design and characterization of a two laser flow/spray visualization system for diesel engines," Defence Research Establishment Ottawa (DREO) Memorandum No. 46/84 (1984)

77. *Nikon Lens Manual 8& 139-B02*

APPENDIX A: INTEGRATION OF SCATTERED IRRADIANCE COLLECTED BY THE LENS

The differential scattering cross-section varies with both the scattering angle θ_s and the azimuthal angle ϕ (see Figure 39). The integral

$$\int_{\Omega} i \, d\Omega \tag{28}$$

must be evaluated with reference to θ_s and ϕ, since $i = f(\theta_s, \phi)$ and i is not a direct function of Ω. The nomenclature for Figure 39 has the particle at the origin, the x-axis on the lens axis, and the y-z plane coincident with the laser sheet, with β the angle between the x-axis and a scattered ray

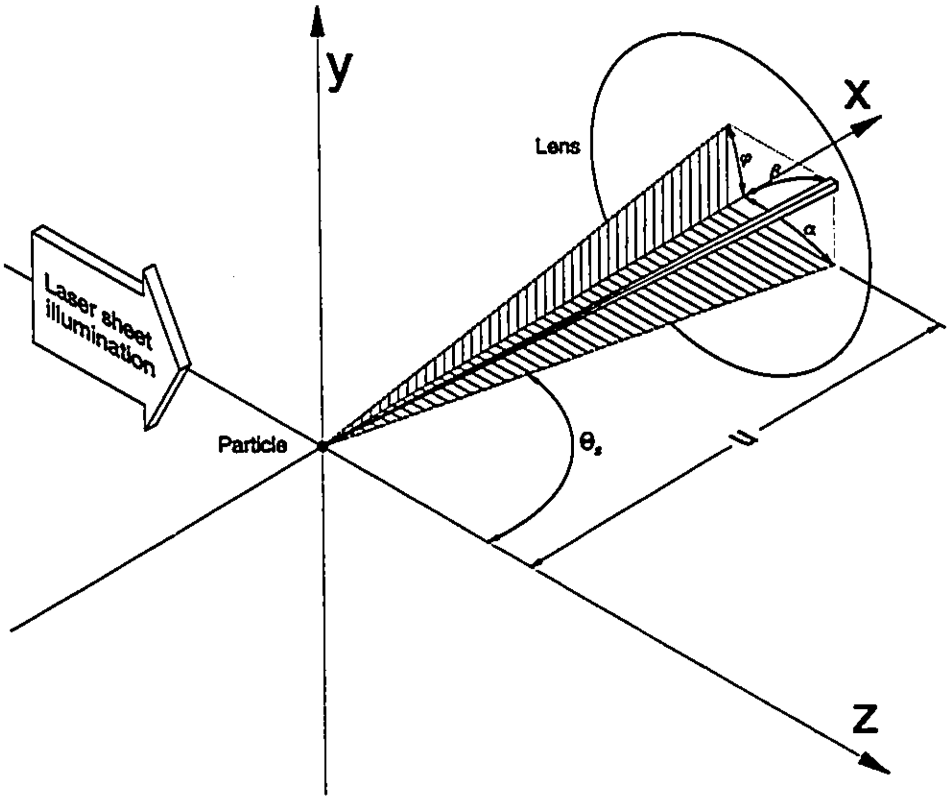

Figure 39. Orientation of arbitrary scattered ray striking lens.

striking an arbitrary detection point on the lens, θ_s the scattering angle in the x-z plane, z the direction of propagation of the light sheet, $\alpha = \pi/2 - \theta_s$ the angle from the lens axis to the detection point projected on the x-z plane, ϕ the azimuthal angle from the lens axis to the detection point projected on the x-y plane, and u the object distance from the lens. Figure 40 shows the lens projected on the y-z plane, with R being the radius of the lens and r the radius to an arbitrary detection point.

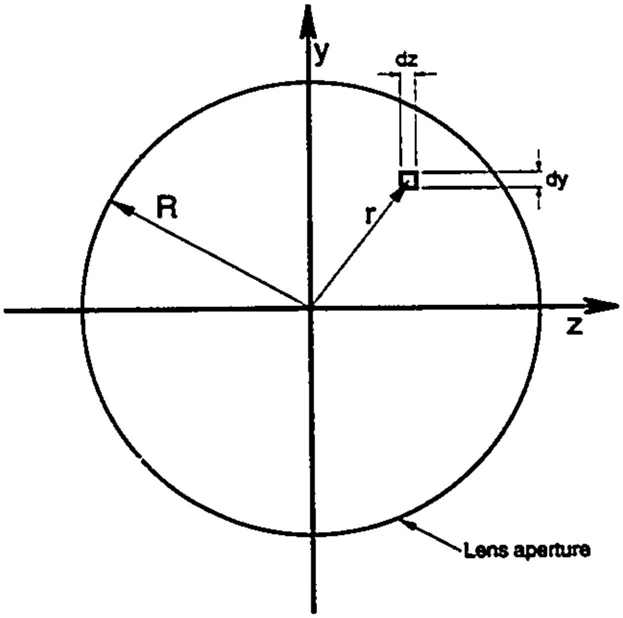

Figure 40. Arbitrary detection point located on lens.

The solid angle subtended by a lens is defined as

$$\Omega = \frac{A}{s^2} \tag{29}$$

where A is the surface area of a spherical section defined by the lens, and $s = u/\cos\beta$ is the distance from the origin to the lens. Differentiating results in

$$d\Omega = \frac{dA}{(u/\cos\beta)^2} \; . \tag{30}$$

From Figure 40, $dA = dydz$, and from Figure 39 and Figure 40,

$$\begin{aligned}\beta &= \tan^{-1}\left(\frac{r}{u}\right)\\ &= \tan^{-1}\left(\frac{\sqrt{y^2+z^2}}{u}\right).\end{aligned} \tag{31}$$

For small angles, $\alpha \approx z/u$ and $\phi \approx y/u$, resulting in $dz \approx ud\alpha$, $dy \approx ud\phi$, and

$$\begin{aligned}\beta &= \tan^{-1}\left(\frac{\sqrt{\alpha^2u^2+\phi^2u^2}}{u}\right)\\ &= \tan^{-1}\left(\sqrt{\alpha^2+\phi^2}\right)\\ &\approx \sqrt{\alpha^2+\phi^2}\end{aligned} \tag{32}$$

With substitutions, Equation (30) becomes

$$\begin{aligned}d\Omega &= \frac{u\,d\phi\;u\,d\alpha\;\cos^2\left(\sqrt{\alpha^2+\phi^2}\right)}{u^2}\\ &= \cos^2\left(\sqrt{\alpha^2+\phi^2}\right)\,d\alpha\;d\phi\end{aligned} \tag{33}$$

Simple lens theory (Equations (34)-(36)) can be used to develop an alternative representation for u (the object distance) in terms of f-number ($f\#$), magnification (M), and aperture diameter (d_a). The focal length of the lens is represented by f, and the image distance is v.

$$f\# = \frac{f}{d_a} \tag{34}$$

$$M = \frac{v}{u} \tag{35}$$

$$\frac{1}{f} = \frac{1}{u} + \frac{1}{v} \tag{36}$$

Substituting Equation (35) into Equation (36) yields

$$\frac{1}{f} = \frac{M+1}{M\,u} \tag{37}$$

and substitution of Equation (34) into Equation (37) results in

$$f\# = \frac{M\,u}{2R\,(M+1)} \tag{38}$$

where d_a has been replaced by $2R$. The integration limits are $z = \pm R$ and $y = \pm R$. Combining (38) with the above relations for α and ϕ results in these limits becoming $\alpha = \pm M/2f\#(M+1)$ and $\phi = \pm M/2f\#(M+1)$. The integral can then be represented by

$$\int_{\Omega} i\; d\Omega = \int_{-\frac{M}{2f\#(M+1)}}^{\frac{M}{2f\#(M+1)}} \int_{-\frac{M}{2f\#(M+1)}}^{\frac{M}{2f\#(M+1)}} i(\alpha,\phi)\;\cos^2\left(\sqrt{\alpha^2+\phi^2}\right)\,d\alpha\;d\phi \tag{39}$$

which can be evaluated numerically. This is done by dividing the projection of the lens onto the y-z plane into a calculation grid, calculating i as shown in Equation 7 for each point in the grid, and then summing the integrand for all points in the grid. The test

$$\sqrt{\alpha^2+\phi^2} \le \frac{M}{2f\#\,(M+1)} \tag{40}$$

must be applied at each point in the calculation grid to ensure that the point lies within the lens aperture.

APPENDIX B: DETERMINATION OF LENS BLUR DIAMETER

The algorithm for the diameter of the point response function of a diffraction limited lens, d_s, measured at the first dark ring of the Airy disk intensity distribution, is developed from the definition of the Airy disc

$$\sin\theta_a = \frac{1.22\,\lambda}{d_a} \tag{41}$$

where θ_a is the half-angle of the diffraction-limited spot size and d_a is the diameter of the aperture of the lens. For small angles

$$\sin\theta_a \approx \theta_a \tag{42}$$

$$\theta_a = \frac{1.22\,\lambda}{d_a}\ . \tag{43}$$

The diameter of the spot size, d_s, is determined by

$$d_s = 2\,\theta_a\,v \tag{44}$$

where v is the distance from the lens to the image plane. Simple lens theory (Equations (34)-(36)) can be used to develop an alternative representation for v in terms of *f*-number (*f#*), magnification (*M*), and aperture diameter (d_a). Substituting Equation (35) into Equation (36) yields

$$\frac{1}{f} = \frac{M+1}{v} \tag{45}$$

and substitution of Equation (34) into Equation (45) results in

$$\frac{1}{d_a\, f\#} = \frac{M+1}{v} \tag{46}$$

which can be rearranged to

$$v = (M+1)\, f\#\, d_a \quad . \tag{47}$$

Finally, substitution of Equation (47) and Equation (43) into Equation (44) produces

$$\begin{aligned} d_s &= 2\left(\frac{1.22\,\lambda}{d_a}\right)[(M+1)\, f\#\, d_a] \\ &= 2.44\ (M+1)\, f\#\,\lambda \quad . \end{aligned} \tag{48}$$